“The Composition Dependence of the Photochemical Reactivity of Barium Strontium Titanates.”

Thesis

Abhilasha Bhardwaj

Advisor – Dr. G.S. Rohrer

Materials Science and Engineering

Carnegie Mellon University

Abstract

The efficiency of particulate water photolysis catalysts is impractically low due to the recombination of intermediate species and charge carriers. The back reaction can occur easily if the oxidation and reduction sites on the surface of the catalyst are not far enough apart. It is hypothesized that it will be possible to increase the separation of the sites of the two half reactions and reduce the recombination of photogenerated charge carriers by using a ferroelectric material with permanent internal dipolar fields. This separation of the reaction sites may significantly increase the efficiency of the process. The present work compares the photochemical reactivities of ferroelectric and nonferroelectric materials ($Sr_xBa_{1-x}TiO_3$, $0.0 \leq x \leq 1.0$) with similar composition and structure. The reactivities are compared by measuring the color change of methylene blue dye after the aqueous dye solution reacts on the surface of ceramic sample pellets as a result of exposure to UV light. The reactivities are also compared by measuring the amount of silver that is formed when an aqueous $AgNO_3$ solution photochemically reacts on the surface. The change in the color of the dye is measured by diffuse reflectance spectroscopy and absorbance measurements. The amount of silver is measured by atomic force microscopy. The photochemical reactivity of $Sr_xBa_{1-x}TiO_3$ shows a local maximum at the composition of the ferroelectric to non-ferroelectric transition. Also, the reactivities decrease as $BaTiO_3$ and $SrTiO_3$ become less pure. The dominant factors causing this trend in reactivities of $Sr_xBa_{1-x}TiO_3$ are the dielectric constant and alloy scattering. It is found that higher values of the dielectric constant increase the photochemical reactivity by enlarging the space charge region. The increase in alloy scattering in $Sr_xBa_{1-x}TiO_3$

solid solutions as x increases from zero or decreases from 1, has adverse effect on reactivity. There are other factors such as ferroelectric polarization, relative band edge positions and pH of the solution that can influence the reactivity. However, these factors are not significant in determining the composition dependence of the photochemical reactivity of $Sr_xBa_{1-x}TiO_3$. The comparison of the surfaces of $Sr_xBa_{1-x}TiO_3$ samples imaged by AFM after reaction (with silver nitrate) also showed that the mode of reaction gradually changes from spatially selective reactivity for $BaTiO_3$ to spatially uniform reactivity for $SrTiO_3$. The spatially selective reactivity disappears completely when x in $Sr_xBa_{1-x}TiO_3$ is greater than or equal to 0.28. The mechanism of the photochemical reaction of methylene blue dye on $Sr_xBa_{1-x}TiO_3$ was also studied. It is found that the dye reacts by a mechanism similar to that of silver. The methylene blue dye and silver reduce on the surfaces of positively charged domains and the reduced reaction products remain at the reduction reaction site.

Extensions of this research would be to experimentally determine the band edges and defect concentrations in $Sr_xBa_{1-x}TiO_3$ to get a better understanding of their influence on photochemical reactivity. Since the long term goal of this research is to find a efficient particulate catalyst for photocatalysis of water, the next step in this research is to carry out the photocatalysis of water using $Sr_xBa_{1-x}TiO_3$ powders. The effect of catalyst particle size should also be analyzed.

Acknowledgements

I would first like to thank my advisor, Dr. Greg Rohrer, for his guidance and encouragement, and extreme patience to go through several revisions of my documents over the years. I would also like to thank my committee members, Dr. Paul Salvador, Dr. Jay Whittacre and Dr. Annette Jacobson, whose invaluable suggestions helped a great deal in shaping this thesis. The financial support of the NSF is also gratefully acknowledged, as well as the support of the staff and faculty in the MSE department. I would specially like to thank Anita Connelly for always explaining any doubts that I had regarding paperwork and also for being a friend and well–wisher of my husband and myself.

I would also like to thank my friends and colleagues for their help and support over the years. I would specially like to thank Nina Burbure for the endless discussions on electrochemistry to understand our research better and also for lending me help and a patient ear whenever I faced an obstacle. Additionally, I would like to thank Amit Prakash and Abhishek Singh for their support and for being there whenever I needed a friend to talk to.

I am grateful to my family for their incessant love and encouragement throughout my entire life. My parents and in-laws have been my support system and my mentors in more ways than one. I would specially like to thank my mother, brother and brother-in-law who have always helped me in seeing the lighter side of things.

Lastly, I would like to thank my husband, Pranay Choudhary, for being my best friend and critic. His perseverance and dedication towards work has been my source of inspiration to move forward despite odds. I would like to acknowledge his help with the

scanning electron microscopy that I used to analyze the surfaces of my samples, and also with the formatting of my thesis. I could not have attained my career goals without his love and support.

I dedicate this thesis to my husband, Pranay, who encouraged me to join graduate school and motivated me to achieve my objectives ever since.

TABLE OF CONTENTS

TABLE OF CONTENTS

TABLE OF CONTENTS

LIST OF FIGURES

LIST OF FIGURES

LIST OF FIGURES

LIST OF FIGURES

LIST OF TABLES

1. Introduction

1.1 Motivation.

Depleting fossil fuel reserves and environmental pollution concerns have opened new horizons for the development and usage of alternate fuels. Power generation from hydrogen is a superior option as it stores approximately 2.6 times the energy per unit mass as gasoline and there are no green house gases or radioactive byproducts. Apart from being an energy source, hydrogen is also an ingredient for the synthesis of several materials such as ammonia, methanol, heating oil and rocket fuel. It is also used to make fertilizers, glass, refined metals, vitamins, cosmetics, semiconductor circuits, soaps, lubricants, cleaners, and even margarine and peanut butter [1]. However, all the current applications and promising possibilities for the usage of hydrogen are limited by its high cost of production.

In 1972, Fujishima and Honda [2] brought forth a new method for the generation of hydrogen by the photolysis of water in the presence of a catalyst (TiO_2 in this case). They proposed that the decomposition of water in the presence of UV light without an external voltage takes place according to the following reactions:-

Excitation on TiO_2 by radiation – $TiO_2 + 2h\upsilon \rightarrow 2e- + 2h^+$

At the TiO_2 electrode – $H_2O + 2h^+ \rightarrow ½\ O_2 + 2H^+$

At the Pt electrode – $2H^+ + 2e^- \rightarrow H_2$

The overall reaction is $H_2O + 2h\upsilon \rightarrow ½\ O_2 + H_2$. At present, various schemes for photolysis can be classified into two major groups. In the first, photolysis is carried out in photoelectrochemical cells using catalytic electrodes [2]. In the second group, photolysis is carried out using particulate catalysts [3]. These two basic classifications are illustrated schematically in **Fig. 1.1**.

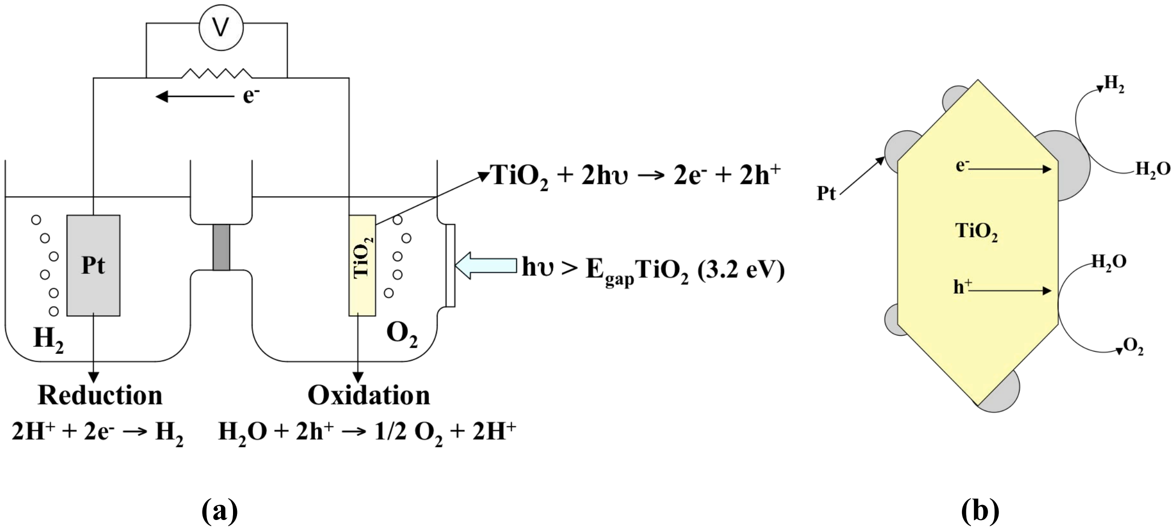

Figure 1.1 – (a) Photoelectochemical cell used by Fujishima and Honda [2] with TiO_2 and Pt electrodes. The photogenerated holes react with water on the TiO_2 surface to produce oxygen and the photogenerated electrons travel through the external circuit to the Pt electrode where they react with water to produce hydrogen. **(b)** Particulate cell with a TiO_2 particle activated by Pt [3]. The reactions involved are the same as for the photochemical cell.

The photoelectrochemical cells (PEC) are more efficient than the powdered catalysts because of spatial separation of electrons and holes in the space charge region of the semiconductor electrode that diminishes charge carrier recombination and the back reaction of the intermediate oxidized and reduced species. The same efficient separation of charge carriers and reaction products is not achieved in the particulate systems [4]. However, any process using a powdered material has the possibility to be far less expensive than any process using a PEC.

1.2 Current Research.

The current research project is aimed at combining the benefits of both of the photoelectrochemical cell and the particulate catalysts by inducing charge separation in the particulate catalysts. The idea of achieving charge separation by band bending was originally conceived by Nozik [5, 6] who proposed the concept of using photochemical diodes that consist of the two electrodes of the photoelectrochemical cell, fused together, to produce either p – n type or Schottky – type devices. Giocondi [7-9] has shown that spatial separation can also be achieved by using ferroelectric materials such as barium titanate. The internal polarization creates band bending that separates the charge carriers. It can be seen that when the ferroelectric catalyst is illuminated with radiation having enough energy to excite the electrons across the band-gap, the oxidation and reduction half cell reactions take place on different sites depending on the internal polarization field. It is, however, not known how much this coercing of electrons and holes to different sites actually increases the efficiency of the photocatalysis.

The purpose of this research is to develop a method to quantitatively determine the effect of dipolar fields on the photochemical reactivity of ferroelectric samples. It is hypothesized that as the internal polarization increases, the reactivity of the material also increases.

1.3 References.

1. [cited; Available from: http://www.hydrogennow.org/Facts/OtherUsesOfHydrogen.htm.
2. Fujishima, A. and K. Honda, Nature, 1972. **238**: p. 37-38.
3. Sato, S. and J. White, J. M. Chem. Phys. Lett., 1980. **72**(1): p. 83-86.
4. Osterloh, F.E., Chem. Mater., 2008. **20**: p. 35-54.
5. Nozik, A.J., Appl. Phys. Lett., 1977. **30**(11): p. 567-569.
6. Nozik, A.J. and R.J. Memming, Phys. Chem., 1996. **100**(31): p. 13061–13078.
7. Giocondi, J.L. and G.S. Rohrer, J. Phys. Chem. B, 2001. **105**: p. 8275-8277.
8. Giocondi, J.L. and G.S. Rohrer, Topics in Catalysis, 2008. **49**: p. 18-23.
9. Giocondi, J.L. and G.S. Rohrer, Chem. Mater., 2001. **13**: p. 241-242.

2. Background

In this chapter the concepts of ferroelectricity and photochemistry are described. The origin of dipolar fields and the domain structure in a ferroelectric material is explained. The photochemistry section includes a discussion of the representation of semiconductor and solution energy levels on the same energy scale. Thereafter, the formation of space charge layers in both the semiconductor and the solution is described. The photochemical reactions and factors affecting the reactivity are then considered. This is followed by a discussion on the use of ferroelectric materials to carry out photochemical reactions. This chapter concludes with a literature review of the application of ferroelectrics in photochemistry.

2.1 Ferroelectrics.

Pyroelectric crystals spontaneously develop polarization and dipole moments. This polarization is temperature sensitive and hence the name pyroelectric [2, 3]. Ferroelectrics are a subgroup of this class of materials. A crystal is said to be ferroelectric when there exists more than one polarization axis in the absence of an electric field and that polarization can be shifted between these axes by the application of the field [4]. Ferroelectrics are non-centrosymmetric with positive and negative charges having different centers of symmetry resulting in a polarized crystal.

2.2 Internal polarization.

In the case of Barium Titanate and other perovskite mixed oxides (ABO_3), the tetravalent B cation sits in the center of an octahedron made up of oxygen ions. At higher temperatures, the structure maintains the cubic shape and is centrosymmetric. Below a critical temperature, called the Curie temperature (T_C), the octahedral cages of oxygen distort and the positive ions shift to off-center positions resulting in a tetragonal structure. Because of this, the crystal becomes polarized [5-7]. This is depicted in **Fig. 2.1**.

This internal polarization (P_S) is not uniform throughout a ferroelectric. For instance, at the surfaces the crystal terminates and polarization becomes zero and, in the neighborhood of defects, the value of P_S may differ from that of the perfect crystal. This variation in P_S gives rise to depolarizing field. This field can be compensated by the flow of free charge in the crystal or by the free charge in the surrounding medium at the crystal surface. The depolarization field energy (W_E) is zero for a totally compensated crystal in equilibrium. However, for insulators in insulating environments, this is not readily attained. In this situation, the W_E can be large.

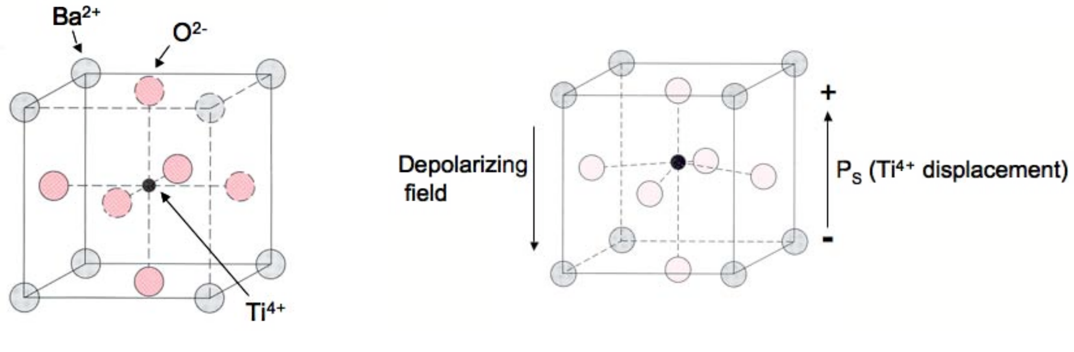

(a) **(b)**

Figure 2.1 – (a) Unit cell of $BaTiO_3$. Cubic perovskite structure. **(b)** Ferroelectric tetragonal $BaTiO_3$ with Ti^{4+} displaced in +z direction. It has offset positive and negative centers of symmetry resulting in polarization of the unit cell [5, 8].

2.3 Domain structure.

To minimize the depolarization field energy, regions of consistent polarization known as ferroelectric domains form in the crystal when cooling from the paraelectric state to the ferroelectric state so that there is no net polarization in the crystal. Because there are multiple polarization axes for ferroelectrics, while cooling through the Curie temperature, regions with different directions of polarizations nucleate within the same crystal. As a result, each grain has domains that are separated by domain walls, which are believed to be a few atomic steps thick. There is a certain amount of energy associated with the domain walls, called domain wall energy (W_W), because the walls differ from the perfect crystal. The sizes of the domains in a crystal are determined by the minimization of $W_E + W_W$ [4]. For the case of a polarized tetragonal crystal, e.g. $BaTiO_3$, the polarization is in the direction of elongation [001]. Hence, within a crystal, when one domain meets the other, the polarization directions on either side of the wall can only be either 90^o or 180^o [7].

2.4 Photochemistry.

2.4.1 *Vacuum and Hydrogen Scales of Energy.*

To interpret the experiments described in this research, it is essential to know the energy levels of the electrons and holes in the sample and of the ions in the solution. In surface science the energy of an electron at infinity (E^e) is taken to be zero. This energy level is called the “vacuum level”. The conduction band, valence band and Fermi level positions for semiconductors are usually specified with respect to this vacuum level. On the other hand, in electrochemistry, the Fermi energy of the hydrogen reference electrode under standard conditions is taken to be zero. The reduction potentials or redox potentials of different species in solution are specified with respect to this Standard Hydrogen Electrode (SHE) or Normal Hydrogen Electrode (NHE) [9]. The relation between these two zeroes of energy has been determined by extrapolation and empirical models and it has been found that the vacuum level is approximately 4.5 eV above the hydrogen reference energy [10-14]. Throughout this thesis, the hydrogen reference electrode will be taken as the zero of the energy scale.

2.4.2 *Band Bending on Semiconductor Surfaces.*

In semiconductors, surface states capture charge carriers near the surface even in vacuum to create a charged surface. When the semiconductor is immersed in a solution, two things happen. First, the surface states are affected by the interaction with the solution. Charged species from the solution adsorb on the surface due to electrostatic attraction with the charged surface and this changes the charge on the surface states. Preferential adsorption of one kind of charged species (positive or negative) creates a net charge on the surface. This can be altered by changing the pH of the solution because pH determines the availability of positively charged H^+ and negatively charged OH^- in the solution. At a specific pH there is no net charge adsorbed on the surface and it is called the “isoelectric point” or “point of zero charge” if H^+ and OH^- are the only species adsorbed. Second, equilibrium between the semiconductor and the redox couples in the solution will occur. This equilibrium is achieved by the exchange of electrons between the two so that the Fermi level of the semiconductor (E_F) is equal to the redox potential of the species in the solution (E_{redox}). If E_{redox} is higher than E_F, electrons flow from the solution to the semiconductor surface and the opposite happens when E_F is higher than E_{redox}. This transfer of electrons creates charged surfaces in the semiconductor. Due to this charge on the surface, three forms of space charge regions can form in the semiconductors as shown in **Fig. 2.2** for a n-type semiconductor. **Fig. 2.2(a)** shows the case of a negatively charged surface or the case in which electrons (majority carriers) are transferred from the semiconductor to the solution. **Fig. 2.2 (b)** shows the case in which the negatively charged surface is created due to ferroelectric polarization. In both the cases a "depletion region" is created. The surface charge compensation in the semiconductor comes from charged donor states as shown in **Fig. 2.2 (a) & (b)**. In the case of a positively charged surface or the case in which electrons are injected into the semiconductor from the solution, an "accumulation layer" forms in the semiconductor as shown in **Fig. 2.2 (c)**. An "inversion layer" as shown in **Fig. 2.2 (d)** happens when excessive depletion of electrons or majority charge carriers takes place (for example, by applying external bias). In this case the charge compensation from the donor states is not enough and the electrons are also extracted from the valence band. In other words, minority carriers are generated and excessive band bending occurs [9]. The space charge layer widths for depletion and accumulation layers are given by **Eqns. 2.1 – 2.3** [15].

For depletion layer,

$$L_{SC} = \left(\frac{2\varepsilon_o \varepsilon_r \phi_{SC}}{eN_D} \right)^{1/2} \qquad \text{---(2.1)}$$

$$Z_{acc} = \sqrt{2}\left(1 - \exp\left[-\frac{V_S}{2kT}\right]\right)L_D \qquad \text{---(2.2)}$$

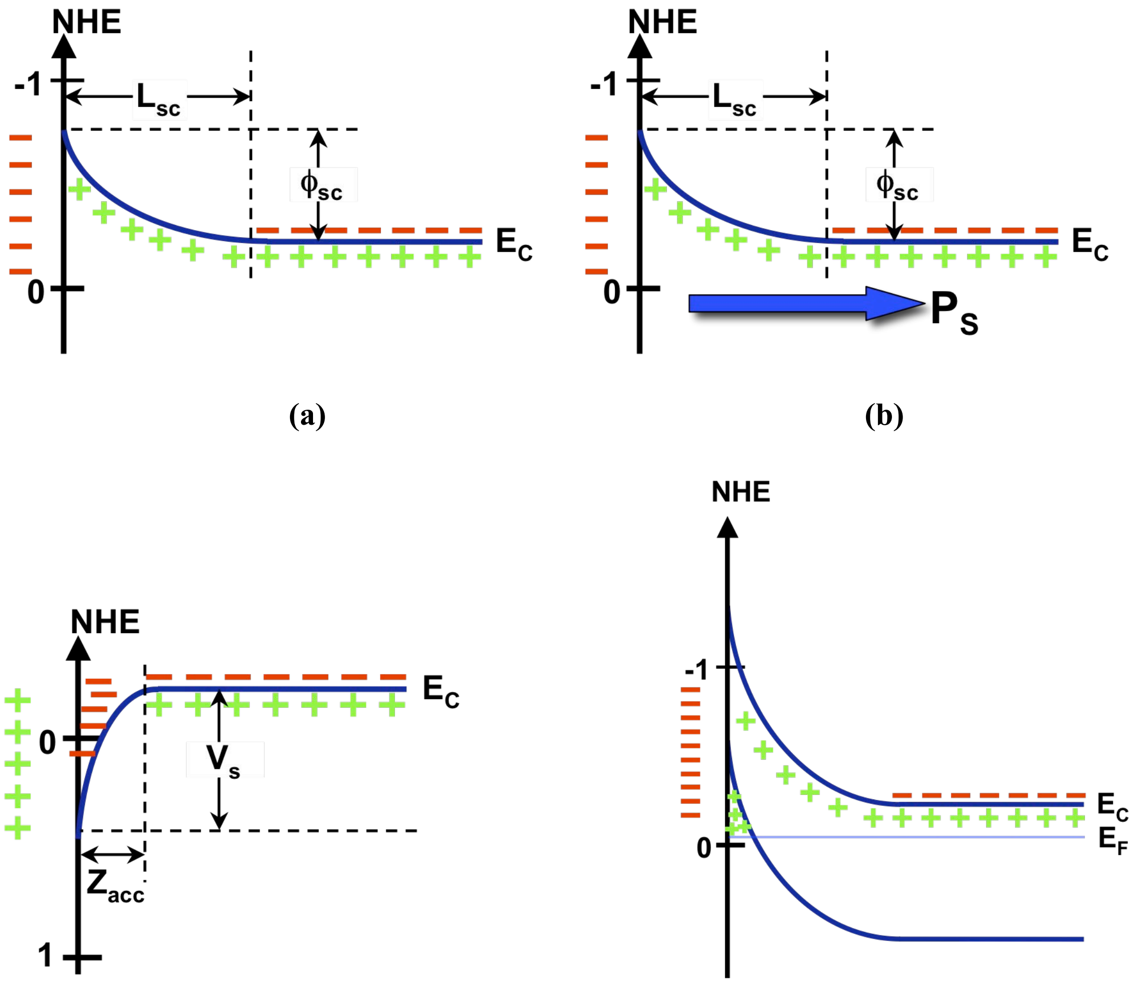

(a) (b)

(c) (d)

Figure 2.2 – Types of space charge layers in a n – type semiconductor. **(a)** Depletion layer. **(b)** Depletion layer due to ferroelectric polarization. **(c)** Accumulation layer. **(d)** Inversion layer.

where L_{SC} = Depletion space charge layer width.

Z_{acc} = Accumulation space charge layer width.

ε_o = Permittivity of free space.

ε_r = Dielectric constant.

k = Boltzmann constant.

e = elementary charge.

T = Temperature.

N_D = Donor density.

L_D = Debye length.

ϕ_{SC} = Potential drop within the depletion space charge layer.

V_S = Potential drop within the accumulation space charge layer.

Debye length of a material is given by **Eqn. 2.3**.

$$L_D = \left(\frac{\varepsilon_o \varepsilon_r kT}{e^2 N_D} \right)^{1/2} \qquad \text{---(2.3)}$$

In the case of ferroelectric materials like $BaTiO_3$, it can be assumed that the charged surfaces are created primarily due to spontaneous polarization P_S and the charge is compensated by the ionized donor states. Assuming that the free carriers do not affect the P_S, and that the value of P_S is constant through out the entire crystal of the ferroelectric semiconductor, the relation for L_{SC} is by **Eqn. 2.4** [4].

$$L_{SC} = \frac{P_S}{eN_D} \qquad \text{---(2.4)}$$

It can be seen from these four equations that the space charge layer widths and the Debye length can be altered by changing the donor density (N_D) and dielectric constant at a constant temperature.

2.4.3 ***Double Layers in the Solution.***

At the semiconductor – liquid interface, there are three double layers. First is the space charge layer in the semiconductor as explained in the previous section. Second is the charged layer between two planes – one plane that is the surface of the semiconductor where the charge is either in the surface states or at the adsorbed ions (the two cannot be distinguished because the adsorbate and the surface state are bonded by the same charged bond) and the second plane called "outer Helmholtz plane (ohp)" that is the position of the closest approach of mobile ions in the solution. This layer is called Helmholtz layer. The third layer is called "Gouy – Chapman layer" that is an extended region of space charge that compensates the charge in the semiconductor uncompensated by the Helmholtz layer. One case of these layers is shown in **Fig. 2.3** [9].

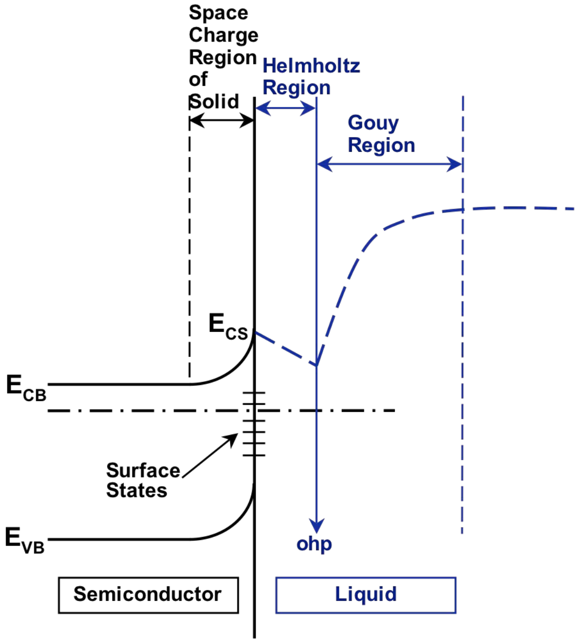

Figure 2.3 – Double layers at solid liquid interface [9]. The distances are not to scale.

2.4.4 *Band Edges on NHE scale.* [9]

To study photochemical reactions it is convenient to have all of the energy levels of the semiconductor and the solution on the same scale (NHE in this case). The conduction band edge on the NHE scale can be calculated by using **Eqn. 2.5** [16, 17]. (The procedure is also shown in **Fig. 2.4 (a)**)

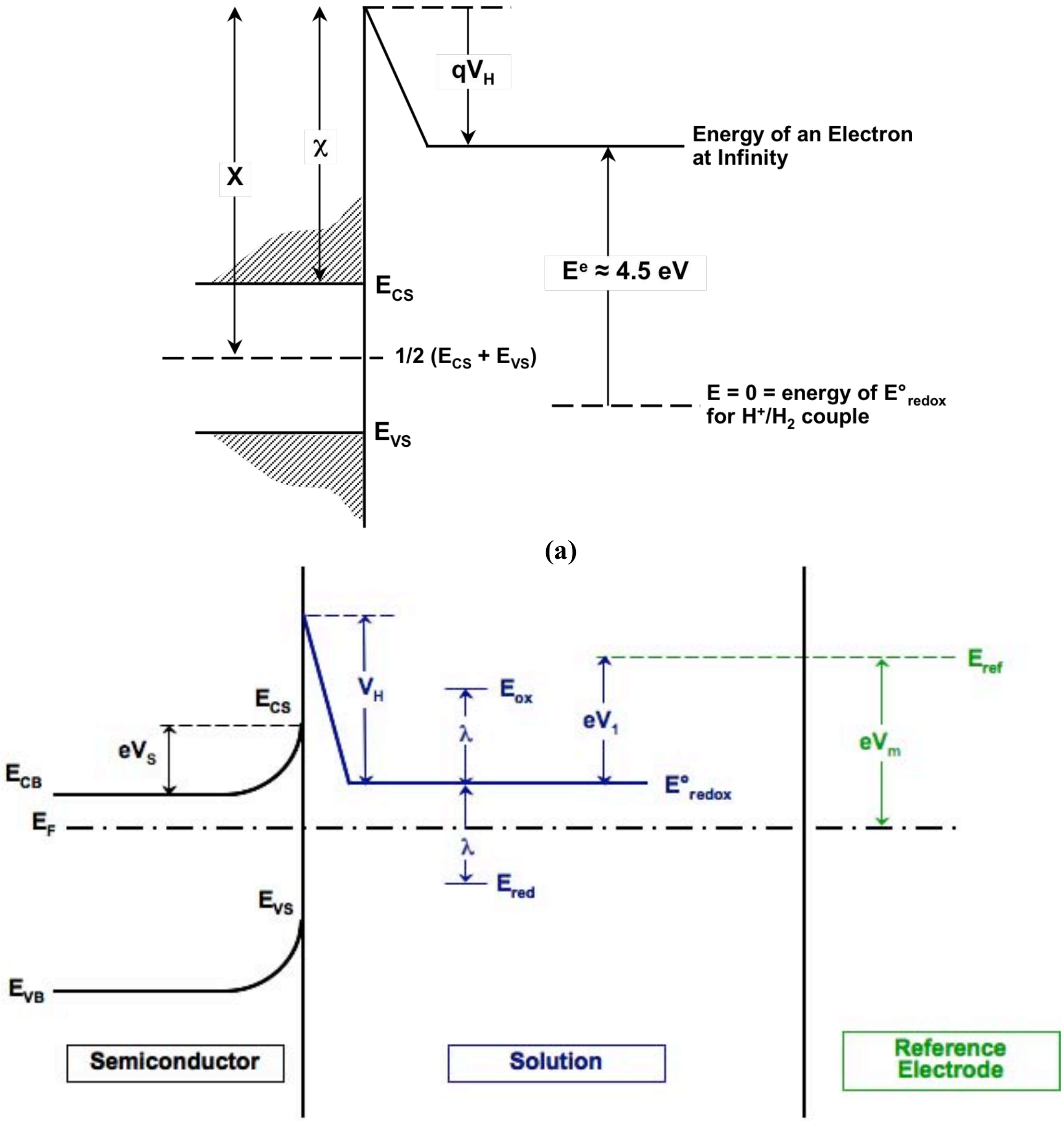

(a)

(b)

Figure 2.4 – Energy diagram to illustrate the parameters required to **(a)** theoretically calculate E_{CS} and **(b)** experimentally calculate E_{CS} [9].

$$E_{cs} = E^e - eV_H - \chi = E^o_{cs} - eV_H \qquad \text{---(2.5)}$$

where E_{CS} = Conduction band edge at the surface.

E^e = Energy of free electrons on the NHE scale.

V_H = Helmholtz potential difference or the change in potential in the Helmholz layer.

χ = Electron affinity.

E_{cs}^{o} = Conduction band edge at the point of zero charge or at $V_H = 0$.

e = elementary charge.

Electron affinity is evaluated as follows. The Mulliken electronegativity for an atom M is defined by **Eqn. 2.6**.

$$X(M) = \tfrac{1}{2}(A + I) \qquad \text{---(2.6)}$$

where A = Atomic electron affinity.

I = First ionization energy.

The values for A and I for different elements are tabulated in literature [18-22]. Sanderson showed that the electronegativity of a compound could be described as the geometric mean of the electronegativities of its component atoms [23]. For a semiconductor, the Sanderson electronegativity is the midgap energy. Therefore, the electron affinity is given by **Eqn. 2.7**.

$$\chi = X - \tfrac{1}{2}E_g \qquad \text{---(2.7)}$$

where X = Sanderson electronegativity of the semiconductor.

E_g = Band gap of the semiconductor.

The electron affinities for $BaTiO_3$ and $SrTiO_3$ estimated using **Eqns. 2.6 and 2.7** are 3.76 eV and 3.64 eV respectively (Band gaps of $BaTiO_3$ and $SrTiO_3$ are 3.0 and 3.2 respectively [24]). Since the electron affinity of $SrTiO_3$ is smaller, the conduction band edge of $SrTiO_3$ is higher than $BaTiO_3$. This is consistent with the experimental measurements [25].

Helmholtz potential difference (V_H) varies with pH of the solution according to the **Eqn. 2.8**.

$$eV_H = 2.3kT(pzc - pH) \quad \text{---(2.8)}$$

where V_H = Helmholtz potential difference or the change in potential in the Helmholz layer.

pzc = point of zero charge.

pH = pH of the solution.

k = Boltzmann constant.

T = Temperature.

e = elementary charge.

At the point of zero charge of a material, Helmholtz potential is zero.

The conduction band edge at the surface can also be estimated on the NHE scale by experimentally measuring the electrode potential (V_m), the potential difference between the semiconductor electrode and the reference electrode (**Fig. 2.4 (b)**). The electrode potential is given by **Eqn. 2.9**.

$$V_m = V_S + V_{fb} \quad \text{---(2.9)}$$

where V_m = Electrode potential.

V_S = Surface barrier or amount of band bending.

V_{fb} = Flat band potential.

The amount of band bending (V_S) can be determined experimentally from the analysis of Mott – Schottky plots. The flat band potential (V_m) is experimentally determined by directly applying a voltage in the setup shown in **Fig. 2.4 (b)** such that $V_S = 0$. The conduction band edge at the surface is related to the flat band potential as shown in **Eqn. 2.10**.

$$E_{cs} = eV_{fb} + \mu + eV_H \quad \text{---(2.10)}$$

where E_{CS} = Conduction band edge at the surface.

V_{fb} = Flat band potential.

V_H = Helmholtz potential difference or the change in potential in the Helmholz layer.

μ = Energy difference between bulk conduction band edge and Fermi energy (~ 0.1 – 0.2 eV for n-type semiconductors).

e = elementary charge.

2.4.5 *Photochemical Reactions.*

When the surface of a semiconductor is irradiated with energy greater than its band gap, photons are absorbed and electrons and holes are generated. These photogenerated charge carriers can either recombine or react with the species in the solution at the surface. For a photochemical reaction to occur, the redox potential of the reacting species in the solution should lie within the band gap of the semiconductor. This situation makes it favorable for the electron in the conduction band to reduce the species and the hole in the valence band to oxidize the species [9, 26]. Nozik [27, 28] proposed that electron – hole separation can be enhanced by band bending. He proposed the concept of photochemical diodes that consist of two electrodes of a photoelectrochemical cell fused together producing either p – n type or Schottky – type devices. The upward band bending represents a negative surface that repels the electrons but attracts the holes and the opposite of this holds true for downward band bending. As a result, the semiconductor with bent bands should react more efficiently as compared to the flat band situation. Also, more band bending and/or wider space charge layers should make the reaction more efficient. Charge carriers should be photogenerated in the region of thickness equal to or greater than the space charge layer widths at the surface because the charge carrier separation in a material occurs only in the regions of band bending. The penetration depth of the incident radiation depends on the absorption coefficient of the material and is discussed in **Section 2.4.5.1**.

The efficiency of photochemical reactions also greatly depends on the availability of photogenerated charge carriers for reaction at the surface. The absorption coefficient and efficiency of non-radiative electron transitions in a material are the two factors that strongly affect this. These two factors are discussed in the remainder of this section.

2.4.5.1 Absorption coefficient.

The intensity of incident radiation on a material decreases with distance from the surface inside the material. For liquid solutions the relation is given by **Eqn. 2.11** [29, 30] (**Fig. 2.5**).

$$A = \log I_0/I = \log 1/T = \alpha \ell c \qquad \text{--- (2.11)}$$

where A = Absorbance.

I_0 = Incident intensity.

I = Transmitted intensity.

T = Transmittance.

α = Absorptivity or Absorption coefficient of the solution (l moles^{-1} cm^{-1}).

ℓ = Path length or the distance light travels in the solution (cm).

c = Concentration of the solution (moles l^{-1}).

This relation is also called Beer's Law. The absorption coefficient, α, is a constant characteristic of the sample and the vacuum wavelength of the radiation. It is defined by **Eqn. 2.12** [29, 30].

$$\alpha = \frac{4\pi k}{\lambda} \qquad \text{---(2.12)}$$

where k = Extinction coefficient of the solution (l mole^{-1}).

λ = Wavelength of radiation in vacuum (cm).

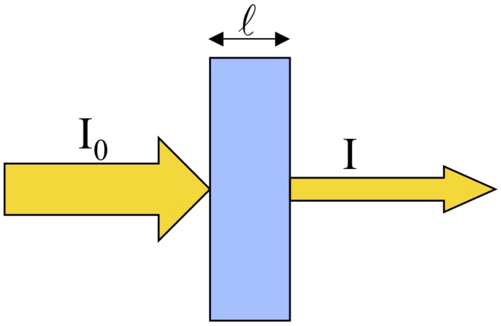

Figure 2.5 – Diagram illustrating the change in the intensity of incident radiation when transmitted through a sample of thickness ℓ.

A more detailed discussion of solutions is presented in **Section 5.2.1.1(b)**. In this section, more emphasis is given to solids. **Equations 2.11 and 2.12** can also be applied to solids with the only difference being that the concentration dependence is meaningless. Instead of the solution sample in the path of light, a thin solid sample can be imagined in **Fig. 2.5**. The only requirement is that the solid material should be thin enough to transmit incident radiation. The intensity of transmitted radiation (I) is now given by **Eqn. 2.13**.

$$I = I_0 e^{-\alpha \ell} \qquad \text{---(2.13)}$$

where I = Transmitted intensity.

I_0 = Incident intensity.

α = Absorptivity or Absorption coefficient of the material (cm^{-1}).

ℓ = Path length = thickness of the sample.

Absorption coefficient of solids is defined by **Eqn. 2.14**.

$$\alpha = \frac{4\pi k}{\lambda} \qquad \text{---(2.14)}$$

where k = Extinction coefficient of the solid sample.

λ = Wavelength of radiation in vacuum (cm).

The absorption coefficient gives the intensity of radiation of a particular wavelength after traveling 1 cm into the sample. If a material has a low value of absorption coefficient at any wavelength, it means that the radiation penetrates deeper into the material. Charge carriers are photogenerated in a material in the region near the surface where the radiation penetrates. It is one of the key factors that determine the quantum efficiency. The reason is that for the same amount of absorbed radiation (> E_g), in a more strongly absorbing material, the electrons and holes are photogenerated in a shallower region near the surface as compared to a material that has weaker absorption. In the case of the strongly absorbing material, more charge carriers will be present per unit volume and because of proximity have a higher probability of recombining. Therefore the recombination time is shorter for the electrons and holes in a more strongly absorbing material. In other words, higher absorption coefficient means shallower penetration in the material or higher recombination of electrons and holes, which is then directly related to reactivity because fewer charge carriers are available for reaction. On the other hand, if the absorption coefficient of a material is too low, the radiation penetrates much deeper in the material and more charge carriers are generated further away from the surface. The possibility of these electrons and holes reaching the surface and reacting is low and therefore fewer charge carriers are available for reaction at the surface of a weakly absorbing material. This also has an adverse effect on the photochemical reactivity. The ideal material would have all of the light absorbed in the space charge region, where carriers are efficiently separated, but also from throughout the entire space charge region. Another important factor to consider while describing this is the band gap of the materials compared. The comparison of absorption coefficients alone will be invalid if the difference in the band gaps of materials is large (say 1 eV).

The electrons and holes that are of interest in photochemical reactions are the ones at the conduction band and valence band edges, respectively. For instance, any electron generated by radiation with $h\nu > E_g$ will be at a higher energy level in the conduction band, but gives up the energy to the lattice by scattering to come to the lowest unoccupied state in the conduction band or at the conduction band edge [31]. Therefore the radiation that is of most significance is that which has energy close to the band gap of the material and hence it is at this wavelength of the radiation that the absorption coefficient is compared for different materials. Radiation with energy lower than the band gap cannot be absorbed by a material and the absorption coefficient at these wavelengths is close to zero. At wavelengths of the incident radiation corresponding to the band gap of the material, the absorption coefficient rises sharply [32] and can even be of the order 10^5 cm^{-1} for photodiode materials [33].

2.4.5.2 Efficiency of Non – Radiative Electron Transitions.

Another factor that increases the recombination rate of photogenerated charge carriers is the presence of impurities or lattice imperfections in a material. In the case of solid solutions, the addition of alloying components distorts the lattice of a material in the vicinity of the solute atoms. This lattice distortion changes the lattice vibrations of the atoms around their equilibrium positions and therefore increases the scattering of charge carriers in the material. The “mean free carrier lifetime” is defined as the average time between two consecutive collisions of electrons with the atoms as the electrons move in the lattice. For the collision of electrons with the impurities or solute atoms in the solid solution, the mean free carrier lifetime (τ_i) is given by **Eqn. 2.15** [34].

$$\tau_i = \frac{1}{N_i \sigma_i \upsilon_r} \qquad \text{---(2.15)}$$

where N_i = Concentration of impurities.

σ_i = Area an impurity atom presents to the incident electron.

υ_r = Random velocity of the electron in the lattice.

The mean free carrier lifetime is inversely proportional to the concentration of impurities. Therefore as the amount of solute increases in a solid solution, the mean free carrier lifetime decreases or the scattering increases. In other words, the increase in alloying components increases the recombination of charge carriers (higher efficiency of non-radiative electron transitions) because of increased scattering. As a result, fewer electrons and holes are available for photochemical reactions. However, if an ordered solid solution forms at a certain solute concentration, the disorder in the lattice reduces and the carrier lifetimes increase [34]. Consequently, the recombination of charge carriers is also reduced and more electrons and holes are available for the reactions.

In the case of doped semiconductors, impurities or lattice imperfections can create energy states within the band gap of a material. Any such states can act as a recombination center by a trapping charge carrier of one kind and then subsequently capturing an opposite charge carrier and annihilating the pair [32]. The direct recombination of charge carriers across the band gap is a fast process and the lifetime of electron – hole pair usually on the order of 10^{-8} seconds. This means that the emission of photons that is caused by the recombination stops approximately 10^{-8} seconds after the radiation photogenerating the charge carriers is stopped. But, if the charge carriers are trapped in these impurity / defect energy states, the emission of photons continues for longer durations after the radiation is stopped because of the delays in recombination caused by the trapping. This is called "*phosphorescence or photoluminescence*". Therefore, photoluminescence studies can provide information about the impurity states. In photoluminescence spectra of materials excited by monochromatic radiation, higher intensity luminescence or emitted radiation from a material suggests lower efficiency of non-radiative transitions or fewer impurities in the material [31].

2.5 Reactions at different surfaces in a ferroelectric material.

Internal dipolar fields create charged surfaces on ferroelectrics that cause the photogenerated charge carriers to move in opposite directions. This is called the bulk photovoltaic effect [35-40]. The electrons and holes move towards the different surfaces of the crystal and thus separate the oxidation and reduction sites [27, 28]. To explain this mechanism, a single crystal oxide particle is shown schematically in **Fig. 2.6**. The particle is assumed to have dipolar fields that arise either from ferroelectric domains, as in the case of $BaTiO_3$, or polar surface terminations as in the case of $SrTiO_3$ (**Fig. 2.7**). The type of reaction that occurs on a surface is determined by the way in which the bands bend at the surface. As demonstrated in **Fig. 2.6,** a surface that is negatively charged repels electrons and, as a result, the electrons face a potential barrier for coming to the surface. This barrier is represented by upward band bending in the space charge region. It is, however, easier for the holes to move to the surface in this situation and oxidation of the reactant can occur. On the other hand, if the surface has a positive charge, one of the following two things can happen, depending on the amount of positive charge on the surface of an n-type semiconductor such as $BaTiO_3$ and $SrTiO_3$. The bands can still be bent upwards (**Fig. 2.6 (a)**) but the upward band bending will decrease and the bands may even become flat as the amount of positive charge increases on the surface. In other words, the bands on the surface will be bent upwards until the positive charge on the surface balances the excess negative charge of the n-type semiconductor on the surface. On such surfaces, only electrons with sufficient energy to overcome the energy barrier of upward band bending have the possibility of reaching the surface and participating in the reaction [26]. However, as long as the barrier is reduced by polarization, more electrons

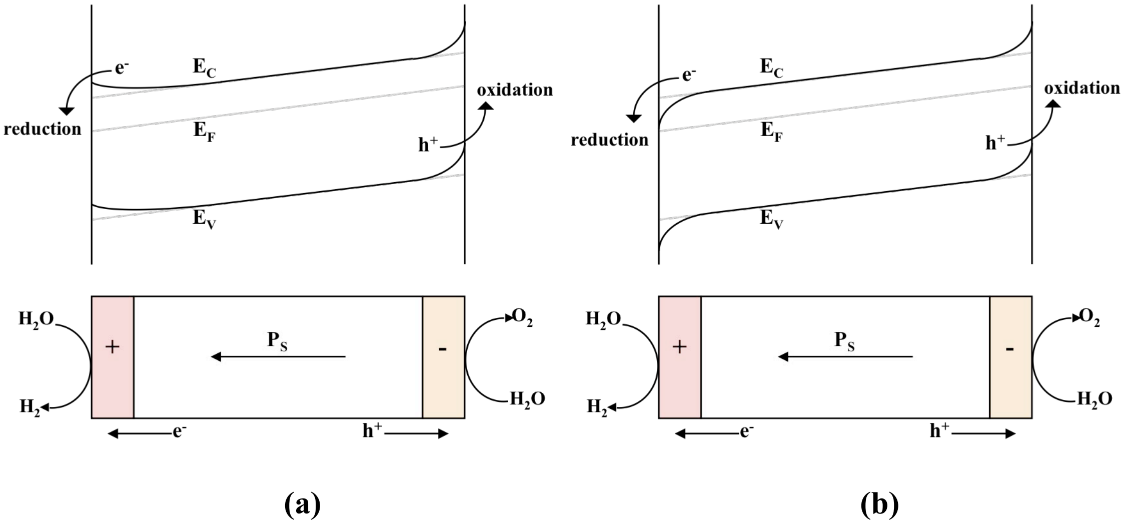

Figure 2.6 – Band bending in a polarized crystal. **(a)** Band bending due to insufficient positive surface charge. **(b)** Band bending for the crystal in the case of net positively and negatively charged surfaces. Reduction occurs on the positively charged surface and oxidation on the negatively charged one.

will reach the surface than in the case without polarization. If the positive charge on the surface increases further, it will create a surface with a net positive charge and the bands will bend downwards and electrons can move easily towards the surface (**Fig. 2.6 (b)**). Hence, reduction occurs in both these cases [26]. In other words, charge carriers that are generated by the illumination of the material are driven to opposite ends of the crystal due to the effect of the internal field. As a result, reduction occurs on the positive end and oxidation occurs on the negative end.

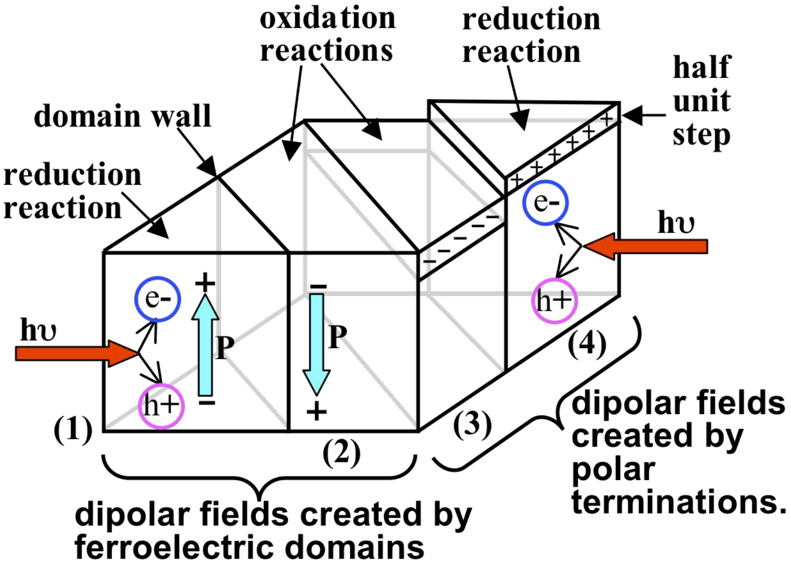

Figure 2.7 - Schematic model for the effect of internal polarizations on photochemical reactions. (1) & (2) depict dipolar fields created by ferroelectric domains and (3) & (4) are the ones created by polar terminations [41].

The work reported by Giocondi *et al.* [41, 42] supports this description. Atomic force microscopy (AFM) images of (001) surface of $BaTiO_3$ are shown in **Fig. 2.8 (a)** after photochemical reduction of Ag ($Ag^+ + e^- \rightarrow Ag$) and **(b)** after the photochemical oxidation of Pb ($Pb^{2+} + 2H_2O + 2h^+ \rightarrow PbO_2 + 4H^+$). It can be seen that Ag and PbO_2 deposit on complimentary domains on macroscopic crystals. It was also observed that Ag accumulates on the surfaces that have positive charge whereas PbO_2 accumulates on the ones that are negatively charged, which is in accordance with the above mentioned theory.

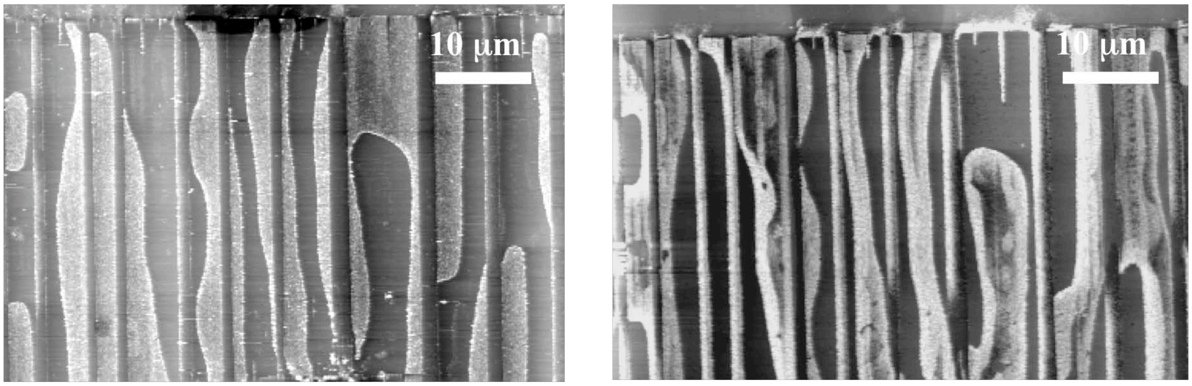

(a) **(b)**

Figure 2.8 - Topographic AFM images of the {001} surface of a $BaTiO_3$ single crystal. **(a)** after Ag reduction and **(b)** after Pb oxidation [41].

This effect held true even in the case of fine powders shown in **Fig. 2.9**. Faceted $BaTiO_3$ crystals are shown in **Fig. 2.9 (a) and (b)** before and after silver deposits from an aqueous solution. It was observed that Ag deposits primarily on {001}-type facets. It can be assumed that the silver accumulated on the (001) surfaces of the crystals toward which the positive end of the polarization vector points [1]. In other words, this is the cathodic end (left side end) of the crystal schematic shown in **Fig. 2.7**.

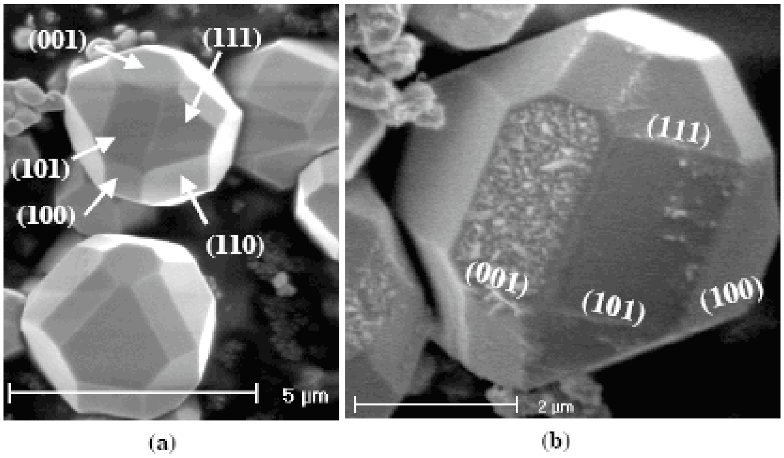

Figure 2.9 - (a) SEM image of $BaTiO_3$ crystals **(b)** After using the crystals to reduce Ag from an aqueous $AgNO_3$ solution, Ag (white contrast) is selectively deposited on the (001) face, which is the reducing end of this crystal [1]

2.6 Ferroelectrics in Photochemistry – literature review.

Inoue [43, 44] studied a series of barium titanates ($BaTi_4O_9$, $Ba_2Ti_9O_{20}$, $Ba_4Ti_{13}O_{30}$ and $Ba_6Ti_{17}O_{40}$) activated with nanosized RuO_2 for photocatalytic production of H_2 from water. $BaTi_4O_9$ has TiO_6 octahedra arranged in such a way that they form pentagonal prism tunnels that are occupied by barium ions. Of all the barium titanates studied, only $BaTi_4O_9$ has this tunnel structure [45-48]. Also, only $BaTi_4O_9$ has heavily distorted TiO_6 octahedra due to Ti displacement that give rise to dipole moments in these TiO_6 octahedra. The comparison of the rate of H_2 production for all of these barium titanates after activation with RuO_2 showed that $BaTi_4O_9$ was quite reactive while the others produced H_2 in very small amounts. Inoue [44] proposed that this high reactivity could be attributed to the dipolar fields present in the TiO_6 octahedra that promoted the separation of charge carriers on photoexcitation.

Inoue *et al.* [49] also studied the rate of hydrogen production for RuO_2 activated $M_2Ti_6O_{13}$ (M = Na, K, Rb, Cs). $M_2Ti_6O_{13}$ (M = Na, K, Rb) compounds have a tunnel structure and the shape of the tunnel is rectangular [50, 51]. $Cs_2Ti_6O_{13}$, however, has a layered structure [52]. All these materials except $Cs_2Ti_6O_{13}$ have heavily distorted TiO_6 octahedra [50-52] and therefore strong dipolar fields like $BaTi_4O_9$. They found that all these RuO_2 / $M_2Ti_6O_{13}$ except $Cs_2Ti_6O_{13}$ produced hydrogen from water with the photocatalytic activity decreasing in the order Na>K>Rb>>Cs or with increasing size of the cation [49]. Based on these observations Inoue *et al.* [3] proposed that the origin of photochemical activity was the same for all these compounds that produced hydrogen although the shape of the tunnels was different. Also the high rate of production of H_2 was because of the presence of dipolar fields.

Recently, Jones *et al.* [53, 54] have studied the photochemical behavior of ferroelectric lead zirconium titanate (PZT) thin films by reacting them with different metal salt solutions. They observed that the photochemical behavior of PZT is strongly dependent on the exact position of the conduction band edge and the redox potential of the salt used [53]. Depending on the redox potential of the salt used with respect to the conduction band edge of the PZT, either metal deposits on positive domains or the photodecomposition of the negative domains takes place. For certain cations such as Fe^{2+} whose redox potential is close to the conduction band edge of PZT, they observed that either of the two processes can happen depending on how the PZT samples are prepared. They attribute this effect to the uncertainty in the position of conduction band edge because it depends on the surface states on each sample [54].

Jones *et al.* [55] have also studied the effect of the energy of incident radiation on the photochemistry of PZT. They photochemically reduced aqueous Ag^+ from a $AgNO_3$ solution to get nanoclusters of Ag on the PZT surface. It was observed that when the energy of the incident radiation was increased, the cross-sectional size of the Ag particles on the surface increased. This was attributed to the fact that higher energy photons excite more electrons from deeper in the valence band of the material where the density of states is higher. This allows a greater reduction rate of Ag^+ at the surface.

Jones *et al.* [55, 56] also the onset of Ag cluster formation varies with orientation. They also propose that the formation of individual Ag clusters is due to the interactions taking place in the Helmholtz layer and its disturbance during UV illumination at points of higher relative potential to their surroundings (for e.g. grain boundaries). Dunn *et al.* [57] also observed that the amount of Ag deposited depends on the orientation. Since the value of remnant polarization varies with orientation, they attribute this change in reactivity to the change in polarization. Dunn *et al.* [58] have demonstrated that it is possible to deposit Ag clusters on negative domains of PZT that normally do not reduce silver by sufficiently increasing the energy of the incident photons (greater than 1 eV over the band gap). They propose that with the increasing rate of charge carrier generation, the excess charge carriers tend to accumulate in the corresponding space charge regions (electrons in positive domains and holes in negative domains). This results in the reduction of the width of the depletion region and an increase in the band bending near the surface. However in this case the electrons can now tunnel across the negatively charged surface and react to form Ag clusters. They have reported that the rate of growth of Ag clusters on negative domains is approximately half the rate of growth on the positive domains [58].

Kalinin *et al.* [59, 60] have proposed the spatially selective photochemical deposition of metals on ferroelectric domains to be a new way of producing nanostructures. They patterned domains on the PZT surface using a biased Atomic Force Microscope tip and photochemically deposited Ag on the patterns. They consider this to be a promising method for nanodevice integration.

Ohara *et al.* [61] studied the ferroelectric to non – ferroelectric transition in $Sr_xBa_{1-x}TiO_3$ epitaxial thin films (~50 nm thick) grown on $LaAlO_3$ (001) substrates by the photochemical reduction of silver. They compared the amount of silver metal photochemically reduced from aqueous $AgNO_3$ solutions on $Sr_xBa_{1-x}TiO_3$ films of different compositions by X – ray fluorescence. The band gap of the $Sr_xBa_{1-x}TiO_3$ films was also measured. They observed that the amount of silver and the band gap of Sr_xBa_{1-}

${}_{x}TiO_3$ thin films show an abrupt change near the $Sr_{0.4}Ba_{0.6}TiO_3$ composition that has the Curie temperature near the room temperature. This behavior near the ferroelectric transition was attributed to the coexistence of paraelectric and ferroelectric domains in the $Sr_xBa_{1-x}TiO_3$ thin films with $0.3<x<0.5$.

2.7 References.

1. Giocondi, J.L. and G.S. Rohrer, Topics in Catalysis, 2008. **49**: p. 18-23.
2. Buchanan, R.C. and M. Dekker, *Ceramic Materials For Electronics- processing, properties and applications*. 1986, New York and Basel: INC.
3. Kaneko, M. and I. Okura, *Photocatalysis Science and Technology*. 2003, New York: Spriniger.
4. Lines, M.E. and A.M. Glass, *Principles and Applications of Ferroelectrics and Related Materials*. 1977, Oxford: Clarendon Press.
5. Forsbergh, P.W., Phys. Rev., 1949. **75**.
6. Forsbergh, P.W., Phys. Rev., 1949. **76**: p. 1187.
7. Braithwaite, N. and G. Weaver. Materials in action series - Electronic Materials inside electronic devices. 1998, London, England: Alden Press (London & Northampton) Ltd.
8. W.D. Callister, J., *Materials Science and Engineering: An Introduction*. 2000, New York: John Wiley and Sons, Inc.
9. Morrison, S.R., *Electochemistry at Semiconductor and Oxidized Metal Electrodes*. 1980, New York: Plenum Press.
10. Noyes, R.R., J. Am. Chem. Soc., 1962. **84**.
11. F.Lohmann and Z. Naturforsch, 1967. **22A**.
12. Trasatti, S., J. Electroanal. Chem., 1974. **52**.
13. Hansen, W.N. and D.M. Kolb, J. Electroanal. Chem., 1979. **100**.
14. Gomer, R. and G. Tryson, J. Chem. Phys., 1977. **66**.
15. Monch, W., *Electronic Properties of Semiconductor Interfaces*. 2004, New York: Springer-Verlag Berlin Heidelberg.
16. Butler, M.A. and D.S. Ginley, J. Electrochem. Soc., 1978. **125**.
17. Frese, K., J. Vac. Sci. Technol., 1979. **16**.
18. Hotop, H. and W.C. Lineberger, J. Phys. Chem. Ref. Data, 1985. **14**.
19. David, R.L., *CRC Handbook of Chemistry and Physics,84th Ed*. 2003, Boca Raton, Florida: CRC Press.
20. Andersen, H.H., et al., Phys. Rev. A, 1997. **55**: p. 3247-3249.
21. Ilin, R.N., V.I. Sakharov, and I.T. Serenkov, Opt. Spectros. (USSR), 1987. **62**.
22. Dellwo, J., et al., Phys. Rev. A, 1992. **45**: p. 1544-1547.
23. Sanderson, R.T., *Chemical Periodicity*. 1960, New York: Reinhold.
24. Cardona, M., Phys. Rev. A, 1965. **140**: p. 651.
25. Dwight, K. and A. Wold, Am. Chem. Soc., 1981. **146**: p. 207 - 216.

26. Bard, A.J. and L.R. Faulkner, *Electrochemical Methods Fundamentals and applications*. 2nd edition ed. 2001: John Wiley & Sons, Inc.
27. Nozik, A.J., Appl. Phys. Lett., 1977. **30**(11): p. 567-569.
28. Nozik, A.J. and R.J. Memming, Phys. Chem., 1996. **100**(31): p. 13061–13078.
29. Beer, A., Ann. Physik. Chem., 1852. **2**(86): p. 78.
30. Bauman, R.P., *Absorption Spectroscopy*. 1962: John Wiley & Sons, Inc.
31. Streetman, B.G. and S. Banerjee, *Solid State Electronic Devices, 5th edition*. 2005: Prentice Hall.
32. Sze, S.M., *Physics of Semiconductor Devices, 2nd edition*. 2001: John Wiley & Sons Inc.
33. Melchior, H., *Demodulation and Photodetection Techniques in F. T. Arecchi and E. O. Schulz-Dubois Laser Handbook, Vol. 1*. 1972, North-Holland, Amsterdam.
34. Omar, M.A., *Elementary Solid State Physics : Principles and Applications*. Addison - Wesley Series in Solid State Sciences. 1975, USA: Addison - Wesley Publishing Company, Inc.
35. Brody, P.S., Solid State Commun., 1973. **12**: p. 673-676.
36. Glass, A.M. and D.v.d. Linde, Appl. Phys. Letters, 1974. **25**: p. 233-235.
37. Brody, P.S. and F. Crowne, J. Elect. Mater., 1975. **4**: p. 955-971.
38. Brody, P.S., J. Solid State Chem., 1975. **12**: p. 193-200.
39. Baltz, R.V., Phys. Stat. Sol. (b), 1978. **89**: p. 419-429.
40. Fridkin, V.M., Ferroelectrics, 1984. **53**: p. 169-187.
41. Giocondi, J.L. and G.S. Rohrer, J. Phys. Chem. B, 2001. **105**: p. 8275-8277.
42. Giocondi, J.L. and G.S. Rohrer, Chem. Mater., 2001. **13**: p. 241-242.
43. Inoue, Y., et al., J. Chem. Soc. Commun., 1992.
44. Kohno, M., et al., J. Chem. Soc. Faraday Trans., 1998. **94**.
45. Templeton, D.H. and C.H. Dauben, J. Chem. Phys., 1960. **32**.
46. Tillmanna, E. and W.H. Bauer, Acta Crystallogr.Sect B, 1970. **Sect B**.
47. Fallon, G.D. and B.M. Gatehouse, J. Solid State Chem., 1983. **49**.
48. Tillmanns, E., Inorg. Nucl. Chem. Lett., 1971. **7**.
49. Ogura, S., et al., Phys. Chem., 1999. **1**.
50. Andesson, S. and A.D. Wadsley, Acta. Crystallogr., 1962. **15**.
51. Cid-Dresdner, H. and M.J. Bueger, Z. Krist, 1962. **117**.
52. Grey, I.E., I.C. Madsen, and J.A. Watts, J. Solid State Chem., 1985. **58**.
53. Jones, P.M. and S. Dunn, Nanotech., 2007. **18**: p. 1-6.
54. Jones, P.M., D.E. Gallardo, and S. Dunn, Chem. Mater., 2008. **20**: p. 5901-5906.
55. Jones, P.M. and S. Dunn, J. Phys. D: Appl. Phys., 2009. **42**: p. 1-5.
56. Dunn, S., S. Sharp, and S. Burgess, Nanotech., 2009. **20**: p. 1-6.
57. Dunn, S., et al., J. Mater. Chem., 2007. **17**: p. 4460-4463.
58. Dunn, S., P.M. Jones, and D.E. Gallardo, J. Am. Chem. Soc., 2007. **129**(28): p. 8724-8728.
59. Kalinin, S.V., et al., Nano Lett., 2002. **26**: p. 589-593.
60. Kalinin, S.V., et al., Adv. Mater., 2004. **16**: p. 795-799.
61. Ohara, K., et al., Jap. J. of Appl. Phys., 2006. **45**(11): p. L339 – L342.

3. Materials used in this research.

Before going into the details of the experiments, it is important to discuss the structure and properties of the materials used in this research.

3.1 $BaTiO_3$.

Barium titanate has a Curie temperature of 120 °C. It has a cubic perovskite structure (**Fig. 2.1**) at $T > 120$ °C and a tetragonal structure at $T < 120$ °C (Polarization P_S is 26 μC/cm^2 at 23 °C) [2, 4, 5]. Lattice parameters of the tetragonal phase are reported as $a = 3.994$ Å and $c = 4.038$ Å [6]. At 5 °C $BaTiO_3$ transforms from a tetragonal structure to an orthorhombic structure and to a rhombohedral structure at -90 °C [7]. The band gap E_g of ferroelectric $BaTiO_3$ is 3 – 3.2 eV at room temperature [8, 9].

For tetragonal $BaTiO_3$ crystals, P_S is in the direction of elongation as is shown in **Fig. 2.1**. The [001] direction or the c-axis is taken to be the dipole direction in each domain. Hence P_S can point in ± x, y or z directions. At the domain walls, where one domain meets the other, the angles between the P_S on either side of the wall can only be either 90° or 180°. **Fig. 3.1** depicts a schematic domain structure of a typical $BaTiO_3$ crystal.

The charges on the surfaces are determined by the P_S and in this case {100} planes are the ones that are charged. The 90° domain boundaries lie on the {110} planes. They show up as straight lines on {100} surfaces. The 180° boundaries are confined only to the zone of planes containing the <001> direction and therefore they appear as curved lines on the {100} surfaces [10]. Some other properties of $BaTiO_3$ are presented in **Table 3.1**.

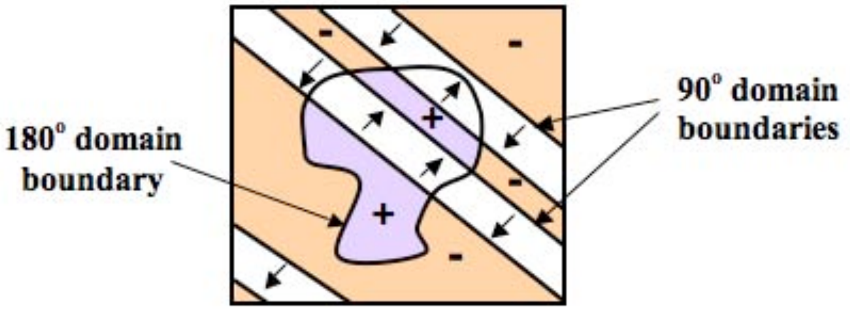

Figure 3.1 - Schematic of the $BaTiO_3$ domain structure. The + represents polarization vectors that point in the +z direction, the – represents those that point in the –z direction, and the arrows correspond to x and y lateral directions [11].

3.2 $SrTiO_3$.

$SrTiO_3$ has a cubic perovskite structure **(Fig. 3.2)** with lattice parameter a = 3.905 Å [6]. The band gap is reported to be in the range of 3.2 – 3.6 eV at room temperature [8, 9]. Non-ferroelectric phase transformations occur in $SrTiO_3$ at very low temperatures (-168 °C) that involve oxygen-cage tilting. Theoretically, a ferroelectric phase transformation is expected at about -238 to -233 °C [3], but both of these transformations are of no significance in this research as the experiments are conducted at much higher temperatures (~ 20 °C).

Unlike $BaTiO_3$, there is no polarization in bulk $SrTiO_3$. However there are polar terminations of some planes of the $SrTiO_3$ crystal that result in charged surfaces. The {100} surfaces terminate in either SrO or TiO_2 planes, both of which are neutral and hence the {100} planes are non-polar. On the other hand, {110} and {111} planes terminate in either $SrTiO^{4+}$ or O_2^{4-} and Ti^{4+} or SrO_3^{4+} planes and are hence polar. These charged surfaces then give rise to dipolar fields as shown in **Fig. 2.7** [12]. This effect is however limited to regions very close to the surface and the properties of the bulk are entirely different. Some other properties of $SrTiO_3$ are presented in **Table 3.1**.

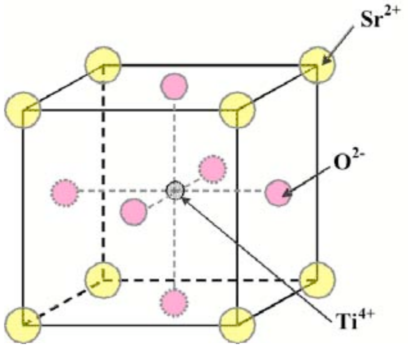

Figure 3.2 – Unit cell of $SrTiO_3$.

Table 3.1 – Electronic, optical and chemical properties of $BaTiO_3$ and $SrTiO_3$.

Property / Composition	**Donor Density cm^{-3}**	**Electron Affinity* eV**	**IEP / PZC[#] pH**	**Flat Band Potential (V_{fb})[❖] eV**	**Absorption Coefficient (α)** cm^{-1}**
$BaTiO_3$	10^{19} [13, 14]	3.76	2.5 – 11 [15-21]	-0.85 – -1.15 [22-25]	40-50 [26]
$SrTiO_3$	10^{19} [27]	3.64	8.6 [28]	-0.61 [29]	10-20 [30]

* Calculated using **Eqns. 2.6 & 2.7**. Values of A and I are taken from Ref. [31-34].

[#] IEP – Isoelectric Point, PZC – Point of Zero Charge.

[❖] Flat band potential at pH 13.

** The values of α for $BaTiO_3$ and $SrTiO_3$ are at wavelengths corresponding to their respective band gaps [26]. The value of α is given as a range because in the plot of α vs. wavelength (commonly used in the literature to study the optical properties of materials) value of α increases sharply for a small change in wavelength. It is therefore extremely difficult to accurately judge where the absorption edge lies. The range here is an estimated range of α near the absorption edge.

3.3 $Sr_xBa_{(1-x)}TiO_3$.

$BaTiO_3$ and $SrTiO_3$ are completely soluble in each other and form homogeneous solid solutions through the entire composition range in the temperature range that is used in this research (from room temperature to 1470 °C which is the highest sintering temperature used). No ordered phases have been reported at any composition in the $Sr_xBa_{1-x}TiO_3$ system [6, 35]. The Curie temperature in $Sr_xBa_{1-x}TiO_3$ decreases linearly with increasing Sr content, as seen in **Fig. 3.3** [1-3]. In other words, the phase transformation from the ferroelectric to non-ferroelectric phase can be observed at any temperature (between the T_C values of $BaTiO_3$ and $SrTiO_3$) by altering the composition of $Sr_xBa_{1-x}TiO_3$. The composition of $Sr_xBa_{1-x}TiO_3$ with $x \approx 0.26$ has T_C at room temperature (24 °C). This phase transformation also corresponds to a peak in dielectric constant at the transition composition. The dielectric constants for the $Sr_xBa_{1-x}TiO_3$ transition composition, $BaTiO_3$ and $SrTiO_3$ have been reported to be 11000, 2000 [36] and 300 [35, 37], respectively.

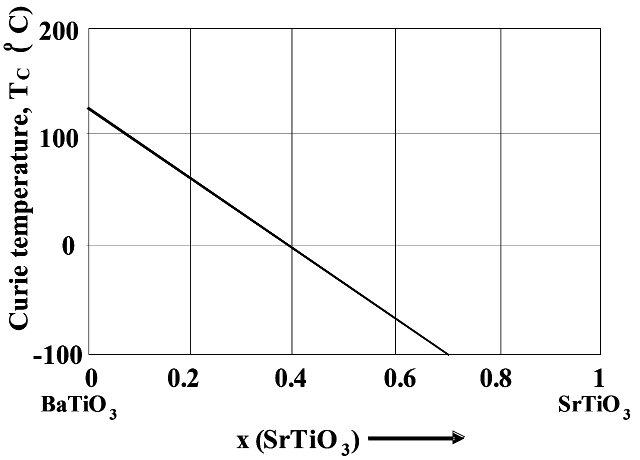

Figure 3.3 - Curie temperature (T_C) of $Sr_xBa_{(1-x)}TiO_3$ as a function of stoichiometry[1-3].

3.4 Methylene Blue Dye and Silver Nitrate.

Methylene blue is an acid – base dye that changes color on changing its oxidation state. The color change reaction is shown in **Fig. 3.4** [38]. The redox potential for a 10 μM solution of methylene blue is +0.011 eV on NHE scale at pH 7 [39]. It is very close to H_2/H^+ redox potential (= 0 eV on NHE scale) and lies within the band gap of the $Sr_xBa_{1-x}TiO_3$ as seen in **Fig. 3.5**.

The silver nitrate reduction potential is +0.8 eV [40] and it also lies within the band gap of $Sr_xBa_{1-x}TiO_3$ as shown in **Fig. 3.5**. Giocondi [12, 41-43] has shown that when $SrTiO_3$ and $BaTiO_3$ photochemically react with aqueous $AgNO_3$ solutions, solid silver is left at the site of the reaction. We assume the same process will occur for the $Sr_xBa_{1-x}TiO_3$ solid solutions.

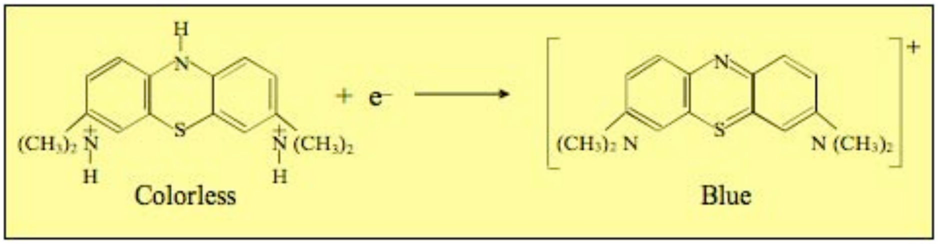

Figure 3.4 – Color changing reacting of methylene blue dye.

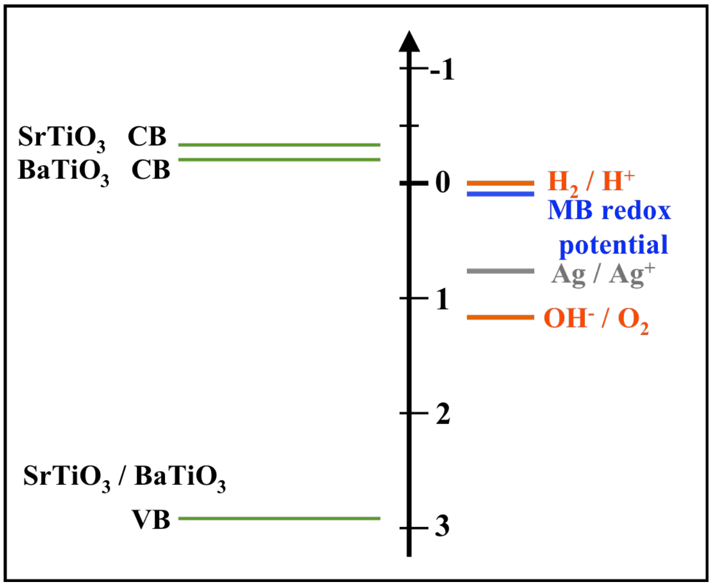

Figure 3.5 – Conduction band and valence band edge positions (flat band condition) of $BaTiO_3$ and $SrTiO_3$ with respect to the redox potentials of hydrogen, methylene blue, silver and oxygen on the NHE scale.

3.5 References.

1. Remmel, T., R. Gregory, and B. Baumert, *Characterization of Barium Strontium Titanate Films Using XRD.* JCPDS-International Centre for Diffraction Data 1999: p. 38-45.
2. Naik, R., et al., Phys. Rev. B, 2000. **61**(17): p. 11367-11372.
3. Lines, M.E. and A.M. Glass, *Principles and Applications of Ferroelectrics and Related Materials*. 1977, Oxford: Clarendon Press.
4. Forsbergh, P.W., Phys. Rev., 1949. **76**: p. 1187.
5. Burfoot, J.C. and D.V. Nostrand. Ferroelecrics: An Introduction to the Physical Properties. 1967, London: Company Ltd.
6. Basmajian, J.A. and R.C.D. Vries, J. Am. Ceram. Soc., 1957. **40**: p. 373.
7. Kwei, G.H., et al., J. Phys. Chem., 1993. **97**: p. 2368.
8. Cardona, M., Phys. Rev. A, 1965. **140**: p. 651.
9. Wemple, S.H. and M. DiDomenico, Phys. Rev. B, 1971. **3**: p. 1338.
10. Hu, Y.H., et al., J. Am. Ceram. Soc., 1986. **69**: p. 594.
11. Giocondi, J.L., in *MSE*. 2003, Carnegie Mellon University: Pittsburgh.
12. Giocondi, J.L. and G.S. Rohrer, J. Am. Ceram. Soc., 2003. **86**(7): p. 1182-1189.
13. Remeica, J.P., J. Am. Chem. Soc., 1954. **76**: p. 940.
14. Nishioka, A., K. Sekikawa, and M. Owaki, J. Phys. Soc. (Japan), 1956. **11**: p. 180.
15. Paik, U. and V.A. Hackley, J. Am. Ceram. Soc., 2000. **83**(10): p. 2381-2384.
16. Kosmulski, M., J. of Coll. and Interf. Sc., 2004. **275**: p. 214-224.
17. Jean, J.H. and H.R. Wang, J. Am. Ceram. Soc., 1998. **81**: p. 1589.
18. al., Y.-L.S.e., Powder Technology, 2005. **155**: p. 26-32.
19. Vamvakaki, M., et al., J. Mater. Chem., 2001. **11**: p. 2437-2444.
20. Wang, X.Y., et al., Mat. Res. Bull., 2000. **35**: p. 2555-2563.
21. Lewis, J.A., J. Am. Ceram. Soc., 2000. **83**(10): p. 2341-2359.
22. Butler, M.A. and D.S. Ginley, Chem. Phys. Lett., 1977. **47**.
23. Butler, M.A. and D.S. Ginley, J. Electrochem. Soc., 1977. **125**.
24. Bolts, J.M. and M.S. Wrighton, J. Phys. Chem., 1976. **80**.
25. Kung, H.H., et al., J. Appl. Phys., 1977. **48**.
26. Berglund, C.N. and H.J. Braun, Phy. Rev., 1967. **164**(2): p. 790-799.
27. Mattheiss, L.F., Physical Review B, 1972. **6**(12): p. 4718-4740.
28. Reichman, B. and B. Mich. 1985: USA
29. Dwight, K. and A. Wold, Am. Chem. Soc., 1981. **146**: p. 207 - 216.
30. Noland, J.A., Phys. Rev., 1954. **94**(3): p. 724.
31. Hotop, H. and W.C. Lineberger, J. Phys. Chem. Ref. Data, 1985. **14**.
32. Dellwo, J., et al., Phys. Rev. A, 1992. **45**: p. 1544-1547.
33. Ilin, R.N., V.I. Sakharov, and I.T. Serenkov, Opt. Spectros. (USSR), 1987. **62**.
34. Andersen, H.H., et al., Phys. Rev. A, 1997. **55**: p. 3247-3249.
35. Nowotny, J. and M. Rekas, Key Engineering Materials, 1992. **66-67**: p. 45-144.
36. Ding, S., et al., Acta Chimica Sinica, 2006. **64**(12): p. 1243-1247.
37. Choudhury, B.K., K.V. Rao, and R.N.P. Choudhury, J. Mater. Sci., 1989. **24**: p. 3469 – 3474.
38. Leventis, N. and M. Chen, Chem. Mater., 1997. **9**: p. 2621-2631.
39. Rao, P.S. and A. Hayon, The J. of Phys. Chem., 1973. **77**(23): p. 2753-2756.

40. Lide, D.R., *CRC Handbook of Chemistry and Physics*. 2007: CRC Press.
41. Giocondi, J.L. and G.S. Rohrer, J. Phys. Chem. B, 2001. **105**: p. 8275-8277.
42. Giocondi, J.L. and G.S. Rohrer, Topics in Catalysis, 2008. **49**: p. 18-23.
43. Giocondi, J.L. and G.S. Rohrer, Chem. Mater., 2001. **13**: p. 241-242.

4. Research objectives.

4.1 Hypothesis.

Taking a step ahead after knowing that the reduction and oxidation half-cell reactions indeed occur on different locations in the ferroelectric photocatalysts, it will be of interest to see if there is a significant change in the reactivity of a ferroelectric sample as compared to that of a non-ferroelectric one. It is hypothesized that ferroelectric crystals are photochemically more reactive than non-ferroelectric crystals with a similar structure and composition. The main objective of this research is to test this hypothesis.

However, the presence of dipolar field isn't the only factor that affects the photochemical reactivity. The dielectric constant, donor density, band gap, absorption depth, efficiency of non-radiative transition, and pH of the solution also influence reactivity. The dielectric constant and donor density affect the Debye length and space charge layer widths in a material [1] which in turn affect the charge carrier separation in the material and hence the reactivity. Longer Debye lengths and space charge layer widths imply that a greater number of photogenerated charge carriers are separated, their recombination probability is lower and the reactivity of the material is higher. Materials with wider band gaps absorb fewer photons than the materials with narrower band gaps when illuminated by the same radiation and, therefore, fewer charge carriers are generated. This leads to different photochemical reactivities. The absorption depth influences reactivity because it affects the fraction of charge carriers generated in the space charge region and the overall density of photogenerated charge carriers. For maximum reactivity, the fraction of charge carriers generated in the space charge region should be maximized while minimizing density of charge carriers. Alloy scattering in solid solutions and impurity or defect states in the band gap of a material increase the recombination of charge carriers and increase the efficiency of non-radiative transitions thereby reducing the number of electrons and holes available for reaction at the surface [2, 3]. As explained in **Section 2.4.5**, for a reaction to occur, the redox potential of the reacting species should lie within the band gap of the material. Since the pH of the solution alters the band positions at the surface [4], it is crucial to maintain the pH that makes the reaction feasible. Also, depending on how the bands are bent by changing the pH, the photochemical reaction can be favored or supressed. Hence, the observed reactivity for any material is a net effect of all the factors mentioned above.

4.2 Research outline.

4.2.1 ***Objective*** *– To determine the compositional dependence of the photochemical reactivity of $Sr_xBa_{1-x}TiO_3$.*

In this research, the reactivities of the materials in ferroelectric and paraelectric states are compared using samples composed of varying compositions of $BaTiO_3$ and $SrTiO_3$. The reason to use these materials is the similarity of their structure and properties and their mutual solubility. As the amount of $SrTiO_3$ increases in $Sr_xBa_{1-x}TiO_3$, the Curie temperature decreases (discussed earlier in **Section 3.3**). At $x \approx 0.26$, T_C is close to 24 °C which is the temperature at which the experiments are conducted (**Fig. 3.3**) [5, 6].

Samples with slightly different compositions will have comparable structures but the sample with slightly more Ba will be in the ferroelectric state and the one with slightly more Sr will be in the non-ferroelectric state. In other words, everything about these samples remains comparable except for the ferroelectric state. Hence there remains approximately one parameter, i.e., the polarization, that will affect the photochemical properties of the sample.

The photochemical reactivity of different compositions of $Sr_xBa_{1-x}TiO_3$ can be compared in several ways. One method is to carry out the photolysis of water and compare the amount of hydrogen synthesized with the passage of time for different samples [7-12]. The samples can be activated by loading them with NiO/Ni co-catalysts using the impregnation method. The R773 – O473 pretreatment (H_2 reduction at 773 K for 2 hrs followed by O_2 oxidation at 473 K for 1 hr after impregnation in an aqueous $Ni(NO_3)_2$ solution) can also be used [8, 13]. The amount of H_2 and O_2 produced can be determined using a gas chromatograph.

The other method is to record and compare the photodegradation of organic dyes in the presence of catalysts. The change in the color of several dyes such as Acid Blue – 9, Acid Orange 7, X – 3B, Orange II, Crystal Violet and Methylene Blue on photodegradation in the presence of a catalyst like TiO_2 and ZnO is reported in the literature [14-25]. The color change of the organic dyes on changing their chemical state by reacting with the photocatalysts is measured to compare the reactivity of different samples [22]. To observe and compare the color change of the dye, diffuse reflectance spectroscopy and absorbance spectroscopy can be used. The later method is used in this research. The structures and characteristics of the dyes are explained in **Section 3.4** and the experiments to demonstrate the mechanism by which they photochemically react with the samples are discussed in **Section 6.3.1**.

If the reactivity of a sample in the ferroelectric state turns out to be more than the reactivity in the paraelectric state, it will support the hypothesis that ferroelectrics are photochemically more reactive than the non-ferroelectrics with a similar composition and structure. The materials chosen for this study are $BaTiO_3$ and $SrTiO_3$. The structure and properties of $BaTiO_3$ and $SrTiO_3$ and their solid solutions are well known. This facilitates the interpretation of the results of this research.

As mentioned earlier in this chapter, there are factors other than ferroelectric polarization that affect the reactivity. It is therefore important in this research to isolate the effects of all the factors including polarization, dielectric constant, band gap, absorption depth, efficiency of non-radiative transitions, and pH of the solution. The analysis of the effect of band gap, absorption depth and efficiency of non-radiative transition of the material can be done based on the information from the literature. The effect of polarization and dielectric constant can be observed by taking AFM images of the surface of different compositions of $Sr_xBa_{1-x}TiO_3$ before and after reaction with $AgNO_3$ solution [26, 27]. All of the samples should be reacted for the same duration and the difference in the mode of reaction and the amount of reaction product left on the surface can then be observed. Also, the dielectric constant affects the Debye length [1]. Samples with different Debye lengths can be made by doping $BaTiO_3$ to change the donor concentration and subsequently the Debye length. The change in reactivity of samples can be evaluated by comparing the rates at which doped and undoped samples photochemically degrade dyes. To study the effect of the pH of the solution, the relative reactivities can be evaluated in solutions of different pH. Also, some control experiments will be carried out to reduce uncertainty and to rule out alternative explanations for the observations. All these experiments are explained in more detail in the **Chapters 5 and 6**.

4.3 References.

1. Albery, W.J. and P.N. Bartlett, J. Electrochem. Soc., 1984. **131**: p. 315.
2. Sze, S.M., *Physics of Semiconductor Devices, 2nd edition*. 2001: John Wiley & Sons Inc.
3. Omar, M.A., *Elementary Solid State Physics : Principles and Applications*. Addison - Wesley Series in Solid State Sciences. 1975, USA: Addison - Wesley Publishing Company, Inc.
4. Morrison, S.R., *Electochemistry at Semiconductor and Oxidized Metal Electrodes*. 1980, New York: Plenum Press.
5. Remmel, T., R. Gregory, and B. Baumert, *Characterization of Barium Strontium Titanate Films Using XRD.* JCPDS-International Centre for Diffraction Data 1999: p. 38-45.
6. Naik, R., et al., Phys. Rev. B, 2000. **61**(17): p. 11367-11372.
7. Inoue, Y., M. Okamura, and K. Sato, 1985. **89**: p. 5184-5187.
8. Domen, K., et al., J. Chem. Soc., Chem. Commun., 1986: p. 356-357.
9. Inoue, Y., et al., J. Chem. Soc. Commun., 1992.
10. Kudo, A., H. Kato, and S. Nakagawa, J. Phys. Chem. B, 1999. **104**: p. 571-575.
11. Kim, H.G., et al., Chem. Commun., 1999: p. 1077-1078.
12. Hwang, D.W., et al., J. of Catalysis, 2000. **193**: p. 40-48.
13. Domen, K., et al., Bull. Chem.. Soc. Jpn., 2000. **73**: p. 1307-1331.
14. Tang, W.Z., et al., Environ. Technol., 1997. **18**: p. 1.
15. Tanaka, K., K. Padermpole, and T. Hisanaga, Wat. Res., 1999. **33**: p. 327.
16. Muneer, M., R. Philip, and S. Das, Res. Chem. Intermed., 1997. **23**: p. 233.
17. Peeves, P., et al., Solar Energy, 1992. **48**: p. 48.
18. Jiang, Z., et al., Chemosphere, 2004. **56**: p. 503-508.
19. Mendez-Paz, D., F. Omil, and J.M. Lema, Water Research, 2005. **39**: p. 771-778.
20. Fernandez, J., et al., App. Catl. B: Environ., , 2004. **48**: p. 205-211.
21. Wu, J.C.-S. and C.-H. Chen, J. of Photochem. And Photobio. A: Chem, 2004. **163**: p. 509-515.
22. Lizama, C., et al., Catalysis. Today, 2002. **76**: p. 235-246.
23. Chen, Y., et al., J. of Photochem. And Photobio. A: Chem., 2005. **172**: p. 47-54.
24. Doushita, K. and T. Kawahara, J. of Sol-Gel Sc. And Tech., 2001. **22**: p. 91-98.
25. Yang, T.C.-K., et al., Proc. of the 2nd Pacific Basin Conf. on Abs. Sc. And Tech., 2000(May): p. 683-687.
26. Giocondi, J.L. and G.S. Rohrer, J. Phys. Chem. B, 2001. **105**: p. 8275-8277.
27. Giocondi, J.L. and G.S. Rohrer, Chem. Mater., 2001. **13**: p. 241-242.

5. Experimental work.

The experimental work is divided in two main sections: "The comparison of photochemical reactivity" and "The understanding of different factors affecting reactivity". The first section includes different techniques used to compare the reactivities of the samples. The comparison of the reactivity of $Sr_xBa_{1-x}TiO_3$ using methylene blue was done in two ways. One was using diffuse reflectance spectroscopy and the second was using absorbance spectroscopy. The reactivity of $Sr_xBa_{1-x}TiO_3$ was also compared by using AFM to measure the amount of Ag left on the surface after it was photochemically reduced from an aqueous $AgNO_3$ solution. To understand how different factors such as dielectric constant, Debye length, polarization and pH affect the reactivity, absorbance spectroscopy and/or AFM imaging was used. The details of the sample preparation and the experimental setups for all these experiments are explained in the following sections.

5.1 Sample preparation.

5.1.1 *Polycrystalline $Sr_xBa_{(1-x)}TiO_3$ for Spectroscopy.*

The samples for the diffuse reflectance and absorbance spectroscopy were prepared in the same manner. Samples used in the study are 1 cm diameter polycrystalline cylindrical pellets of varying compositions of $Sr_xBa_{1-x}TiO_3$ in the range $0 \leq x \leq 1$. It was important to prepare the samples so that they have approximately the same color and the diffuse reflectance spectra are dominated by changes in dye absorption rather than differences in the substrate reflectivity (explained in **Section 5.2.1.1(a)**). The temperatures for the reaction and sintering steps mentioned below are decided by making multiple samples at different temperatures. The phase purity of the samples was evaluated using X-ray diffraction. The sintering processes were selected to produce samples with similar color and enough strength for handling. When the samples are heated in the furnace, alumina crucibles are used with an excess of parent powder so that the pellets do not come in contact with the crucible. The heating rate of the furnace was 10 °C/min when the solid solutions are formed. For all sintering, the heating rate was 10 °C/min until 900 °C and 5 °C/min for any further increase in temperature. At the end of the heat treatment, the furnace was always step cooled. The steps taken for the preparation of the samples are enumerated below.

1. The starting materials are $BaTiO_3$ and $SrTiO_3$ powders of 99.7 % and 99.9 % purity respectively. The powders are obtained from Alfa Aesar and have particle size of less than 5 micron. For mixed compositions, these powders are mixed in stoichiometric ratios.
2. Cylindrical pellets are then made by uniaxially pressing the powders under a nearly 230 MPa load. A few drops of binder (Ethanol 95 % pure, ACS/ USP grade obtained from Pharmco-AAPER) are added to make these green pellets strong enough to avoid breakage while handling. Stearic acid (95 % pure obtained from Research Chemicals Ltd.), mixed in excess of ethanol (95 % pure, ACS/ USP grade obtained from Pharmco-AAPER), was used as a lubricant for the parts of the pressing dye.
3. The polycrystalline samples are prepared according to the schedule specified in **Table 5.1**. The burn-off stage for each sample was intended to remove the

organic binder and lubricant. For $Sr_xBa_{1-x}TiO_3$ compositions with 0<x<1, pellets of mixed $BaTiO_3$ and $SrTiO_3$ powders are reacted in air to create a single phase $Sr_xBa_{1-x}TiO_3$. After this reaction step, the pellets are again ground into fine powder using a mortar and pestle. New pellets are made from this ground powder and then sintered in air as explained in **Table 5.1**.

Table 5.1 – Polycrystalline $Sr_xBa_{(1-x)}TiO_3$ sample preparation for spectroscopy experiments.

Stage / Composition	**$BaTiO_3$**	**$SrTiO_3$**	**$Sr_xBa_{(1-x)}TiO_3$**
Reaction Step	–	–	1250 °C 12 hrs
Hand Grinding	_	_	Yes
Burn Off	900 °C 10 hrs	900 °C 10 hrs	900 °C 10 hrs
Sintering	1250 °C 10 hrs	1300 °C 6 hrs	1250 °C 6 hrs

4. The presence of single phase $Sr_xBa_{(1-x)}TiO_3$ was determined using X-Ray Diffraction. The XRD patterns of $Sr_{0.26}Ba_{0.74}TiO_3$ and $Sr_{0.27}Ba_{0.73}TiO_3$ powders after inadequate annealing at the reaction step are shown in **Fig. 5.1 (a) and (b)** respectively. The reference peak positions of $Sr_xBa_{1-x}TiO_3$ compositions that were the closest match available to the peak positions in the diffraction patterns are superimposed on **Fig. 5.1 (a) & (b)**. $SrTiO_3$ peaks are detected in both these powders indicating the presence of residual $SrTiO_3$. An XRD pattern of single phase $Sr_{0.29}Ba_{0.71}TiO_3$ powder after the appropriate reaction step (1250 °C for 12 hrs) is shown in **Fig. 5.1 (c)**. The reference peak positions of $Sr_{0.4}Ba_{0.6}TiO_3$ are superimposed on this diffraction pattern.

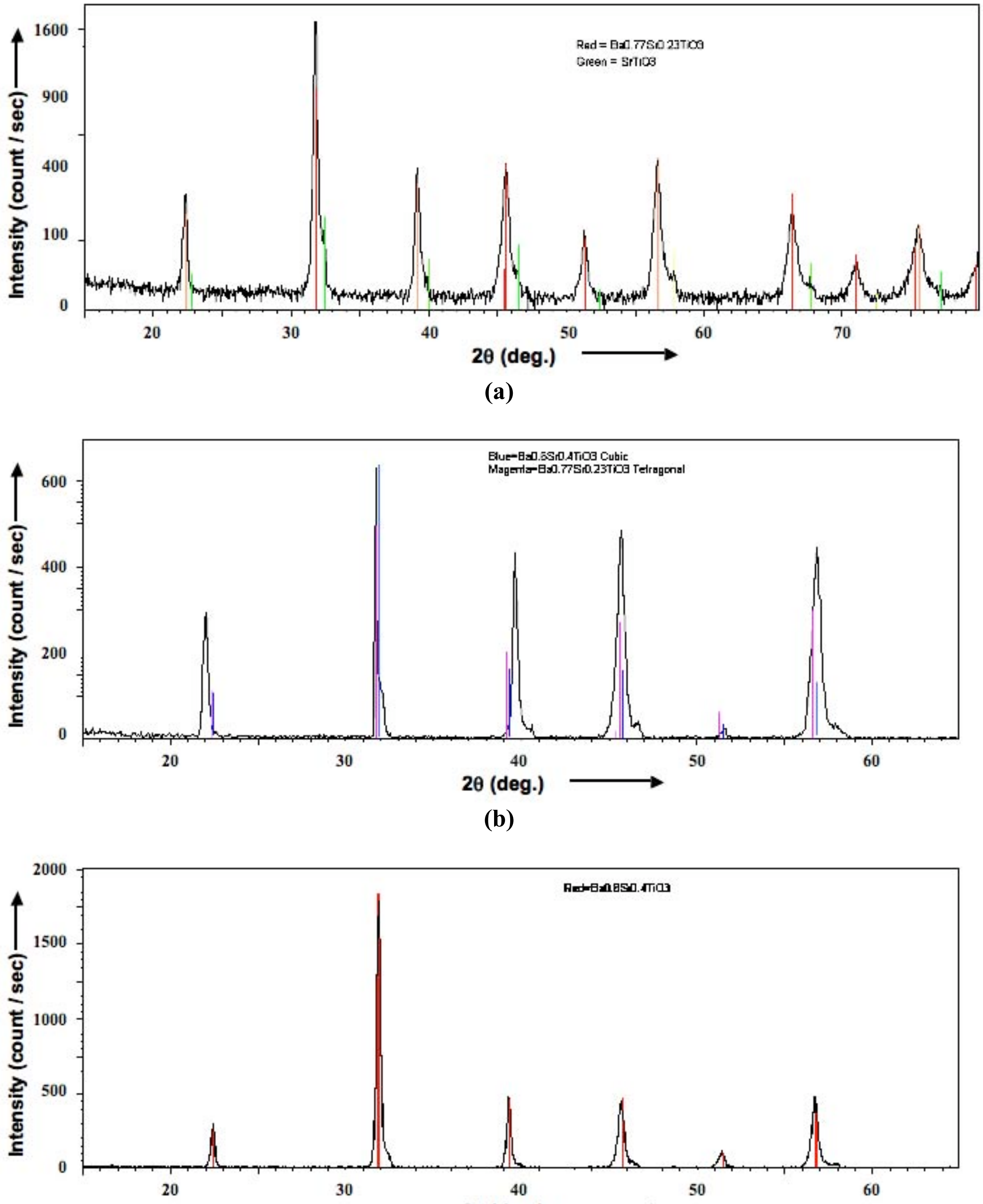

Figure 5.1 – X – ray diffraction pattern (Intensity vs. 2θ) of inadequately reacted **(a)** $Sr_{0.26}Ba_{0.74}TiO_3$ and **(b)** $Sr_{0.27}Ba_{0.73}TiO_3$ powders and adequately reacted single phase **(c)** $Sr_{0.29}Ba_{0.71}TiO_3$ powder.

Figure 5.2 shows the scanning electron microscope (SEM) images of **(a)** $BaTiO_3$, **(b)** $Sr_{0.8}Ba_{0.2}TiO_3$ and **(c)** $SrTiO_3$ samples used for spectroscopy. The samples are extremely porous and have a wide range of particle sizes. Some samples contain a few big particles >15 microns (for example, $SrTiO_3$) and some small particles <300 nm (for example, $Sr_{0.8}Ba_{0.2}TiO_3$). The average particle size is approximately 700 nm – 1000 nm for these samples.

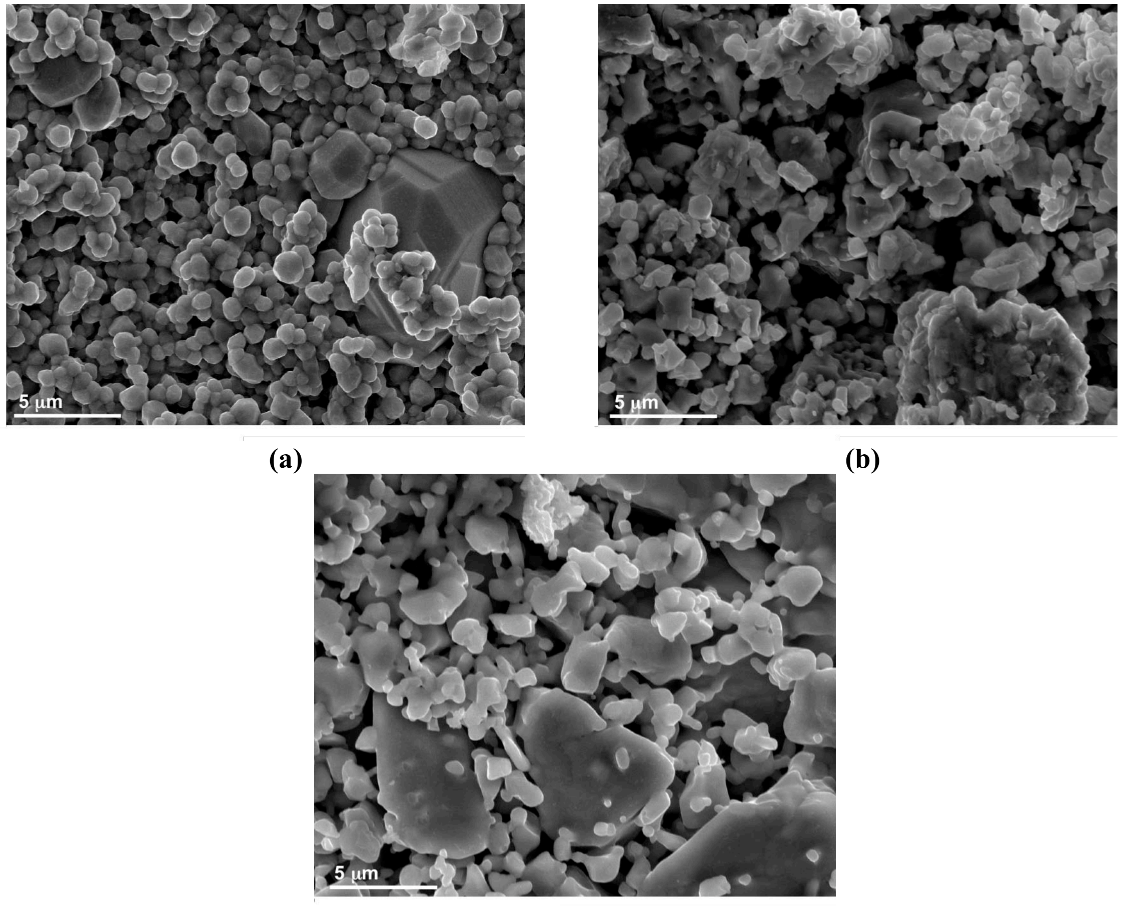

(a) **(b)**

(c)

Figure 5.2 – Scanning electron microscope images of **(a)** $BaTiO_3$, **(b)** $Sr_{0.8}Ba_{0.2}TiO_3$ and **(c)** $SrTiO_3$ samples used for spectroscopy experiments.

5.1.2 *Polycrystalline $Sr_xBa_{(1-x)}TiO_3$ for Atomic Force Microscopy.*

The samples imaged by AFM were prepared to be denser and to have larger grain sizes than the samples used for the spectroscopy experiments. Polycrystalline cylindrical pellets with a 1 cm diameter were prepared with varying compositions of $Sr_xBa_{1-x}TiO_3$ in the range $0 \leq x \leq 1$. The mixed compositions are ground after the reaction step in a mortar and pestle. Hand grinding does not break all the agglomerates formed during reaction step. Therefore, the samples were ball milled for different times. The ball milling time for which the least porous sintered pellets are obtained was used for all the samples. The steps taken for the preparation of the samples are the same as those for the spectroscopy samples with the only difference being the sintering temperatures and the addition of the ball milling step. As before, the heating rate of the furnace was 10 °C/min for the reaction step for mixed compositions. For all sintering, the heating rate was 10 °C/min till 900 °C and 5 °C/min for any further increase in temperature. At the end of the heat treatment, the furnace was always step cooled. The sample preparation is summarized in **Table 5.2**.

For the ball milling step, the powders are mixed with ethanol to make a slurry and are then ball milled in 500 ml plastic bottles using 5 mm yittria stabilized zirconia balls. Zirconia balls are used because they are one of the hardest, toughest and least porous of the available grinding media and hence are less likely to contaminate the samples. After ball milling, the powders are dried by evaporating the ethanol at 85 °C on a hot plate and the new pellets are formed. The sintered pellets are polished using 0.02 μm colloidal silica solution in the final step. The samples are also thermally etched to make surface features such as grain boundaries more visible so that the same area on the surface can be located during sequential steps of the experiment.

Table 5.2 – Polycrystalline $Sr_xBa_{(1-x)}TiO_3$ sample preparation for atomic force microscopy experiments.

Stage / Composition	$BaTiO_3$	$SrTiO_3$	$Sr_xBa_{(1-x)}TiO_3$
Reaction Step	–	–	1250 °C 12 hrs
Hand Grinding	–	–	Yes
Ball Milling	–	–	4 Days
Burn Off	900 °C 10 hrs	900 °C 10 hrs	900 °C 10 hrs
Sintering	1230 °C 10 hrs	1340 °C 10 hrs	1280 °C 10 hrs
Grain Growth	1360 °C 3 hrs	1470 °C 3 hrs	1400 °C 3 hrs
Thermal Etching (After Polishing)	1200 °C 4 hrs	1250 °C 4 hrs	1225 °C 4 hrs

5.1.3 *Polycrystalline Y_2O_3 Doped $BaTiO_3$.*

Y_2O_3 doped $BaTiO_3$ polycrystalline samples were used to study the effect of Debye length on reactivity. Acros Organics 99.999 % pure Y_2O_3 powder was used for doping $BaTiO_3$. Only one doped sample with 0.5 mole % Y_2O_3 in $BaTiO_3$ was made. The powders were mixed in stoichiometric ratios using ball milling. Weighed powders and ethanol were mixed in a 250 ml plastic bottle and ball milled for 2 hrs using 12 mm yittria stabilized zirconia balls. A smaller sized bottle and bigger balls than the ones used for $Sr_xBa_{1-x}TiO_3$ were used because, unlike $Sr_xBa_{1-x}TiO_3$, pulverization of the powder was not required here. After this mixing step, the powder was dried and then pressed in green pellets of 1 cm diameter as described earlier. For the reaction step, the heating rate of the furnace was 10 °C/min. The furnace was step cooled at the end. The reacted pellets crumbled easily and therefore did not require ball milling for as long as $Sr_xBa_{1-x}TiO_3$. This second ball milling was, therefore, also done in a 250 ml plastic bottle using 12 mm yittria stabilized zirconia balls. After drying the reacted powder, it was pressed to make 1 cm pellets again and sintered. The sintering cycle was the same as that for $BaTiO_3$. The preparation is described in **Table 5.3**.

Table 5.3 – Polycrystalline Y_2O_3 Doped $BaTiO_3$ sample preparation for spectroscopy experiments.

Stage / **Composition**	**0.5 mole % Y_2O_3 Doped $BaTiO_3$**
Reaction Step	1000 °C 1.5 hrs
Hand Grinding	Yes
Ball Milling	26 hrs
Burn Off	900 °C 10 hrs
Sintering	1230 °C 10 hrs
Grain Growth	1360 °C 3 hrs

Since different preparation methods are reported in the literature and not all the parameters are mentioned [1-3], some steps in the preparation method are just an imitation of what was used for $Sr_xBa_{1-x}TiO_3$ preparation. It is assumed that since the sample is very lightly doped, it can be processing in the same way as $BaTiO_3$.

Figure 5.3 shows the scanning electron microscope (SEM) image of 0.5 mole % Y_2O_3 doped $BaTiO_3$ sample used for spectroscopy. The samples are also extremely porous and have an average particle size of approximately 900 nm.

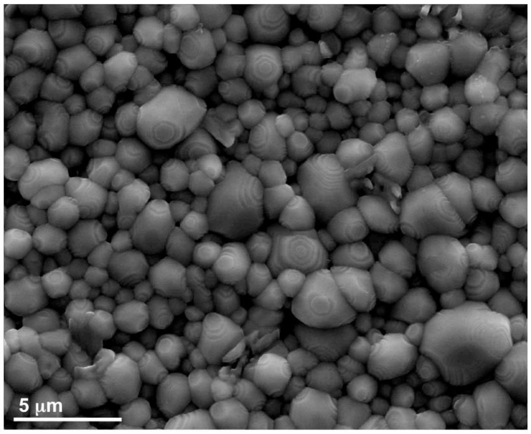

Figure 5.3 – Scanning electron microscope image 0.5 mole % Y_2O_3 doped $BaTiO_3$ sample used for spectroscopy experiments.

5.1.4 *Methylene Blue Dye Solution.*

Methylene blue dye was obtained from Fisher Scientific in powder form. This dye powder was dissolved in deionized water. A concentrated dye solution (4×10^{-5} M) was made in large quantity batches (4 liters per batch). This solution was diluted to the desired concentrations for the experiments.

5.1.5 *Silver Nitrate Aqueous Solution.*

The ACS certified $AgNO_3$ crystals were obtained from Fisher Scientific. These crystals were dissolved in deionized water to form a 0.115 M aqueous $AgNO_3$ solution.

5.2 Experimental Setup.

A 300 W high pressure mercury lamp was used as an illumination source. Before describing the experiments, it is important to see if this UV lamp generates radiation with enough energy to excite the electrons across the band gap for all the samples. The spectrum produced by this lamp (shown in **Fig. 5.4**) is relatively constant between 300 –

800 nm [4]. The intensity sharply decreases below 300 nm with just a single sharp peak at 240 nm before it goes to zero. The photons arising from this region of the 240 nm peak are much fewer in number than from the rest of the spectrum. They are also attenuated more strongly by the intervening air and the liquid in the experiment. Therefore, it is assumed that a majority of photogenerated charge carriers are produced by the photons from the remaining part of the spectrum. In other words, photons with energies lower that 4.1 eV (corresponding to 300 nm wavelength) are utilized in generating the electron-hole pairs. Since $SrTiO_3$ has the largest band gap of all the $Sr_xBa_{1-x}TiO_3$ compositions, it is important to know if the photons with 4.1 eV energies are sufficient to excite electrons from the valence band to the conduction band in $SrTiO_3$. It has been previously reported that 4.1 eV is enough to generate charge carriers in $SrTiO_3$ and a slight increase in the band gap would mean fewer or no photogenerated charge carriers in the sample on illumination [5].

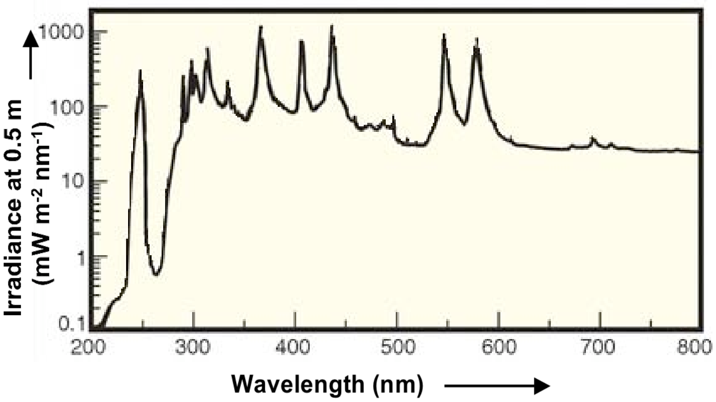

Figure 5.4 – Emission spectrum produced by the 300 W high pressure Hg lamp used in this research.

5.2.1 *Photochemical Reactivity Comparison – Using dyes.*

Each sample is tied with a coated electrical wire and hung inside a 250 ml quartz reactor with a 1-inch diameter quartz window. UV light from a 300 W mercury lamp enters the reactor through this window. The pellet is placed in the reactor in such a manner that one flat face was parallel to the window and as close to it as possible without touching it **(Fig. 5.5).** Dye solution (200 ml of 1×10^{-5} M or 5×10^{-6} M Methylene blue solution) is then poured into the reactor. The concentration of the dye solution is chosen so that the absorbance of the dye solution is less than 1 and in a range where Beer's law is applicable (**Section 5.2.1.1(b) and 6.4.1.1**). The solution was magnetically stirred at 700 rpm throughout the experiment. Before UV exposure, the solution was allowed to stir for 10 minutes to reach adsorption equilibrium. Different times have been reported for different dyes to reach adsorption equilibrium (1 hr to overnight) during photocatalytic degradation studies [6, 7]. However, the samples used in these studies were powders and hence had larger surface area than the polycrystalline samples used in this research. Since the samples used for the spectroscopy study in this research were porous, bubbles could be seen after putting the sample in the dye solution. No bubbles were observed after 10 min of stirring and there was no difference in absorbance of the solution after 10 min and 30 min of stirring. Hence, 10 min of stirring was used. Some recent literature has also reported 15 min of stirring time to reach adsorption equilibrium for photocatalytic degradation of methylene blue [8]. After 10 min of stirring, illumination began.

The duration of illumination for diffuse reflectance spectroscopy experiments was 40 minutes. The sample was then removed from the reactor and the surface was analyzed. For the absorbance experiments, the total duration of the illumination was 200 min and 5 ml dye solution samples were withdrawn from the reactor for analysis every 40 min. These processes were repeated for different compositions of $Sr_xBa_{1-x}TiO_3$. The duration of the experiment was 200 min because the UV lamp becomes extremely hot by this time, despite constant water cooling. The sampling time of 40 min was decided to avoid excessive change in the total volume of dye solution in the reactor during the course of the experiment.

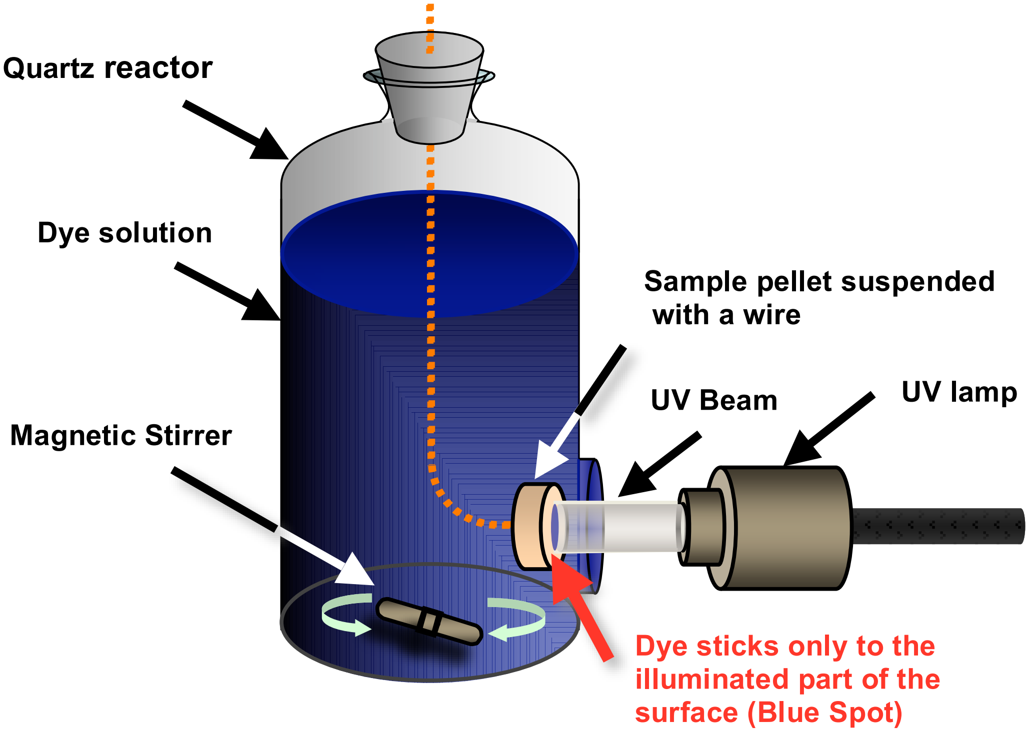

Figure 5.5 – A schematic of quartz reactor used for this study. The sample pellet is placed in front of the lamp with the aid of a wire.

The set of experiments to study the effect of pH on photochemical reactivity were conducted in the same manner as above with a 5×10^{-6} M methylene blue solution. The pH was reduced using H_2SO_4 and was increased using NaOH.

5.2.1.1 Data acquitsition.

The color change of the dyes can be analyzed by absorbance or diffuse reflectance spectroscopy. One method involves recording “Absorbance” (defined as logarithm of the ratio of incident light intensity to transmitted light intensity at a given wavelength) of dye solution samples withdrawn from the reactor at fixed intervals of time during the illumination [6, 9-19]. Alternatively, the “diffuse reflectance” of the illuminated surface of the sample can be measured to analyze the amount of dye on the surface after illumination [20]. Both the methods are used in this research.

5.2.1.1(a) *Diffuse reflectance spectroscopy.*

To measure the differences in the reactivities of different samples by the change in the color of the dye on their surfaces, the method of “*diffuse reflectance*” is used. The term “reflectance” is defined as the ratio of the amount of radiation reflected from a surface to the amount originally striking the surface. In the case where the particle size is greater than the wavelength of the radiation, the phenomena of reflection, reflectance and diffraction for the individual particles are well defined. Considering only reflection, there can be two types of reflections from the surface. The first is “specular/regular reflection” or “mirror reflection” wherein the angle of incidence is equal to the angle of reflection and light reflects as if from a mirror. The second is “diffuse reflection” wherein light reflects at all possible angles into the hemisphere from which the incident radiation originates as if reflecting from a matte surface. Ideal diffuse reflectance is defined by the condition that the angular distribution of the reflected radiation is independent of the angle of incidence [21].

The law of diffuse reflectance by Seeliger [22] assumes that the radiation penetrates the sample, undergoes numerous reflections, refractions and diffractions and gets partly absorbed and partly returned through the surface. The emitted radiation is the sum of all the contributions of all the elements of the penetrated volume.

To obtain diffuse reflectance spectra, an Ocean Optics USB 2000 UV-VIS spectrometer (Model AIS MINI DT B) was used with the diffuse reflectance attachment. The schematic in **Fig. 5.6** shows the basic setup of the instrument. The diffuse reflectance probe is connected to the light source and the spectrometer that detects the signal from the reflected light by a set of optical fibers. The spectrometer is connected to a computer that processes the data and displays it in the form of plots of Reflectance vs. Wavelength. The reflection data is calculated by the SpectraSuite software by using **Eqn. 5.1** [23].

$$\%T_\lambda = \frac{S_\lambda - D_\lambda}{R_\lambda - D_\lambda} \times 100\% \qquad \text{---(5.1)}$$

where T_λ = reflection at wavelength λ.

S_λ = sample intensity a wavelength λ.

D_λ = dark intensity at wavelength λ.

R_λ = reference intensity at wavelength λ.

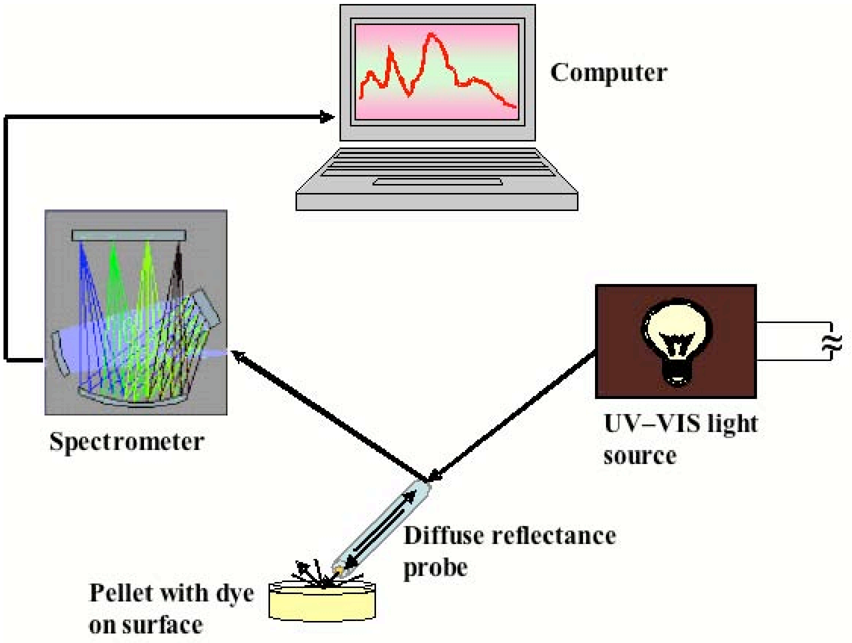

Figure 5.6 – Schematic of the set-up of Spectrophotometer with Diffuse reflectance attachment.

The probe sits on top of the sample pellet at a distance of approximately 2 mm and at an angle of 45° and performs the dual function of light supplier as well as the reflected light collector. The specific angle of 45° is preset by the manufacturer to get the maximum diffuse reflection signal by avoiding the specular or directly reflected light from the window and the sample.

The experiments in this study were conducted using 1×10^{-5} M aqueous methylene blue solution. A reference spectrum to get R_λ values was stored by recording the reflectance from a WS – 1 diffuse reflectance standard by Ocean Optics (> 98 % reflective form 250 – 1500 nm radiation range). A dark spectrum to get D_λ values was stored by recording the reflectance from the standard surface when the UV and visible lamps of the spectrometer were turned off. Both the reference and dark spectra were saved and reloaded into the software for each sample of an experimental set. Twelve compositions of $Sr_xBa_{1-x}TiO_3$ with different x values were used. Diffuse reflectance measurements were carried out on the illuminated surfaces (with dye on them) of each of the samples after 40 min of illumination in the dye solution. The reflectance at 656.8 nm was measured for each sample. This wavelength is chosen because around 656 nm there is the least amount of spectral error as methylene blue dye absorbs this region of the spectrum most strongly and the energy of this radiation is a signature of the methylene blue dye molecule. There is a peak in the Absorbance vs. Wavelength plot around this wavelength. However in Reflectance vs. Wavelength there is a broad trough around this wavelength. It is possible to convert reflectance to absorbance using Kubelka-Munk theory [21, 24], but this was not necessary for the present study.

5.2.1.1(b) *Absorbance Spectroscopy.*

The dye solution samples that were withdrawn from the reactor at 40 min time intervals during the duration of the experiment were immediately transferred to the 5 ml polystyrene cuvettes with 1 cm path length. Path length is the distance the light travels through the solution. Since these cuvettes have a square cross section with a 1 cm length, light travels 1 cm in the solution. The cuvettes were then placed in the absorbance attachment of the UV-VIS spectrometer (shown in **Fig. 5.7 & 5.8**) and the *"absorbance"* spectra were recorded. The term "absorbance" (A) is defined as the logarithm of the ratio of the intensity of the incident radiation (I_0) to the intensity of the transmitted radiation (I). Bouguer [25] was the first person to observe this in 1729 (Lambert [26] came to the same conclusion independently a little later). According to Bouguer's law, when monochromatic radiation passes through an absorbing medium, the amount of energy or intensity absorbed will depend on the frequency of the radiation, the nature of the absorber, and the thickness of the absorber. In 1852, Beer [27] demonstrated that for a given thickness of the sample or absorbing medium, transmittance ($T = I / I_0$) depends exponentially on the concentration of the absorbing species. Combining both of these facts, the expression for absorbance at any wavelength can be expressed by **Eqn. 5.2** [27] **(Fig. 5.7)**.

$$A = \log I_0/I = \log 1/T = \alpha \ell c \qquad \text{--- (5.2)}$$

where A = Absorbance.

I_0 = Incident intensity.

I = Transmitted intensity.

T = Transmittance.

α = Absorptivity or Absorption coefficient (l moles^{-1} cm^{-1}).

ℓ = Path length = 1 cm.

c = Concentration of the sample (moles l^{-1}).

Absorption coefficient, α, is a constant characteristic of the sample and the vacuum wavelength of the radiation. It is defined by **Eqn. 5.3**.

$$\alpha = \frac{4\pi k}{\lambda} \qquad \text{---(5.3)}$$

where k = Extinction coefficient of the sample (l mole^{-1}).

λ = Wavelength of radiation in vacuum (cm).

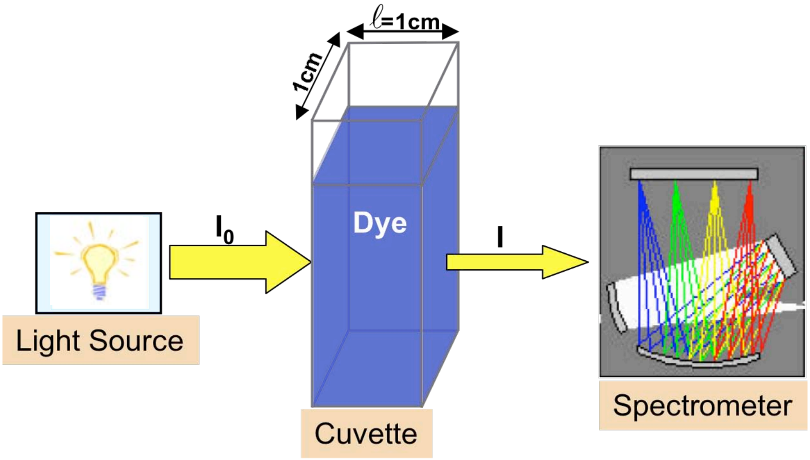

Figure 5.7 – Schematic to explain the parameters of Beer's law.

The absorbance spectrum is a signature of the structure of the absorbing compound. The peak in the absorbance vs. wavelength plot represents the absorption of the quanta of energy that excites an electron from the highest occupied molecular orbital (HOMO) to the lowest unoccupied molecular orbital (LUMO) in the absorbing molecule. The value of absorbance at this wavelength is of prime significance.

There are several factors that can lead to deviations from Beer's law. The reflection from the surface of the cuvettes, contaminants on the surface and the sample, convergence or divergence of the beam from the light source, non-homogeneity of the incident radiation or of the sample, scattering, fluorescence or activation of absorbing molecules by absorption can all lead to a deviation from linear dependence of absorbance on concentration. When the concentration of the solution is varied, some other effects due to chemical and physical interaction of absorbing molecules become important. There is a possibility of hydrogen bonding, ion-pair formation, solvation or some other chemical reactions taking place that can affect the concentration of the absorbing species. Physical interactions between polar molecules can lead to a change in the refractive index and consequently in the dielectric constant of the solution resulting in a change in absorption coefficient. These effects become more significant at higher concentrations and as a result the plot of absorbance vs. concentration deviates from straight line behavior and the slope of the curve decreases. It is therefore important in experimental analysis to conduct the study with solutions dilute enough for Beer's law to hold true [26]. The experiment conducted to ensure this is described in **Section 6.4.1.1**.

The set up of UV-VIS spectrometer for absorbance measurements is shown in **Fig. 5.8**. It is similar to the set up for diffuse reflectance measurements except that the cuvette holder unit replaces the diffuse reflectance probe. The absorbance data at any wavelength λ is calculated by the SpectraSuite software by using **Eqn. 5.4** [4].

$$A_\lambda = \log_{10}\left(\frac{R_\lambda - D_\lambda}{S_\lambda - D_\lambda}\right) \qquad \text{---(5.4)}$$

The software uses this equation to evaluate each pixel on the detector and produce the absorbance spectrum.

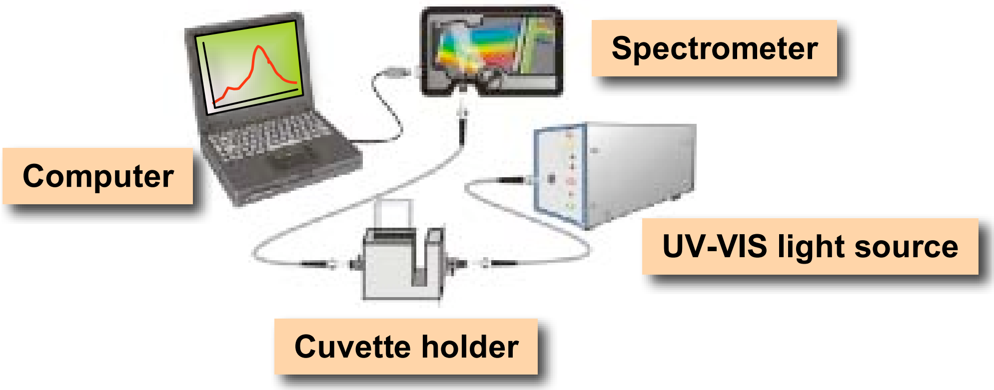

Figure 5.8 – Schematic of the set-up of Spectrophotometer with cuvette holder attachment for absorbance measurement.

The reference spectrum to get R_λ values was stored by recording the absorbance of deionized water because it was the solvent or the reference. A dark spectrum to get D_λ values was stored by recording the absorbance of the standard when either the path of the light was blocked or the visible light lamps of the spectrometer were turned off. Both the reference and dark spectra were saved and reloaded into the software for each measurement of an experimental set. The samples used for these experiments were the same as those used for diffuse reflectance experiments. For each $Sr_xBa_{1-x}TiO_3$ sample, the change in the color of the dye solution is observed for a period of 200 min by recording the absorbance spectra of the dye solution samples (5 ml each) withdrawn at fixed intervals.

To access the instrumental error, ten spectra were recorded for a single methylene blue dye solution. When the absorbance is taken at the peak of main absorption band, the measurement has a standard deviation of approximately 0.2 %. If a portion of the spectrum is integrated in vicinity of the peak (in the wavelength range of 650.19 to 675.19 nm), the standard deviation is reduced to 0.1 %. In all of the measurements reported here, that latter method was used. Further, because the instrumental uncertainty is relatively small compared to other possible sources of error, it will not be mentioned further.

5.2.2 *Atomic Force Microscopy.*

In this research, AFM was used for two separate sets of experiments. First, it was used to understand the mechanism of the interaction between methylene blue and the sample. Second, it was used to compare the photochemical reactivity of different compositions of $Sr_xBa_{1-x}TiO_3$ by determining the amount of Ag that each composition is able to reduce from aqueous $AgNO_3$ solutions under equivalent conditions. The same data set was also used to separately understand the effects of ferroelectric polarization and dielectric constant. Both of these experimental setups are explained below.

5.2.2.1 Dye – Sample Interaction Mechanism Experiment.

A sintered and thermally etched $BaTiO_3$ pellet was suspended in 1×10^{-5} M methylene blue solution and its surface was illuminated by UV light for 100 min in the same set up shown in **Fig. 5.5**. After the lamp was turned off, the pellet was removed, washed with water, air dried and then imaged by AFM. This duration of the experiment was selected by doing the experiment multiple times and imaging the surface after reaction using AFM. The sole motive for choosing the 100 min illumination time was to get good AFM images. Images were first taken with the reaction product, i.e. dye, on the surface. The dye was then cleansed off by swiping the surface with a Q-tip soaked with acetone and then leaving the sample immersed in acetone in a beaker overnight. The sample was further cleaned in ultrasonic cleaner for 20-30 min if required. The surface potential images and the images of the surface without the reaction product were then simultaneously recorded at the same spot where the images with the reaction product were recorded. It has been shown previously that in the surface potential images collected from the ferroelectric materials, the measured charge is actually related to the screening charges rather than to the charge of the domain dipole itself [28, 29]. In ferroelectric materials, charge screening on the surface can be provided by adsorbates, surface states and free charges. As a result, the measured charge is actually the opposite of the charge created by ferroelectric polarization, i.e. light areas in the image correspond to the regions where the negative end of the domain dipoles are oriented towards the surface. The information about the orientation of the domain polarization vector that is obtained from the surface potential images can be used to predict which reaction (reduction or oxidation) will be preferred at a specific location. Hence, reaction behavior could be determined through AFM imaging. In other words, if, after the reaction, the dye is found on only one type of domain, the nature of the reaction (reduction or oxidation) can be determined by comparing the dye locations to the surface potential image.

5.2.2.2 Photochemical Reactivity Study using AFM.

Sintered and thermally etched $Sr_xBa_{1-x}TiO_3$ samples of different compositions were first imaged using the AFM. These samples were then photochemically reacted with a 0.115 M aqueous $AgNO_3$ solution. The photochemical reaction used for this set of experiments is expressed in **Eqn. 5.5**.

$$Ag^+ + e^- = Ag \qquad \text{---(5.5)}$$

This reaction leaves insoluble Ag on the surface at the reaction site. Ag^+ ions are provided by a 0.115 M aqueous $AgNO_3$ solution. The experimental setup is depicted in

Fig. 5.9. An O-ring was placed on top of the sample surface and filled with aqueous $AgNO_3$ solution. The surface was illuminated by a 300 W Hg lamp placed directly on top of the O-ring. After reaction, the O-ring was removed and the sample was washed with water and air-dried. The samples were then imaged at the same locations as before reaction by using the AFM [30]. The reaction time for all the $Sr_xBa_{1-x}TiO_3$ samples was 6 seconds. The amount of silver on each sample was then taken as a measure of the photochemical reactivity. The method used to determine the amount of silver will be described in **Section 6.4.3**.

The Ag reaction location gives information about the factors influencing the reactivity. For example, if Ag is not selectively reduced on some regions of a grain in domain patterns (as in the case of $BaTiO_3$), it will confirm that there is no spatially selective reactivity due to ferroelectric polarization.

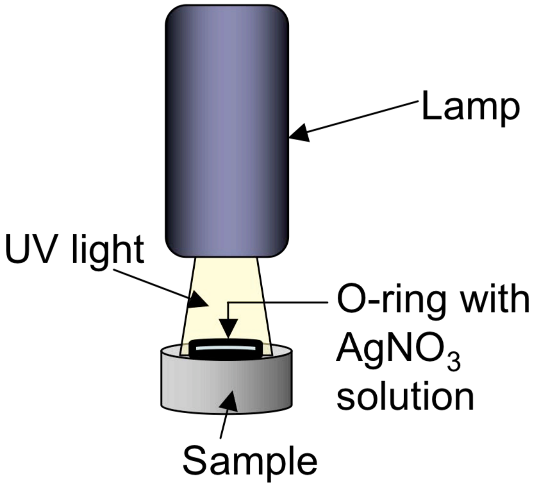

Figure 5.9 – Schematic of the set-up for probe reactions.

5.3 References.

1. Jeong, J.H., M.G. Park, and Y.H. Han, J. of Electroceram., 2004. **13**: p. 805-809.
2. Kim, J.H. and Y.H. Han, Mat. Sc. For., 2007: p. 534-536.
3. Liu, X., Y. Luo, and X. Li, J. of Al. and Comp., 2008. **459**: p. 45-50.
4. http://www.newport.com/images/webclickthru-EN%5Cimages/1013.gif.

5. Giocondi, J.L., P.A. Salvador, and G.S. Rohrer, Topics in Catalysis, 2006. **41**: p. 1-2.
6. Chen, Y., et al., J. of Photochem. And Photobio. A: Chem., 2005. **172**: p. 47-54.
7. Chuang, T.-H. and S.-F. Wang, Proc. of the 2nd Pacific Basin Conf. on Abs. Sc. And Tech. (Brisbane, Australia), 2000(May): p. 683-687.
8. Franco, A., et al., J. of Haz. Mats., 2009. **161**: p. 545-555.
9. Tang, W.Z., et al., Environ. Technol., 1997. **18**: p. 1.
10. Tanaka, K., K. Padermpole, and T. Hisanaga, Wat. Res., 1999. **33**: p. 327.
11. Muneer, M., R. Philip, and S. Das, Res. Chem. Intermed., 1997. **23**: p. 233.
12. Peeves, P., et al., Solar Energy, 1992. **48**: p. 48.
13. Jiang, Z., et al., Chemosphere, 2004. **56**: p. 503-508.
14. Mendez-Paz, D., F. Omil, and J.M. Lema, Water Research, 2005. **39**: p. 771-778.
15. Fernandez, J., et al., App. Catl. B: Environ., , 2004. **48**: p. 205-211.
16. Wu, J.C.-S. and C.-H. Chen, J. of Photochem. And Photobio. A: Chem, 2004. **163**: p. 509-515.
17. Lizama, C., et al., Catalysis. Today, 2002. **76**: p. 235-246.
18. Doushita, K. and T. Kawahara, J. of Sol-Gel Sc. And Tech., 2001. **22**: p. 91-98.
19. Wuw, J.-M. and B. Huang, J. Am. Ceram. Soc., 2006. **89**(8): p. 2660 – 2663.
20. Yang, T.C.-K., et al., Proc. of the 2nd Pacific Basin Conf. on Abs. Sc. And Tech., 2000(May): p. 683-687.
21. Kortüm, G., *Reflectance Spectroscopy – Principles, Methods and Applications*. 1969: Springer-Verlag New York Inc.
22. Seeliger, V., R : Münch. Akad. II. K1. Sitzungsber., 1888. **18**: p. 201.
23. software, I.m.S.
24. Blevin, W.R. and W.J. Brown, J. Opt. Soc. Am., 1961. **51**: p. 129.
25. Bouguer, P., Essai d' optique sur la gradation de la lumière, 1729.
26. Bauman, R.P., *Absorption Spectroscopy*. 1962: John Wiley & Sons, Inc.
27. Beer, A., Ann. Physik. Chem., 1852. **2**(86): p. 78.
28. Kalinin, S., R. Shao, and D.A. Bonnell, J. Am. Ceram. Soc., 2005. **88**: p. 1077-1098.
29. Kalinin, S. and D.A. Bonnell, Physical Review B, 2001. **63**: p. 125411.
30. Giocondi, J.L., in *MSE*. 2003, Carnegie Mellon University: Pittsburgh.

6. Results - Comparison of photochemical reactivities.

6.1 Introduction.

The experiments using methylene blue are designed in such a way that UV light from the 300 W Hg lamp excites charge carriers in the $Sr_xBa_{1-x}TiO_3$ samples that are immersed in the magnetically stirred dye solution. Photogenerated electrons and holes react with dye molecules on the surface of the sample and change the oxidation state of the dye. Changing the oxidation state of the dye changes its color and this change in color was used as a measure of photochemical reactivity. The experimental set up is shown in **Fig. 5.5**.

In the silver reduction experiment, the sample must be illuminated with UV light and in contact with an aqueous $AgNO_3$ solution. The amount of insoluble reaction product (Ag) that is left on the surface is taken as a measure of photochemical reactivity. The experimental set up for these probe reactions is shown in **Fig. 5.9**.

6.2 Qualitative observations.

During the course of the dye experiments, 5 ml of dye solution is withdrawn from the reactor at fixed intervals and the absorbance of the solution is measured in the spectrometer. This is done to observe any change in the color of the dye solution due to the UV illumination of the sample. It is observed that the dye solution continuously loses color and becomes lighter. It is also observed that during the experiment, dye is adsorbed only on the portion of the surface that is illuminated. In other words, after the experiment, there is a circular blue mark where the light impinged on the surface. This patch of dye on the surface becomes visibly darker with increased illumination times.

To confirm that it is actually the $Sr_xBa_{1-x}TiO_3$ sample that is responsible for the changes in the dye solution, several control experiments were performed. For example, in one control experiment an alumina (Al_2O_3) pellet was put in place of the sample and all other aspects of the experiment were the same. Since alumina has a band gap of 9 eV [1], it is not expected to generate charge carriers on illumination and hence a reaction is not expected. It is indeed observed that no dye accumulates on the Al_2O_3 pellet. The periodic absorbance measurement of the dye solution also shows that the change in absorbance of the solution after 200 min UV illumination time is 20 % of the change in absorbance when $BaTiO_3$ is used. Therefore, while UV light degrades the dye by a small amount in the control experiment, the majority of the degradation in the normal experiment can be attributed to the $Sr_xBa_{1-x}TiO_3$ samples.

6.3 Mechanism of dye – sample interaction.

To understand how the methylene blue interacts with the samples, a polycrystalline $BaTiO_3$ pellet is used to react with the dye solution in a set up shown in **Fig. 5.5**. The surface of $BaTiO_3$ is imaged using the AFM at the same location before and after reaction.

6.3.1 *Results from AFM for Methylene Blue Reaction.*

Figure 6.1 (a) and (c) are the topographical images of polycrystalline $BaTiO_3$ before and after the reaction with the dye respectively. The contrast in the image represents varying heights. Black in the image corresponds to lower features and white corresponds to higher features. In **Fig. 6.1 (a)** some of the contrast is from the surface microstructure. For example, there are faceted ridges aligned diagonally across the surface. Also, if the sample is cooled from annealing temperatures higher than its Curie temperature (120 °C for $BaTiO_3$), height contrast may appear due to the tetragonal distortion of the unit cells. The domains with polarization vector normal to the surface may either rise or subside as compared to the domains whose polarization vector is parallel to the surface. It is important to note that if the sample is heated above the Curie temperature after polishing, domain contrast from differential polishing may remain on the surface, but will not be expected to correlate with the actual domain structure since a new domain structure will form on cooling from T_C. In **Fig. 6.1 (c)** the contrast is due to the dye deposits on the surface and since the height contrast is much higher in this image than in the image before the reaction, most of the contrast of **Fig. 6.1 (a)** is overshadowed. **Fig. 6.1 (b)** shows the surface potential image of the same area and it is taken simultaneously with **Fig. 6.1 (a)**. In the surface potential image, contrast results primarily from the differences in surface charges. The light to dark contrast represents positive and negative voltages, respectively.

It has been shown previously that in surface potential images collected from the ferroelectric materials, the measured charge is actually related to the screening charges rather than to the charge of the domain dipole itself [2, 3]. In ferroelectric materials, charge screening on the surface can be provided by adsorbates, surface states and free charges. As a result, the measured charge is actually the opposite of the charge created by ferroelectric polarization, i.e. light areas in the image correspond to the regions where the negative end of the domain dipoles are oriented towards the surface. The information about the orientation of the domain polarization vector that is obtained from the surface potential images can be used to predict which reaction (reduction or oxidation) will be preferred at a specific spatial location. Hence reaction behavior could be determined through surface potential imaging.

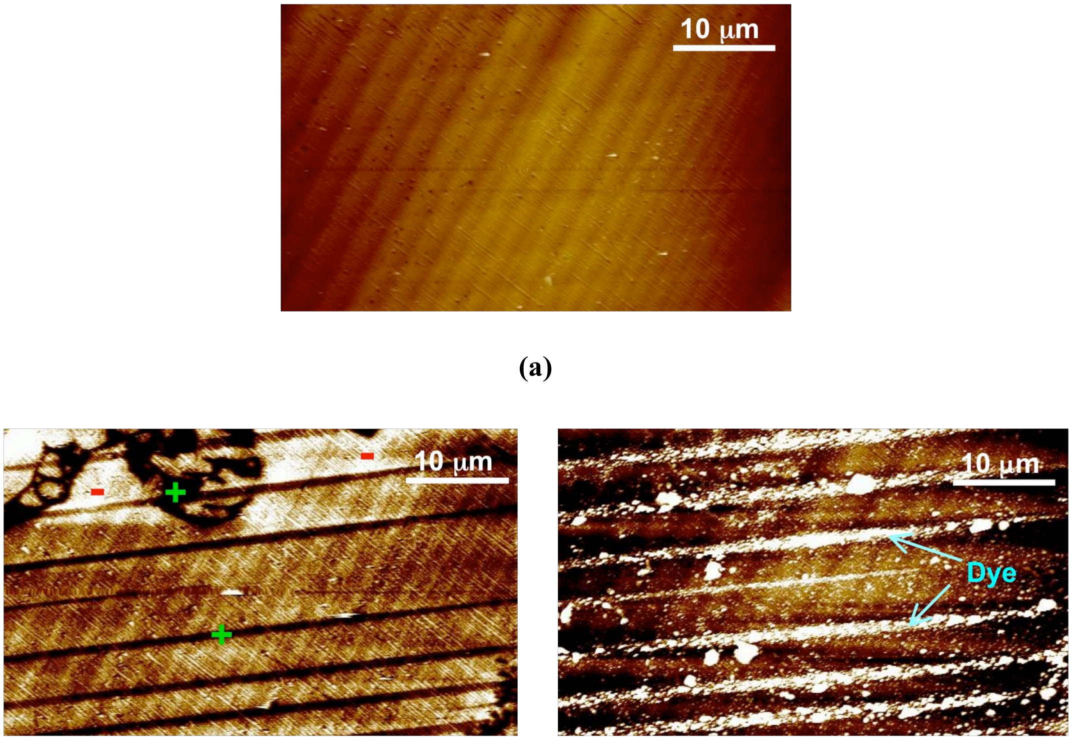

(a)

(b) **(c)**

Figure 6.1 (a) - A topographical AFM image of the surface of $BaTiO_3$ before reaction is pictured. Black-to-white contrast is 200 nm. The contrast in this image could be from facets and/or domains. **(b)** A surface potential image of the same exact location is shown. The domain structure can be observed in this image. The black-to-white contrast is 50 mV. **(c)** The topographical AFM image of the surface of $BaTiO_3$ after reaction with the dye is pictured. Black-to-white contrast is 100 nm.

Comparing **Fig. 6.1 (b) and (c)**, it can be seen that the dye sticks on the regions that are black in the surface potential image. In other words, dye sticks on the domains that have the positive end of the dipole oriented towards the surface. Hence it is seen that the methylene blue dye gets reduced (reaction shown in **Fig. 3.4** [4]) on the positively charged domains and the reduced form of the dye that is blue in color sticks to the surface. The opposite reaction must therefore occur on the negatively charged domains and the blue ions of the dye in the solution give electrons to the $Sr_xBa_{1-x}TiO_3$ sample and get oxidized and become colorless. With the passage of time, more and more blue dye ions stick to the positively charged domains and the surface appears increasingly blue while simultaneously more and more blue ions become colorless in the solution and the solution gradually becomes decreasingly blue (**Fig. 6.2**).

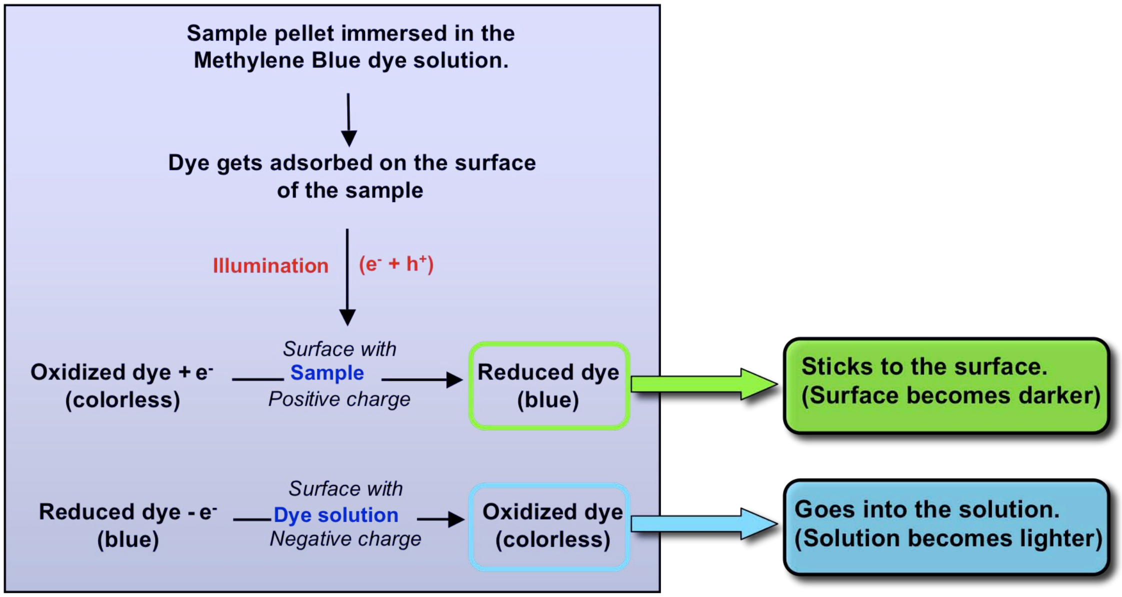

Figure 6.2 – Mechanism of methylene blue dye and $Sr_xBa_{1-x}TiO_3$ sample interaction.

It is important to review here that the dye is observed on the illuminated surface of the $Sr_xBa_{1-x}TiO_3$ samples, but not on the surface of alumina under similar conditions. Because alumina has a band gap of 9 eV [1], photogenerated charge carriers will not be produced. In other words, alumina is not expected to react with the dye and the absence of dye on the surface supports that. It is hence assumed that the dye reacts with the charge carriers on the illuminated $Sr_xBa_{1-x}TiO_3$ surface and sticks to it.

6.4 Experimental results from spectroscopy.

The experiments to compare the photochemical reactivities of different compositions of $Sr_xBa_{1-x}TiO_3$ are carried out in a quartz reactor as illustrated in **Fig. 5.5**. For the diffuse reflectance and absorbance spectroscopy experiments, the dye concentration and UV illumination times were kept constant. The details of the experimental set up and equipment were explained in previous chapters. The results and the methods used to analyze the spectroscopy data are explained below.

6.4.1 *Absorbance Spectroscopy*.

6.4.1.1. Beer's Law Application in Experiments.

Before starting the absorbance experiments it was essential to make sure that at the concentration of the dye used, Beer's law is obeyed (see **Section 5.2.1.1(b)**). This was confirmed by preparing dye solutions of different concentrations and measuring the absorbance at 660.09 nm. This dependence of absorbance on concentration is shown in **Fig. 6.3**. As seen in **Fig. 6.3**, the absorbance is directly proportional to the concentration of methylene blue. Therefore, Beer's law is obeyed between the concentrations of 5×10^{-6} M and 1×10^{-5} M, which are used in this study.

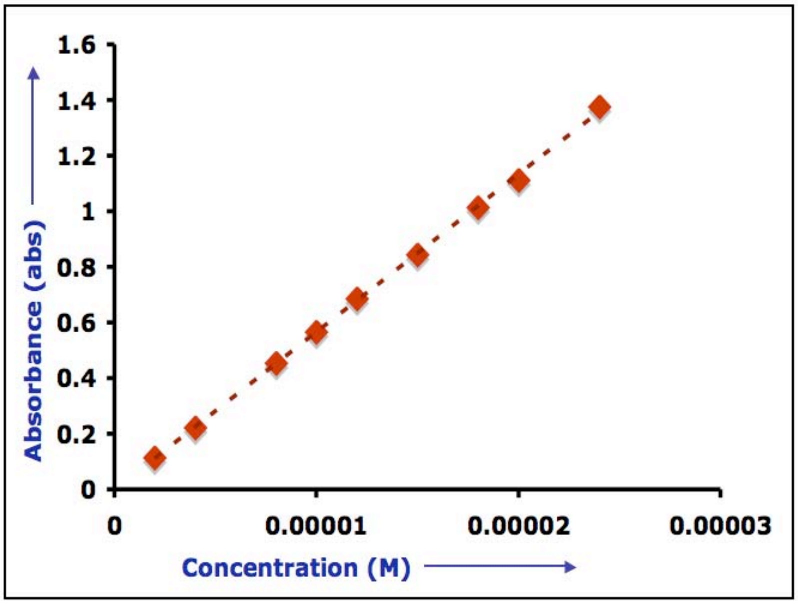

Figure 6.3 – Absorbance vs. Concentration plot for Methylene blue dye. The uncertainty in data points is ± 0.0007 Absorbance units which is less than the size of the points on this plot.

6.4.1.2. Representation of Photochemical Reactivity Comparison in Absorbance Spectroscopy Results.

The photochemical reactivities of the $Sr_xBa_{1-x}TiO_3$ samples are compared by measuring the change in absorbance of the dye solution by reacting with these samples over a fixed period of UV illumination. All of the experiments are conducted at room temperature. For each $Sr_xBa_{1-x}TiO_3$ sample, 5 ml of the dye solution is withdrawn every 40 min during the 200 min duration of the experiment.

Optical absorbance spectra are measured using the spectrometer six times in each experiment. The spectrum labeled “0 minutes” is recorded from a solution removed immediately after the 10 min equilibration period. When the absorbance at 40 min time intervals for a single sample are compared, it is clear that the absorbance at the peak gradually decreases with increased illumination times. An example of these spectra for the $Sr_xBa_{1-x}TiO_3$ sample with x = 0.27 is shown in **Fig. 6.4 (a)**. This spread of absorbance

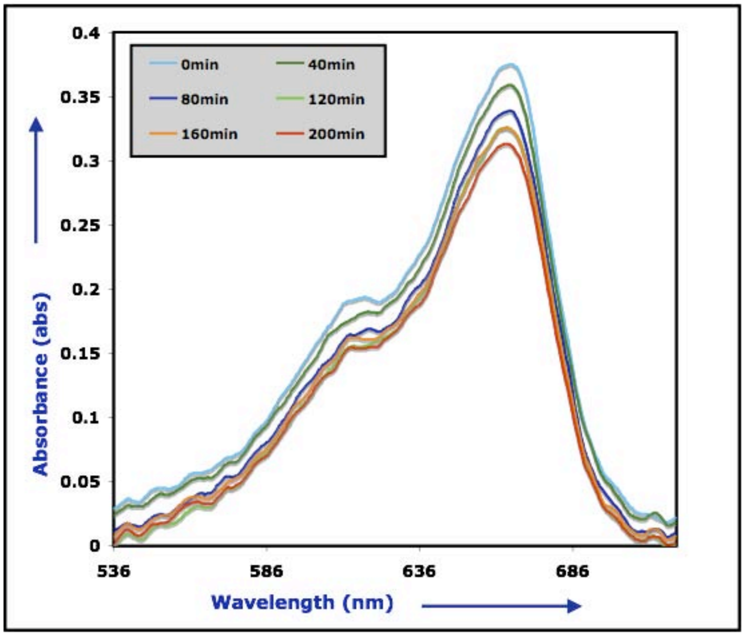

(a)

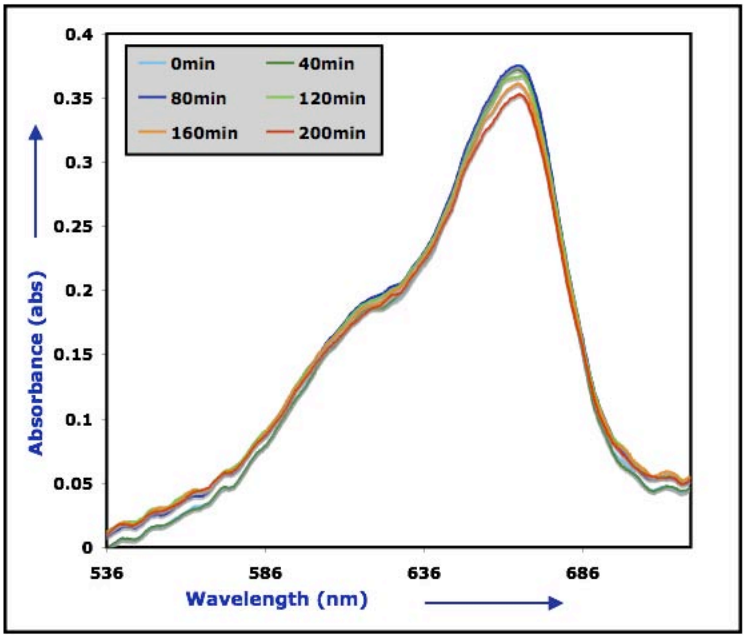

(b)

Figure 6.4 – Change in the absorbance of methylene blue dye with increased UV illumination time in the presence of **(a)** a reactive $Sr_xBa_{(1-x)}TiO_3$ sample (x = 0.27) and **(b)** alumina.

at the peak is different for each sample. It is broader for more reactive samples and narrower for less reactive samples. The comparable spectra for alumina (a control that doesn't react) are shown in **Fig. 6.4 (b)**. There is a narrow spread of absorbance even for alumina that could be from the decay of the dye by itself due to exposure to UV radiation.

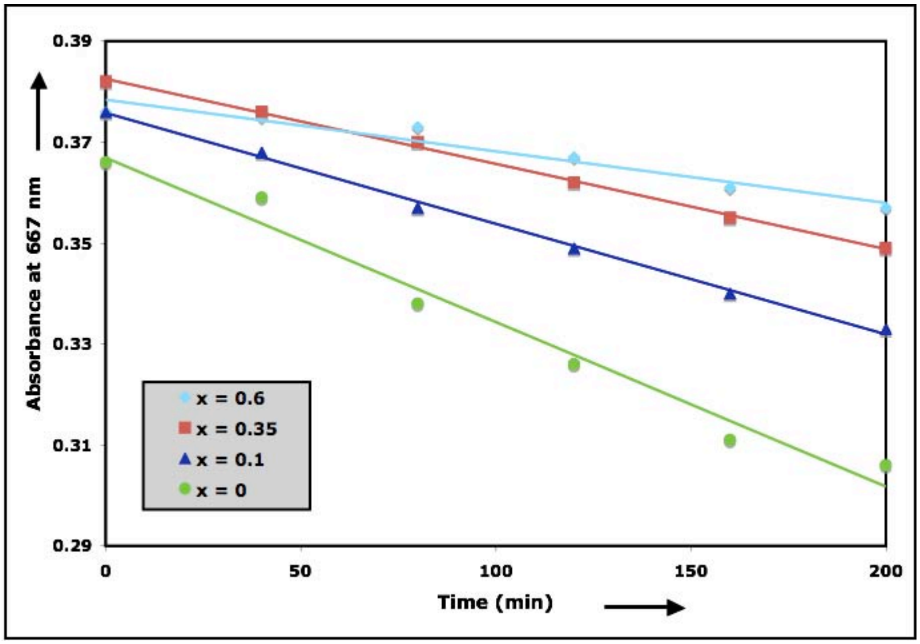

Figure 6.5 – Decay plots for methylene blue dye photodegradation using different $Sr_xBa_{(1-x)}TiO_3$ samples. The uncertainty at each points is ± 0.0007 Absorbance units which is less than the size of the points on this plot.

The data can be compared in several ways. The decay plots for each composition can be made by plotting absorbance at the peak vs. time. An example of such plots is shown in **Fig. 6.5**. The slopes of these decay plots can then be compared for all of the compositions. Alternately, the area under the absorbance spectrum each sample can be calculated for different illumination times. This area is calculated for a small portion of the spectrum close to the peak as shown in **Fig. 6.6**. The reason for using the area under the peak is to accommodate the fluctuation/noise in the absorbance value at each

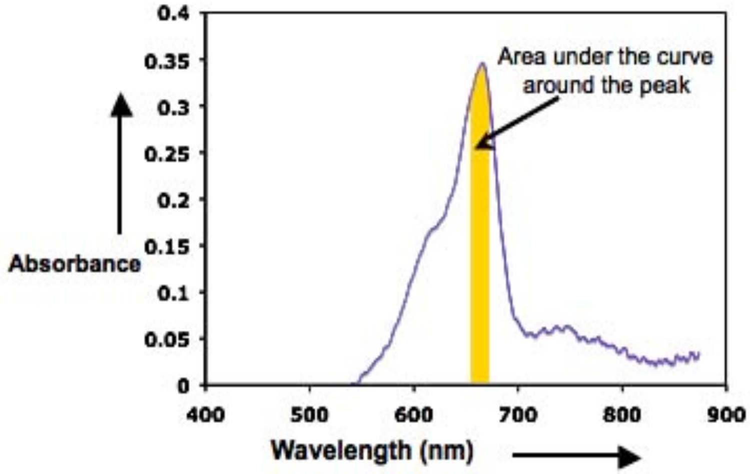

Figure 6.6 – An example of Absorbance vs. Wavelength plot obtained from the spectrometer also showing the region where area under the curve is calculated (wavelength 650.19 – 675.19 nm).

wavelength. The area under the spectrum can be plotted as a function of composition at any of the experimental time intervals, as shown in **Fig. 6.7.**

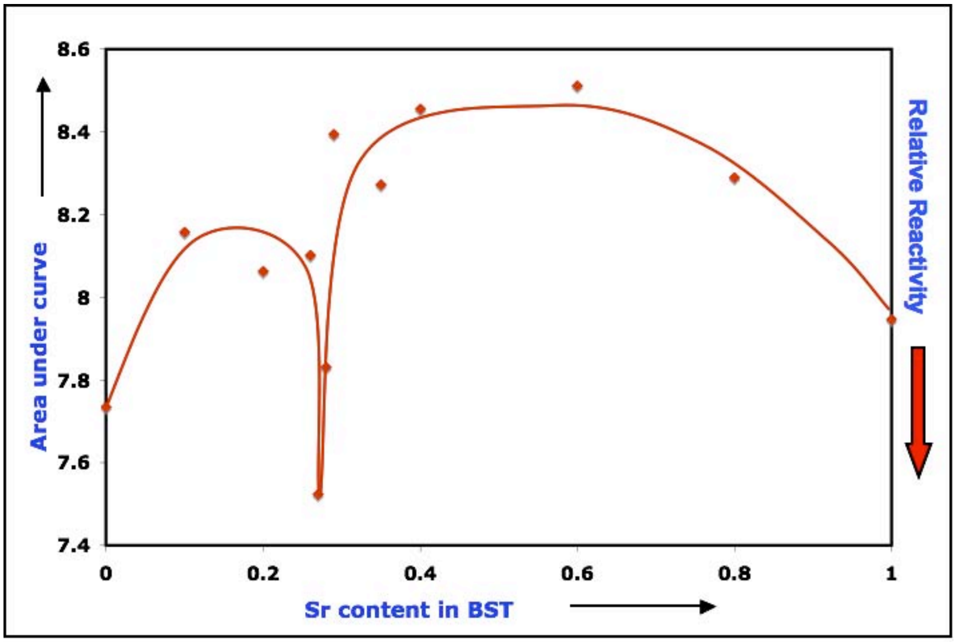

Figure 6.7 – Graph of area under the curve of absorbance vs. wavelength plots near the peak and composition. Lower values on the y-axis represent higher reactivities of the samples. The uncertainty in data points is ± 0.1 Area under the curve units. The line in this plot is drawn as a guide to visualize the trends in the data.

A lower value of absorbance or area under the curve represents a greater change in the color of the dye or more reactivity for that sample for a fixed illumination time as compared to the other sample. To represent higher reactivity as a peak in the graph, similar plots can be drawn with the abscissa representing the "composition" and the ordinate representing "(constant – absorbance/area)" value, as in **Fig. 6.8**, and this method is used in the remainder of this chapter.

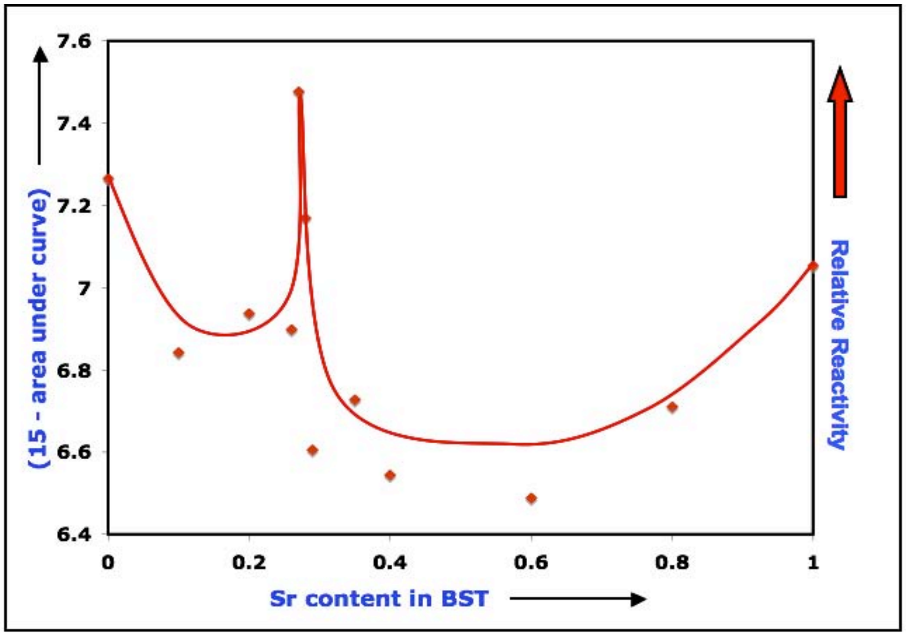

Figure 6.8 – Graph of (15 – area under the curve of absorbance) vs. wavelength plots near the peak and composition. Lower values on the y-axis represent higher reactivities of the samples. The uncertainty in data points is ± 0.1 Area under the curve units. The line in this plot is drawn as a guide to visualize the trends in the data.

6.4.1.3. Absorbance Spectroscopy Results.

6.4.1.3(a) *Constant Temperature Compositional Effect on Photochemical Reactivity of $Sr_xBa_{1-x}TiO_3$.*

Figure 6.9 shows the photochemical reactivity of $Sr_xBa_{1-x}TiO_3$ as a function of x. The experiments were carried out for 200 min in a 5×10^{-6} M methylene blue solution. The experiment is repeated for some compositions and the average values of the area under the curve at all the intervals of illumination time are measured. The variation in the slopes of the decay plots for the same composition in the repeated experiments varies by less than 15 %. Also, in these repeated experiments with a single composition, the absorbance and area under the curve values for similar UV exposures lie within the experimental error range (described in **Section 6.4.1.4**). This validates the reproducibility of these experiments. The results consistently show a peak in reactivity at the transition from the ferroelectric to the non-ferroelectric phase. The pure materials, $BaTiO_3$ and $SrTiO_{3,}$ also show relatively high reactivity.

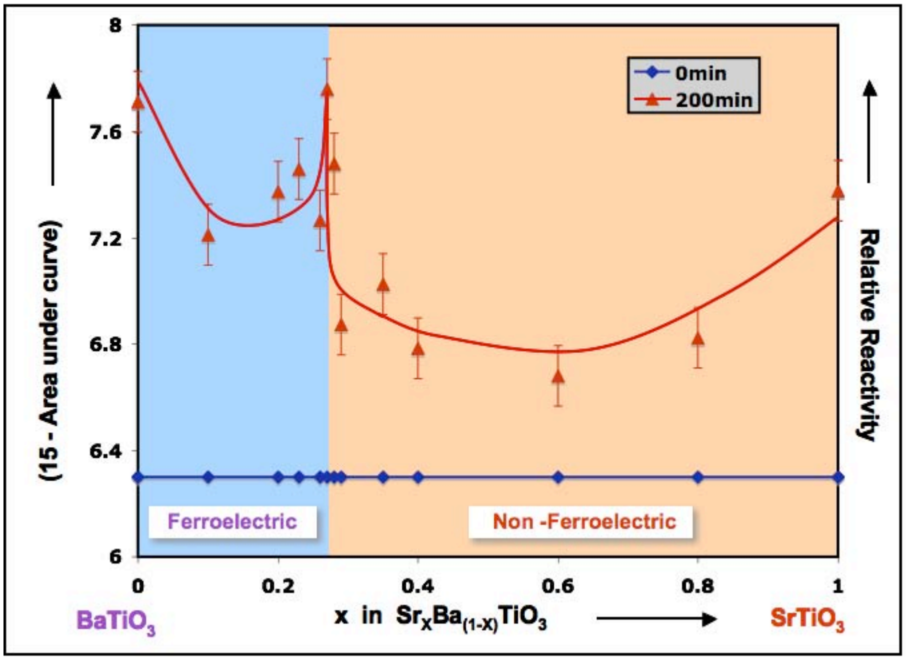

Figure 6.9 – (15-Area under the curve near the peak) v/s x (mole fraction of Sr in $Sr_xBa_{(1-x)}TiO_3$ samples) zero minute and 200 min exposure time for experiments done in 5×10^{-6} M methylene blue solution. The uncertainty in data points is ± 0.12 Area under the curve units. The line in this plot is drawn as a guide to visualize the trends in the data.

The experiments were repeated with a different dye concentration (1×10^{-5} M methylene blue dye solution) for compositions around the phase transition and a similar peak in reactivity was observed (**Fig. 6.10**).

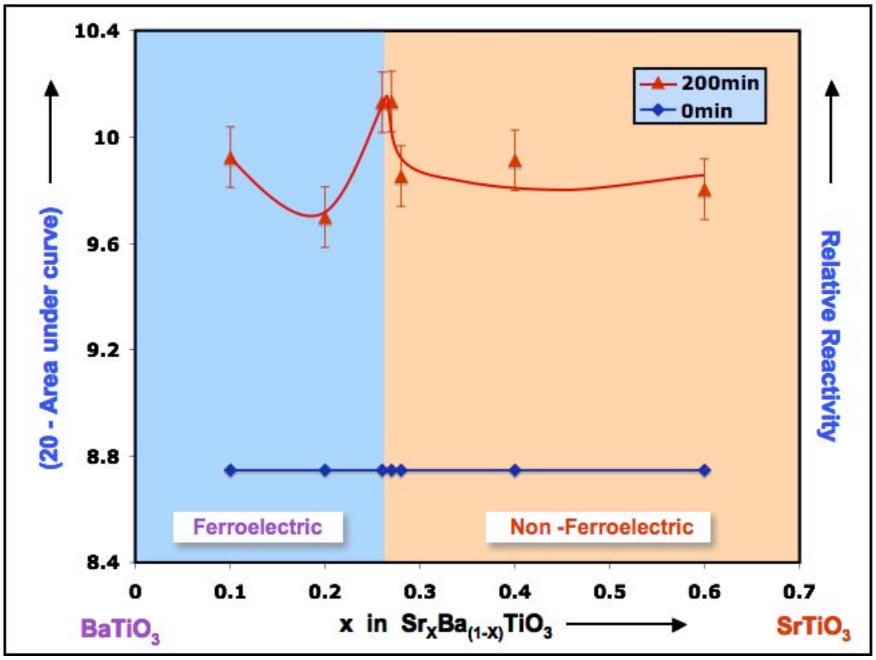

Figure 6.10– (20-Area under the curve near the peak) v/s x (mole fraction of Sr in $Sr_xBa_{(1-x)}TiO_3$ samples) zero minute and 200 min exposure time for experiments done in 1×10^{-5} M methylene blue solution. The uncertainty in data points is ± 0.12 Area under the curve units. The line in this plot is drawn as a guide to visualize the trends in the data.

6.4.1.3(b) *Temperature Effect on the Photochemical Reactivity of $Sr_{0.23}Ba_{0.77}TiO_3$.*

Another set of experiments was conducted with $Sr_{0.23}Ba_{0.77}TiO_3$ samples at different temperatures to determine how the reactivity changed when it transformed from the ferroelectric to paraelectric state. The quartz reactor was placed on a hot plate with a magnetic stirrer and a temperature probe attachment. The temperature probe was in contact with the dye solution at all times to maintain constant temperature during the experiment. A fresh $Sr_{0.23}Ba_{0.77}TiO_3$ pellet was used for each experiment at different temperatures. The analysis of the data and the error correction was carried out exactly as in the earlier two experiments. **Figure 6.11** shows the decay plots for different temperatures.

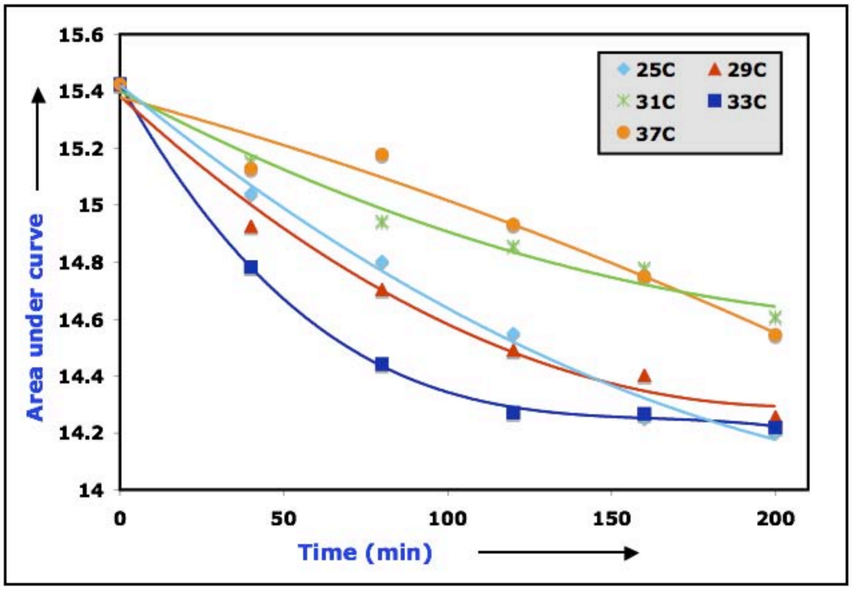

Figure 6.11 – Decay plots for methylene blue photodegradation using $Sr_{0.23}Ba_{0.77}TiO_3$ samples at different temperatures. The uncertainty in data points is ± 0.01 Area under the curve units which is less than the size of the points on this plot.

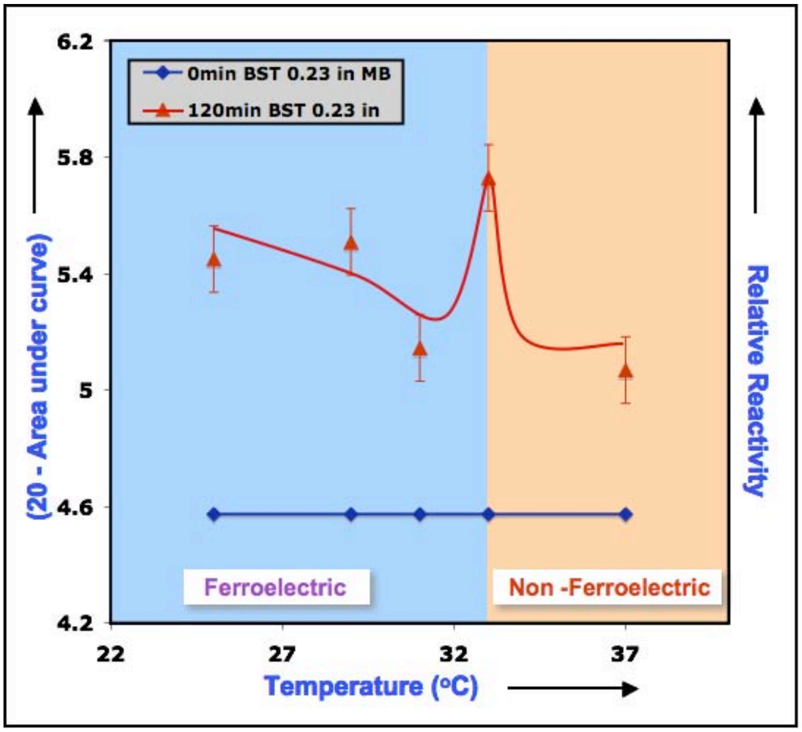

Figure 6.12 – (20-Area under the curve near the peak) v/s temperature (°C) at corrected zero min and 200 min exposure time for experiments carried out with $Sr_{0.23}Ba_{0.77}TiO_3$ samples in 1×10^{-5} M methylene blue dye solution. The uncertainty in data points is ± 0.12 Area under the curve units. The line in this plot is drawn as a guide to visualize the trends in the data.

It is observed that these plots do not exhibit linear decay of the dye at higher temperatures. It is likely due to the evaporation of water in the dye solution at higher temperatures making the solution more concentrated as time passed and competing with the decay of the dye due to the reaction with the sample. However, the maximum decay rate of the dye is at 33 °C. The data are compiled in **Fig. 6.12**, which shows the photochemical reactivity of $Sr_{0.23}Ba_{0.77}TiO_3$ at different temperatures after 120 min of UV irradiation. This set of experiments is also consistent with the observation that increased reactivity occurs close to the transition temperature.

6.4.1.3(c) *Effect of Debye Length and Space Charge Layer Width on Photochemical Reactivity.*

The Debye length and space charge layer widths affect the charge carrier separation in a material and therefore affect the reactivity. To study the effect of Debye length and space charge layer widths on photochemical reactivity, the reactivity of two samples with different Debye lengths and space charge layer widths were compared. As mentioned in **Section 2.4.2**, Debye length and space charge layer width are sensitive to the donor density.

If the donor density (N_D) of $BaTiO_3$ is changed by a small amount, the dielectric constant (ε_r) and polarization (P_S), should not be affected. Kim *et al.* [4] have reported that the unit cell dimension of $BaTiO_3$ in the direction of Ti^{4+} displacement reduces by 1.25×10^{-4} nm on adding 0.5 mole % Y_2O_3. Assuming that the length of the dipole in each unit cell is also reduced by the same amount, the value of P_S reduces by less than 1 % [5]. This is an insignificant change in P_S and can therefore be ignored. Hence it is assumed that any change in the Debye length and space charge layer widths by adding a small amount of dopant in $BaTiO_3$ is due to the increase in donor density. The samples compared in this experiment are $BaTiO_3$ and 0.5 mole % Y_2O_3 doped $BaTiO_3$ (N_D = 8.8×10^{19} per cm^3). It has been reported that Y_2O_3 concentrations, up to 0.5 mole %, Y^{3+} ions substitute at Ba sites in the $BaTiO_3$ lattice and act as donors [4, 6-8]. The defect reaction is shown in **Eqn. 6.1** [6].

$$Y_2O_3 + 2TiO_2 \rightarrow 2Y_{Ba}^{\bullet} + 2Ti_{Ti} + 6O_O + 1/2\,O_2 + 2e' \qquad \text{---(6.1)}$$

Because Debye length and space charge layer width vary inversely with N_D and the square root of N_D respectively, donor doping decreases the Debye length and space charge layer widths. It is also important to note that the addition of Y_2O_3 adds impurity levels in the band gap of $BaTiO_3$ that will increase the efficiency of non – radiative electron transitions and therefore should affect the reactivity. The decay plots for 5×10^{-6} M methylene blue solutions reacted with $BaTiO_3$ and 0.5 mole % Y_2O_3 doped $BaTiO_3$ are shown in **Fig. 6.13**. The rate of dye degradation for doped $BaTiO_3$ is lower than that of undoped $BaTiO_3$.

6.4.1.4. Error Analysis and Control Experiments – Absorbance Spectroscopy.

To understand the above mentioned results (**Section 6.4.1.3**), it is important to explain the control experiments and how the error bars in the results are calculated and what they represent. The absorbance has errors from two sources – (a) the instrument error from the spectrometer and (b) the experimental error in the dye solution concentration inculcated due to the making of a fresh dye solution for each experiment.

The error bars for the absorbance data were determined by adding the error from these two sources. An estimate of theses errors is made in the remainder of this section.

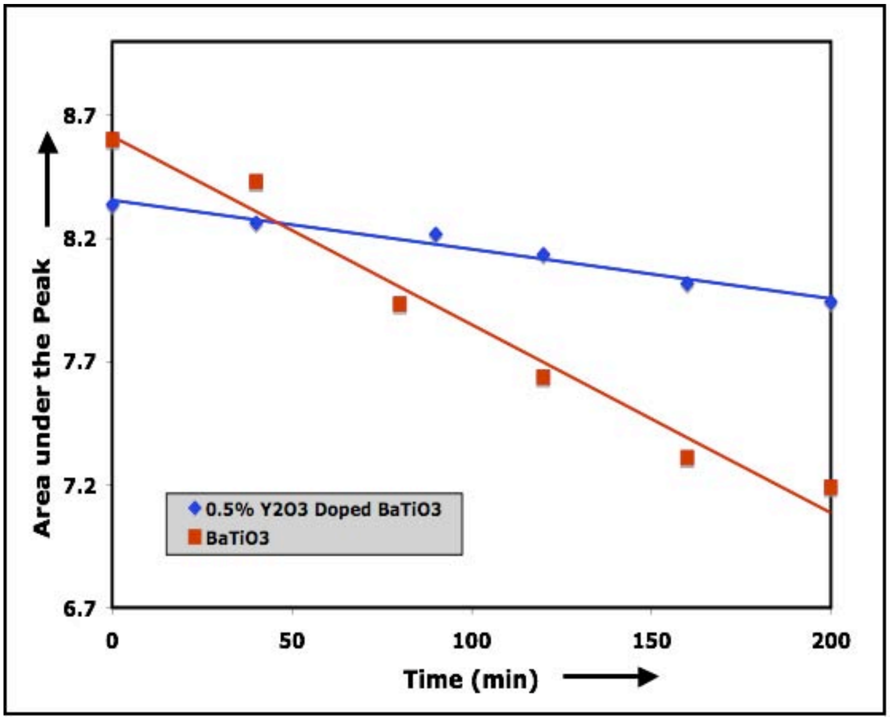

Figure 6.13 – Decay plots for methylene blue dye photodegradation using $BaTiO_3$ and 0.5 mole % Y_2O_3 doped $BaTiO_3$. The uncertainty in data points is ± 0.01 Area under the curve units which is less than the size of the points on this plot.

6.4.1.4(a) *Instrument error.*

As mentioned in **Section 5.2.1.1(b)**, errors in the measured absorbance and area under the curve values are approximately 0.1 % and 0.2 % respectively. These are very small compared to the other sources of uncertainty.

6.4.1.4(b) *Experimental error.*

As mentioned in the experimental details (**Section 5.1.4**), for each experiment the dye solution is made by diluting the concentrated 4×10^{-5} M methylene blue solution with deionized water. It is impossible to make the solution exactly same each time. The starting concentrations of the dye solutions therefore vary slightly for each experiment. To estimate this variation, nine samples of 200 ml of the dye solution and 5×10^{-6} M concentration were prepared and absorbance spectra were recorded. The standard deviation in the absorbance values at 665 nm is 1.2 % of the average absorbance of the nine dye solutions at this wavelength. The standard deviation in the area values in the wavelength range of 650.19 to 675.19 nm for the nine dye solutions is 1.1 % of the average area value of all the dye solutions

Along with these error estimates, some control experiments are also conducted to understand the rate of decay of the dye with time in the dark and in ambient light, with and without a sample, and the influence of pH on the rate of decay of the dye.

6.4.1.4 (i) *Effect of pH.*

When an oxide is immersed in an aqueous solution, anions and cations from the liquid adsorb on the surface sites. If the oxide absorbs more anions from the solution, the solution becomes more acidic and the oxide is called a “solid acid”. If the oxide adsorbs more cations, it is called a “solid base”. In both cases the pH of the solution is changed when the oxide is added to the solution. Also, the adsorption of anions creates a negatively charged surface and the adsorption of cations creates a positively charged surface. In other words, space charge double layers are created and the conduction band and valence band positions at the surface are altered. However, the net charge adsorbed depends on the pH of the solution [9]. Negative surface charge causes the bands to bend upwards and a positive surface charge causes the bands to bend downwards (**Section**

2.4.2). As explained in **Section 2.4.2**, this band bending can influence reactivity. It has been reported by C. Lizama *et. al.* [10] that the rate of photodegradation of Reactive Blue 19 dye in the presence of TiO_2 and ZnO catalysts can be increased by optimizing the pH and concentration of the dye solution and the amount of catalyst added. The change in pH was however very drastic to enhance the dye degradation (from ~6.1 to 11 pH).

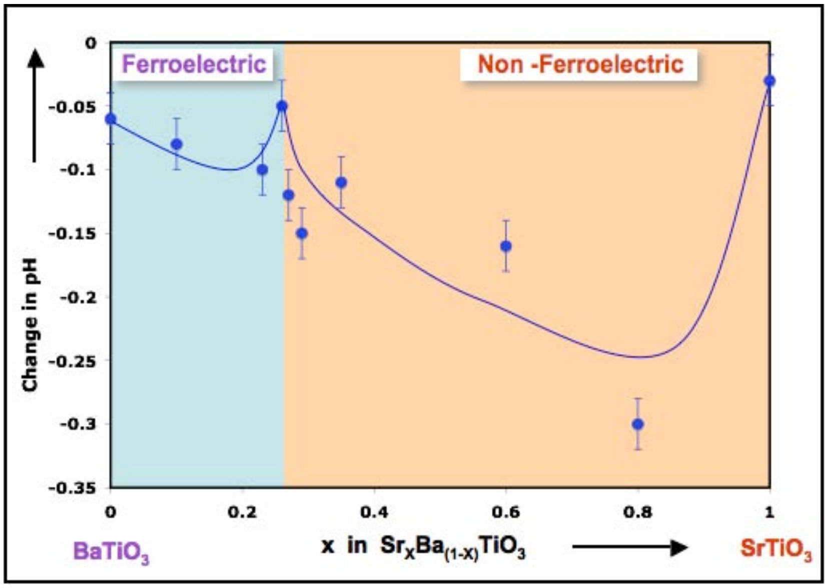

Figure 6.14 – Change in the pH of 200 ml 5×10^{-6} M methylene blue dye solution on addition of $Sr_xBa_{1-x}TiO_3$ samples. The uncertainty in data points is ± 0.02 pH units. The line in this plot is drawn as a guide to visualize the trends in the data

The changes in pH on immersing $Sr_xBa_{1-x}TiO_3$ samples of different compositions in a 5×10^{-6} M methylene blue solution were measured. The pH of the dye solution was measured before immersing the sample and after immersing the sample and magnetically stirring the dye solution for 10 min. A Datalogging pH meter by Sper Scientific Ltd. with accuracy of ±0.02 pH was used to measure the pH. The change in pH on adding different $Sr_xBa_{1-x}TiO_3$ to the dye solution is shown in **Fig. 6.14**. The pH of the starting solutions varies in the range of (6.1 – 6.5) ±0.02. On adding $Sr_xBa_{1-x}TiO_3$ the pH decreases or the solution becomes slightly acidic (the ordinate scale is negative). It can be seen that the change in pH is the least for the pure compositions ($BaTiO_3$ and $SrTiO_3$) and the composition at the ferroelectric to non-ferroelectric transition.

Because methylene blue is an acid – base dye, the change in pH affects the color of the dye. **Figure 6.15** shows the zero minute area under the absorption peak for different compositions of $Sr_xBa_{1-x}TiO_3$. Zero minute measurements are recorded just before the UV lamp is turned on. Comparing **Fig. 6.14 and Fig. 6.15**, it can be seen that they show approximately the same trend. The pure compositions and the transition compositions that have the least change in pH also have the lowest area absorbance. This shows that the immersion of these $Sr_xBa_{1-x}TiO_3$ compositions that alter the pH of the dye solution by the smallest amount simultaneously alters the concentration of colored dye ions from the starting concentration by the smallest amount. These changes in the color of the dye solution are however small compared to the total uncertainty, which is ± 0.22 area units.

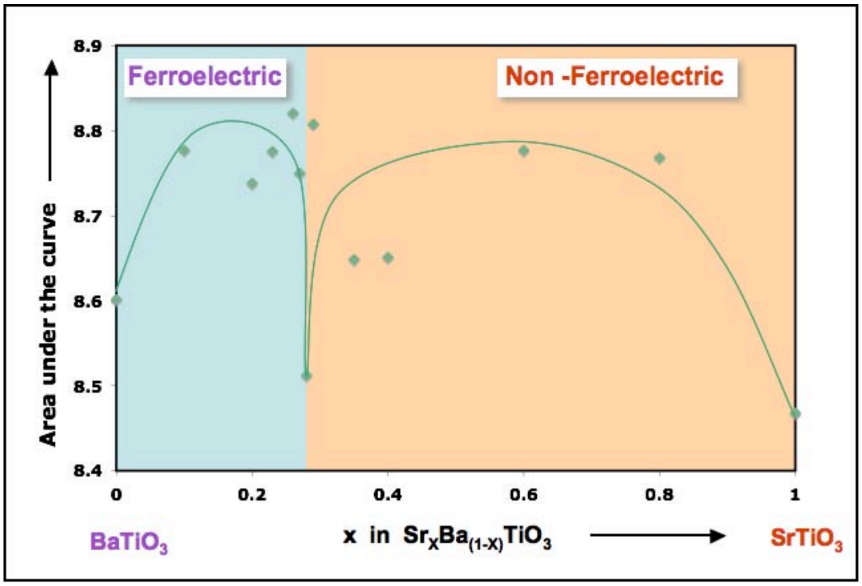

Figure 6.15 – Graph of area under the curve (of absorbance vs. wavelength plots near the peak) vs. composition at zero minute when 200 ml 5×10^{-6} M methylene blue dye solution is used. The uncertainty in data points is ± 0.22 Area under the curve units. The line in this plot is drawn as a guide to visualize the trends in the data.

Knowing that the color of the dye solution is affected by the pH, it is important to see if the pH of the starting dye solutions affect the rate photodegradation of the dye. This needs to be tested because it is the rate of color change of the dye (or the net change in the color of the dye for a certain duration of UV illumination) that is representative of the reactivity. For this purpose two more experiments were done with the same $Sr_xBa_{1-x}TiO_3$ composition samples in dye solutions deliberately made more acidic and more basic than the typical fluctuation in pH of the dye solutions used in all of the experiments. The rates of color change of the dye for these two experiments are then compared with the rate when the same composition is reacted with a normally prepared dye solution. If these solutions with pH greater than or less than the normal range do not show any difference in the dye decay rate then the effect of pH on the difference in reactivity for different $Sr_xBa_{1-x}TiO_3$ samples can be ruled out. As mentioned above, the pH of the starting solutions varies in the range of (6.1 – 6.5)±0.02. The dye solution is made more acidic by adding aqueous H_2SO_4 to achieve a starting pH of 5.64±0.02 and is made more basic by adding aqueous NaOH to achieve a pH of 7.15±0.02. The experiments are carried out in exactly the same way as the other absorbance experiments. $Sr_{0.29}Ba_{0.71}TiO_3$ samples and 5×10^{-6} M methylene blue dye solution are used. **Fig. 6.16** shows the decay plots for these three cases. The variation in the slopes of these decay plots is approximately 20 %. Recall form **Section 6.4.1.3(a)** that the slopes in repeated experiments on the same material varied by 15 %. Therefore, the differences between these plots are only marginally larger than typical experimental uncertainty and it can be concluded that though it is possible to change the photodegradation rate of the dyes by altering the pH, it is not significant in the pH range of the dye solution in this research.

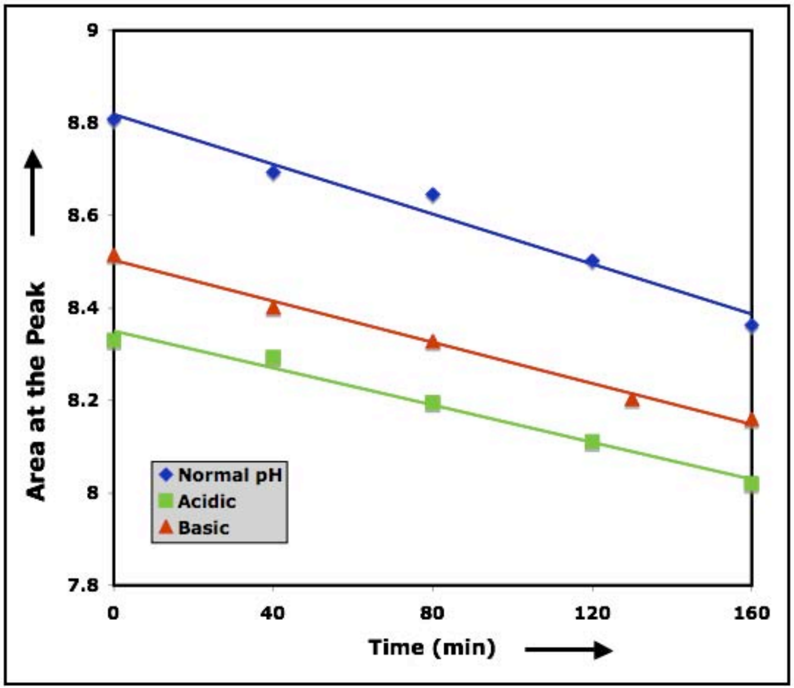

Figure 6.16 – Decay plots for photodegradation of 5×10^{-6} M methylene blue dye solutions of different pH values in the presence of $Sr_{0.29}Ba_{0.71}TiO_3$ samples. The uncertainty in data points is ± 0.01 Area under the curve units which is less than the size of the points on this plot.

The addition of $Sr_xBa_{1-x}TiO_3$ samples of different compositions makes the dye solution more acidic by varying amounts. This variation in the pH change indicates dissimilar adsorption of negative ions from the solution. To understand the role of adsorbed ions on reactivity, the mechanism of dye – sample interaction needs to be considered. As shown in **Section 6.3**, reduction of methylene blue dye occurs on the positive domains and the reduced dye accumulates on the surface. The presence of negatively charged ions adsorbed on the surface of $Sr_xBa_{1-x}TiO_3$ samples will not favor this reaction. Furthermore, for the reduction reaction to occur, positively charged dye ions react on the positively charged domains. The adsorption of positive ions on positive domains is unlikely. Therefore, the adsorption of negative ions in varying amounts on $Sr_xBa_{1-x}TiO_3$ surfaces during the initial equilibration with the methylene blue solution does not appear to be a plausible explanation for the composition dependence of the photochemical reactivity.

Another set of experiments was carried out to measure the change in the pH of the dye solution for different $Sr_xBa_{1-x}TiO_3$ samples when they were illuminated by UV light for 2 hrs. On average the pH decreases by 0.25±0.03. One exception was $Sr_{0.1}Ba_{0.9}TiO_3$, for which the pH decreases by 0.55±0.03. The other exceptions were $Sr_{0.8}Ba_{0.2}TiO_3$ and $SrTiO_3$, for which pH actually increases by 0.19±0.03. All other changes in pH are within the error of the pH measurement.

6.4.1.4(ii) *Effect of Room Light*.

Another control experiment was conducted to see if the light in the room (not the light from UV lamp) in which the experiments are conducted affects the color of the dye with and without $Sr_xBa_{1-x}TiO_3$ sample. Because visible light does not have enough energy to generate charge carriers in $Sr_xBa_{1-x}TiO_3$, exposure to room light should not change the color of the dye solution. To test that idea, 200 ml of a 5×10^{-6} M methylene blue solution was placed in two separate beakers. A $SrTiO_3$ pellet was added to one beaker, the solution was stirred for a few minutes, and it was then placed in the dark for 20 min to let the pellet reach adsorption equilibrium with the dye solution. Both beakers were then exposed to the room light and absorbance spectra were recorded every 40 min, as in the other experiments. The decay rates of the dye for both these cases are shown in **Fig. 6.17**. As expected there is no difference in the rate of color change of the dye with and without $SrTiO_3$. In fact, there is no noticeable color change for this duration of exposure to room light. The standard deviation of these absorbance measurements is 1.2 % and this is characteristic of all of the absorbance measurements in this thesis.

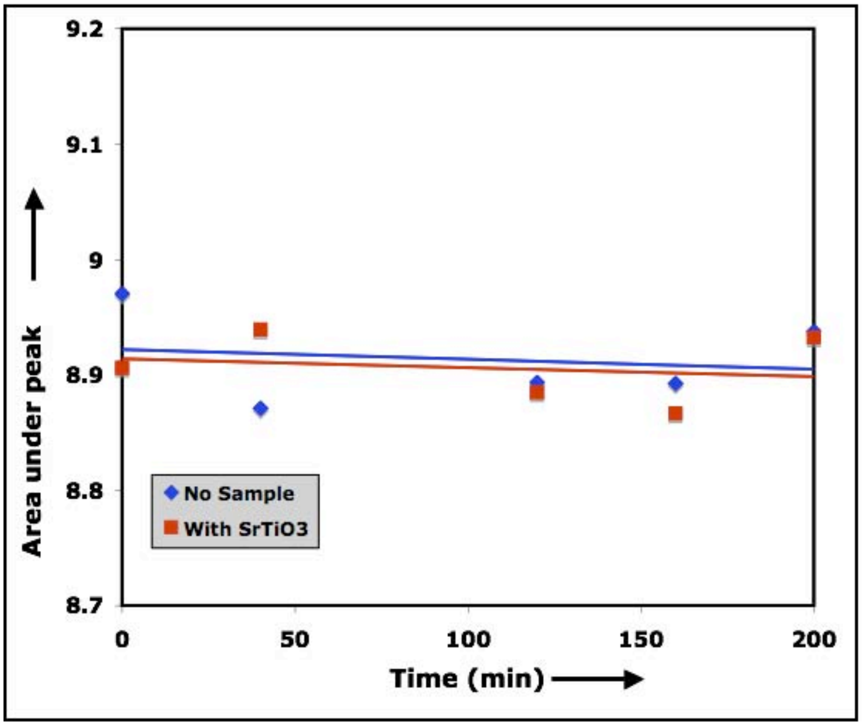

Figure 6.17 – Decay plots of 5×10^{-6} M methylene blue dye photodegradation in room light only, with and without a $Sr_xBa_{1-x}TiO_3$ sample ($SrTiO_3$ in this case). The uncertainty in data points is ± 0.13 Area under the curve units.

6.4.1.4(iii) *Variation in Darkness.*

Nine different compositions of $Sr_xBa_{1-x}TiO_3$ were immersed in 200 ml of a 5×10^{-6} M methylene blue solution and were kept in the dark for over 20 hrs. As for the samples left in room light, there was no change in color and the standard deviation of the absorbance values was 1.2 %.

6.4.1.5. Correction for Differences in the Initial Absorption.

Figure 6.18 shows the measured absorbance for all of the $Sr_xBa_{1-x}TiO_3$ compositions at zero minutes (or before the UV lamp is turned on). To compare the reactivities of the different compositions, they should all have the same initial absorbance. However, because of uncertainties in the initial solution concentration and changes that occur when

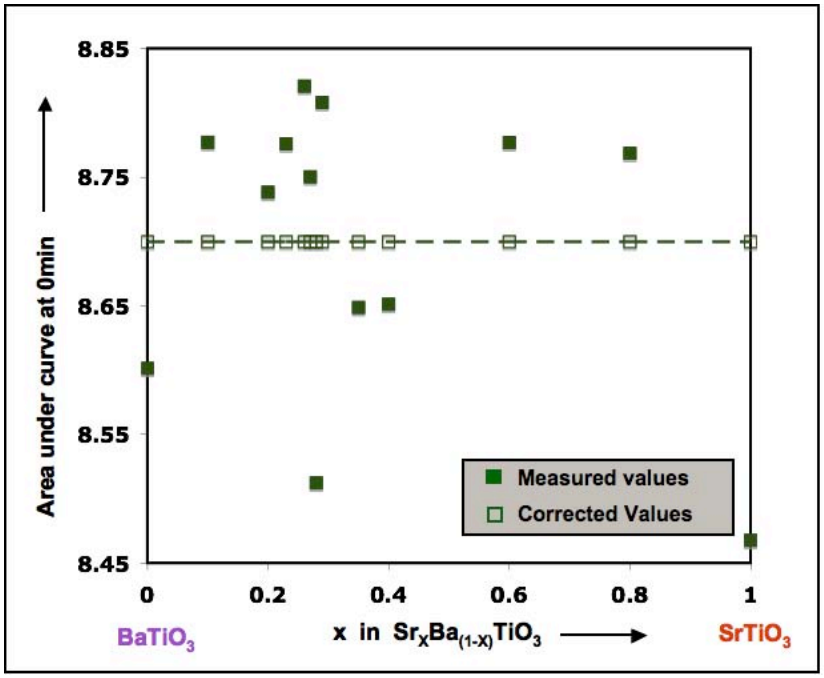

Figure 6.18 – Plot of area under the curve around the peak v/s composition of $Sr_xBa_{(1-x)}TiO_3$ before and after correction in the zero minute values.

the sample equilibrates with the solution, the values are not identical. To compensate for these initial fluctuations, the average of the zero minute absorbance values of all the samples is calculated at the wavelengths around the peak in absorbance vs. wavelength data. The difference between this average value and the experimentally obtained absorbance values for each sample is also calculated at these wavelengths. This difference in the absorbance values for each sample is then added to the rest of the absorbance values for the same wavelengths but different illumination times for that sample. In doing so, all six data points at various illumination times for a sample are shifted by the same amount and hence the slope of the decay plot is not affected. This method is illustrated in **Fig. 6.19**. Finally, it should be noted that correcting the initial absorbance values does not remove all of the uncertainty. For example, the absorbances of the samples in the dark still had a standard deviation of 1.2 %, so this value is used for the error bars for the results in **Fig. 6.9, 6.10, and 6.12**.

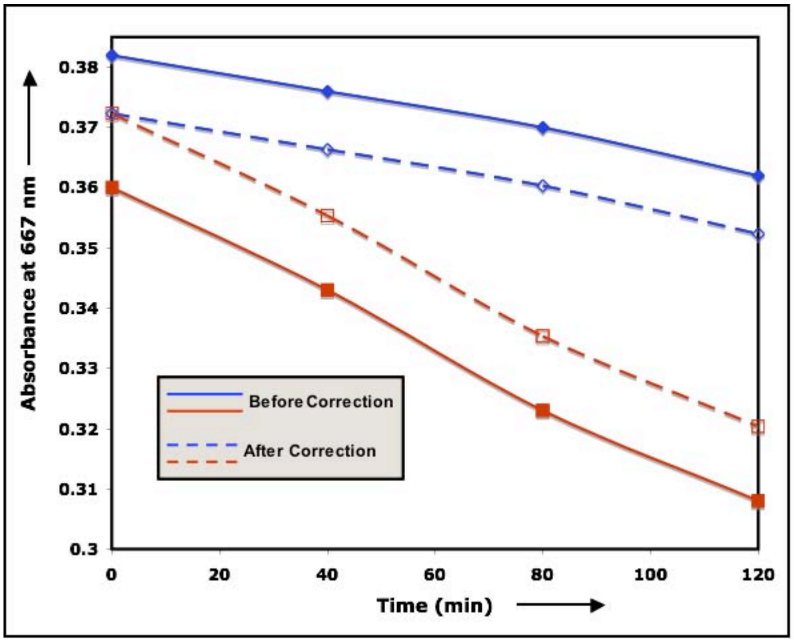

Figure 6.19 – Decay plots of two different $Sr_xBa_{(1-x)}TiO_3$ compositions before and after error correction. The uncertainty in data points is ± 0.01 Area under the curve units which is less than the size of the points on this plot.

Figure 6.20 shows the zero minute measurements with and without correction and the effect of this correction on the measurements after 120 min of UV illumination. It is observed that the zero minute measurements correction does not affect the measurements at higher illumination times significantly (though these measurements are more accurate after being corrected). However, it must also be noted that the zero minute readings exhibit the same overall trend as the data after UV exposure. The trends are also consistent with the initial trends in the pH (see **Fig. 6.14**) and the color change (see **Fig. 6.15**) of the solution. This suggests that there are interactions between the solid and the solution during the formation of the solid/solution interface before illumination that influence the composition dependence of the reactivity.

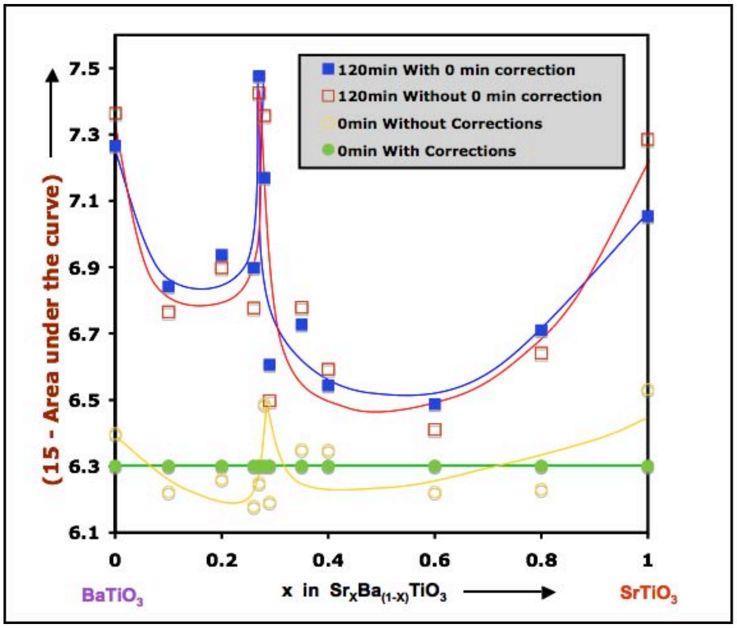

Figure 6.20 – (15-Area under the curve near the peak) v/s x (mole fraction of Sr in $Sr_xBa_{(1-x)}TiO_3$ samples) at zero minute and 120 min exposure times with and without the zero minute corrections for experiments done in 5×10^{-6} M methylene blue dye solution. The lines in this plot are drawn as a guide to visualize the trends in the data.

6.4.2 *Diffuse Reflectance Spectroscopy*.

The photochemical reactivities of different compositions of $Sr_xBa_{1-x}TiO_3$ were also compared by observing the color of the dye on the sample surface using diffuse reflectance spectroscopy. The experimental set up was the same as that shown in **Fig. 5.5**. The concentration of the methylene blue solution was 1×10^{-5} M. After 40 min of irradiation, the samples were removed and are air dried. For each $Sr_xBa_{1-x}TiO_3$ sample, four diffuse reflectance spectra are recorded at different locations from the region of the sample surface where the dye is adsorbed. The average of these four measurements is used for comparison with other samples. Applying the concept of diffuse reflectance (explained in **Section 5.2.1.1(a)**) to the samples used in the current research, when radiation falls on the sample during diffuse reflectance measurement, a portion of it penetrates the dye layer and is emitted as diffuse reflection **(Fig. 6.21)**. This reflected radiation is affected by the color of the dye on the surface because the color signifies absorption of certain wavelengths of the spectrum (dark color signifies more absorption of radiation and hence less radiation). At the same time, the color of the dye depends on photochemical reactivity of the material. Hence the diffuse reflectance spectrum is directly related to the reactivity of the sample.

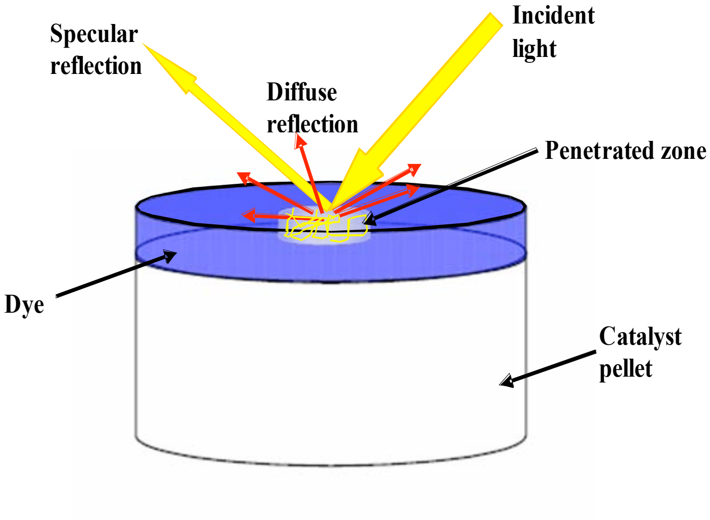

Figure 6.21 – Different types of reflections that take place during diffuse reflection measurement on the pellet with adsorbed dye after UV illumination.

Reflectance measurements as a function of composition are used to determine the relative reactivities of the samples. A more reactive sample will have more dye adsorbed on the illuminated surface and hence it will be darker than the surface of a less reactive sample. Darker color signifies less reflection and hence the % Reflectance will be the least for the most reactive sample. Therefore to represent high reactivity on the positive axis, a plot of (100 - % Reflectance) vs. composition is shown in **Fig. 6.22**. This experiment was repeated for each sample and the reported values of % R are an average of the values obtained from both the experiments. The difference in the % R values from the two experiments was calculated for each sample. The error bars in the plot represent the standard deviation from the average of these differences in % R values. The results from diffuse reflectance spectroscopy show a trend that is similar to that observed by absorbance spectroscopy. The addition of solid solution elements decreases the reactivity of the relatively purer phases and there is a maximum in the reactivity at the ferroelectric to non-ferroelectric phase boundary.

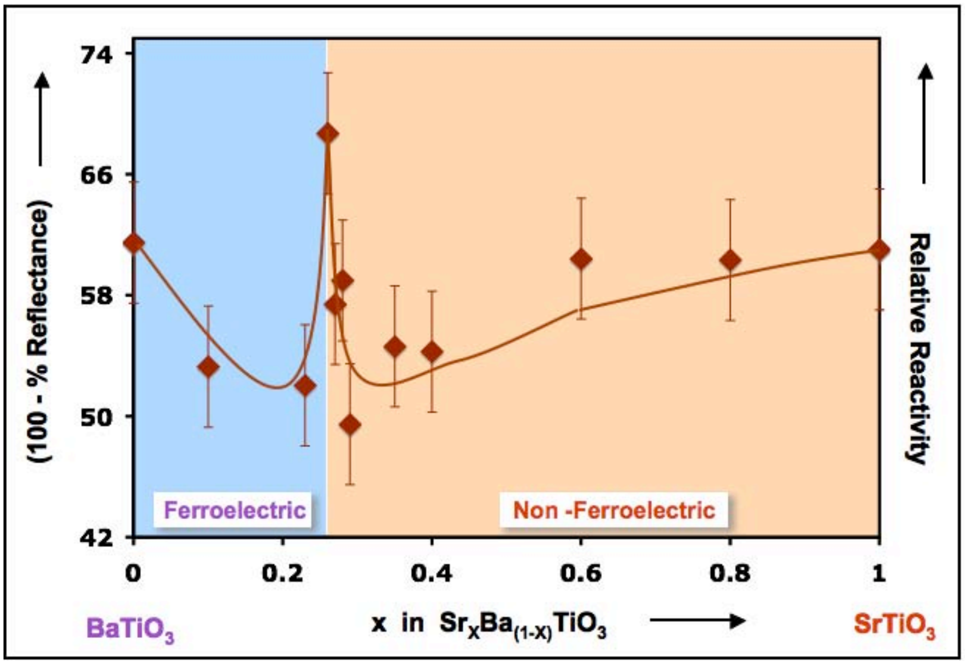

Figure 6.22 – (100 – **%** Reflectance) v/s x (mole fraction of Sr in $Sr_xBa_{(1-x)}TiO_3$ samples) at 656.8nm wavelength.

6.4.3 *Atomic Force Microscopy*.

$Sr_xBa_{1-x}TiO_3$ samples with different compositions were photochemically reacted with a 0.115 M aqueous $AgNO_3$ solution, as shown in **Fig. 5.9**. As explained in **Section 5.2.2.2**, silver ions are reduced and solid silver is left on the surface at the reaction location. The surface is imaged before and after the reaction using AFM [11, 12]. The amounts of silver formed on the surface during the same duration of UV illumination (6 seconds), are taken as measures of photochemical reactivity of the $Sr_xBa_{1-x}TiO_3$ samples.

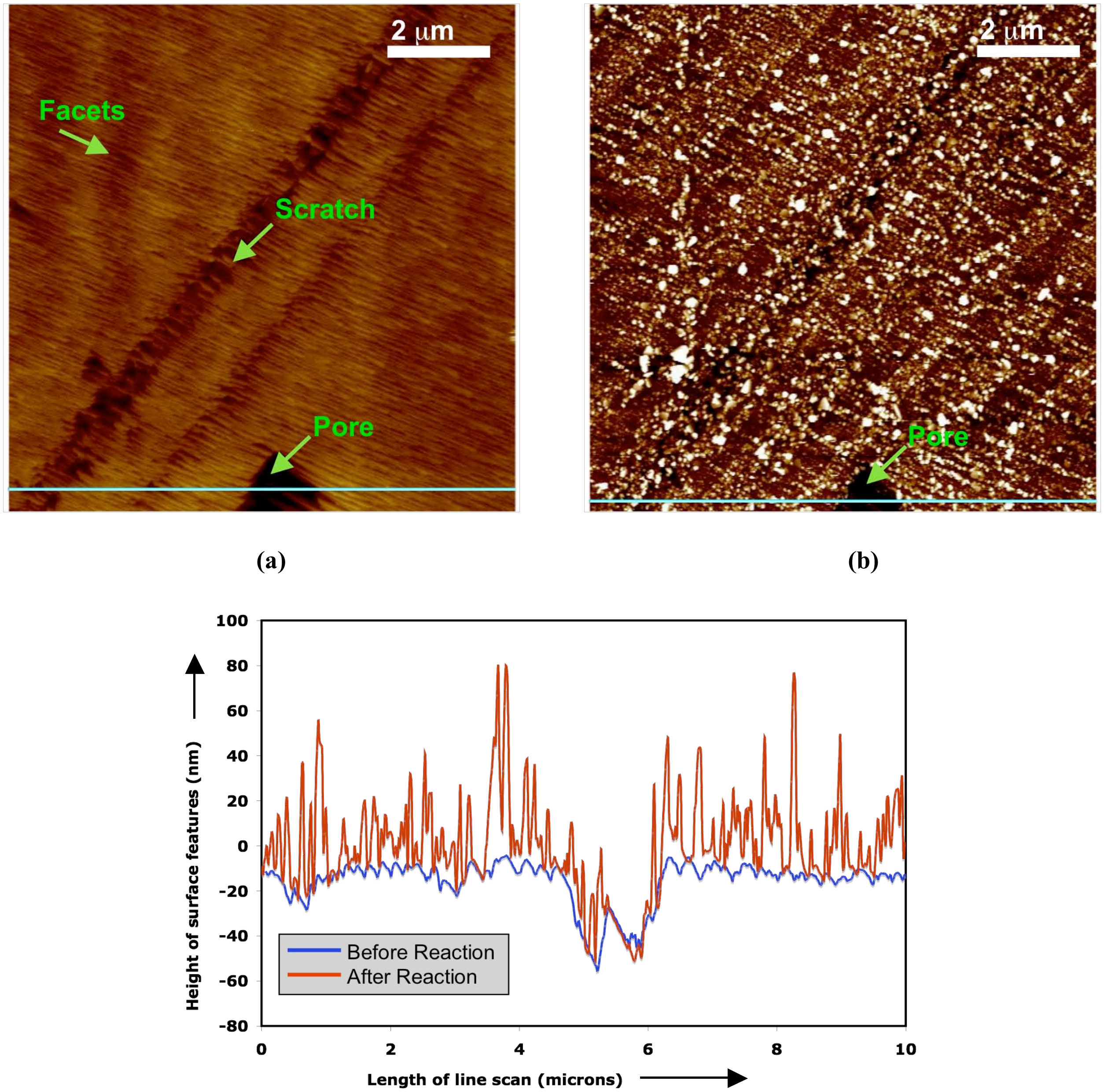

(a)

(b)

(c)

Figure 6.23 – (a) A topographical AFM image of the surface of $Sr_{0.27}Ba_{0.73}TiO_3$ before reaction is pictured. Black-to-white contrast is 60 nm. The contrast in this image is from facets, scratches and pores on the surface and also possibly from domains. **(b)** The topographical AFM image of the surface of $Sr_{0.27}Ba_{0.73}TiO_3$ after reaction with $AgNO_3$ is pictured. Black-to-white contrast is 75 nm. The white contrast in this image is primarily due to Ag. **(c)** Surface height profile along the blue lines on before and after reaction images.

The amount of Ag on the surface is estimated by recording height profiles of the surface at the same location with and without the reaction product. One example is shown in **Fig. 6.23**. **Fig. 6.23 (a) & (b)** show the surface before and after reaction at the same location. Heights of the surface features are recorded along the blue lines on the same spot on both the images. The height profiles are then plotted on the same graph (**Fig. 6.23 (c)**) such that some common features of both the plots coincide. In this example, the common feature is a pore on the surface. In other cases, the common feature might be a grain boundary, scratch or facet, depending on the image. This step is important because the before and after plots shown in **Fig. 6.23 (c)** are recorded at different times on the AFM. The lowest point for both of these height scans is not necessarily at the same x and y axes values when plotted on the same graph. Therefore the values of one of these height scans need to be adjusted such that the common features coincide as shown in **Fig. 6.23 (c)**.

The method used to estimate the amount of silver on the surface is shown in **Fig. 6.24**. **Fig. 6.24 (a)** only depicts **Fig. 6.23 (c)** showing that the grey area is silver and the yellow area is the surface. As shown in **Fig. 6.24 (b)**, to calculate the grey area, the areas under the plots are calculated by integrating the height scan data (after adjustment to coincide at a common feature) for before and after reaction. These areas are called as A_R and A_B for the reacted and un-reacted cases respectively. The difference between these areas is the area of the Ag or $(A_R - A_B) = A_{Ag}$.

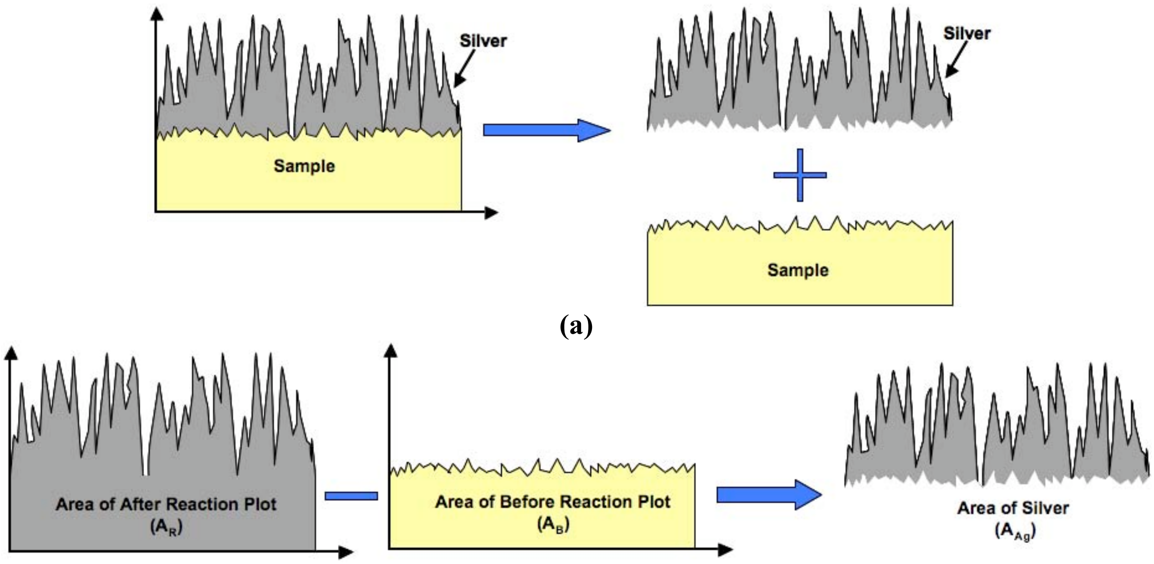

(a)

(b)

Figure 6.24 –Schematic representing **(a)** the surface height profiles of the sample before and after reaction with $AgNO_3$ and **(b)** the area terms used to estimate the amount of silver for a pair of height scans at the same location on the surface of the samples before and after reaction.

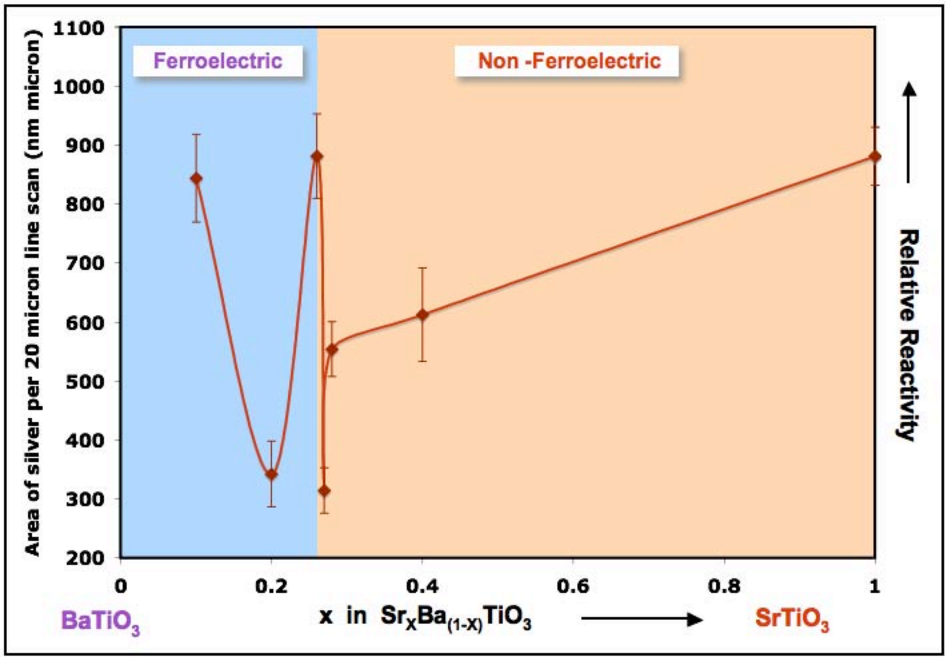

Figure 6.25 – (Area of Ag per pair of height scans of 20 μm lengths at the same location on the surface of the samples before and after reaction) v/s x (mole fraction of Sr in $Sr_xBa_{(1-x)}TiO_3$ samples). The reaction time is 6 seconds for each sample.

Seven different compositions of $Sr_xBa_{1-x}TiO_3$ are analyzed by this method. Three sets of before and after images of 20 μm × 20 μm field of view are taken for each composition. Every set of before and after images for each composition is taken at a different area on the sample surface to include the variation in reactivity due to grain orientation. The A_{Ag} is then calculated for twelve line-scans (four for each image pair) of 20 μm length each. It is however not possible to find common features to coincide the before and after height scan plots perfectly for all the line scans. To deal with this, for each image pair at least one surface feature was perfectly aligned in the before and after reaction height scans. The other height scans for the same image are then adjusted by the same amount. The standard deviation from average A_{Ag} values for each composition is calculated. These average areas of silver (A_{Ag}) for different compositions are then plotted versus the composition for $Sr_xBa_{1-x}TiO_3$ and are shown in **Fig. 6.25**. The error bars represent the standard deviation from average A_{Ag} values for each composition. The trend of reactivity observed by Atomic Force Microscopy is the same as that observed by spectroscopy.

One set of before and after images for eight different $Sr_xBa_{1-x}TiO_3$ compositions (except $Sr_{0.27}Ba_{0.73}TiO_3$ for which two sets are shown) is shown in **Fig. 6.26**. It can be seen from these images that the mode of reaction gradually changes from spatially selective reactivity for $BaTiO_3$ to spatially uniform reactivity for $SrTiO_3$. Evidence for domains disappears completely at the $Sr_{0.28}Ba_{0.72}TiO_3$ composition. For the $Sr_{0.27}Ba_{0.73}TiO_3$ sample, clear evidence for domains is observed in only one of the images, shown in **Fig. 6.26 (i & j)**. The other regions on $Sr_{0.27}Ba_{0.73}TiO_3$ sample display spatially uniform reactivity as shown in **Fig. 6.26 (k & l)**. The $Sr_{0.26}Ba_{0.73}TiO_3$ composition showed highest reactivity (**Fig. 6.25)**.

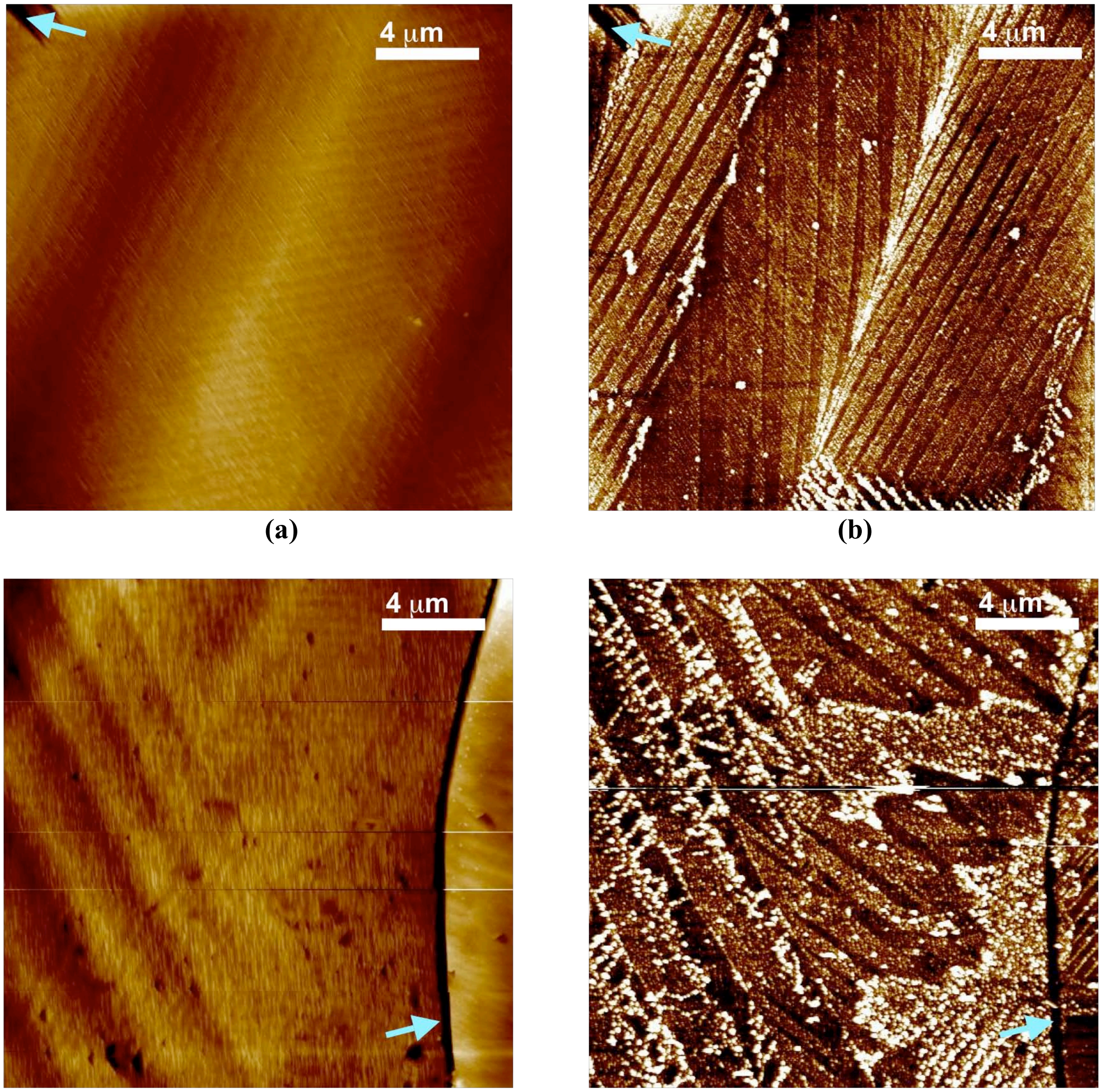

(a) **(b)**

(c) **(d)**

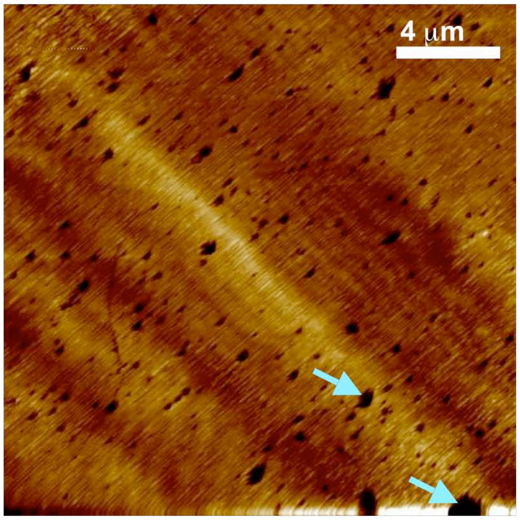

(e)

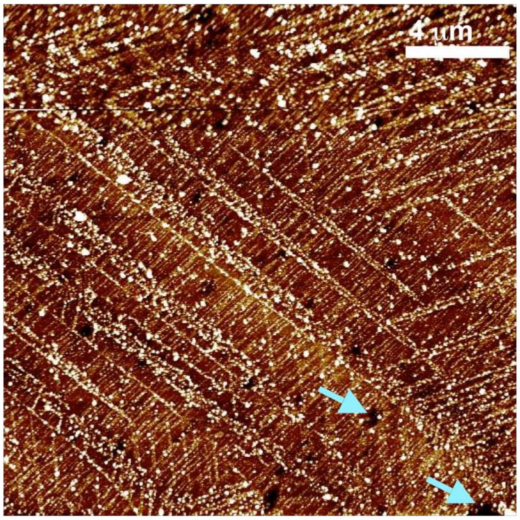

(f)

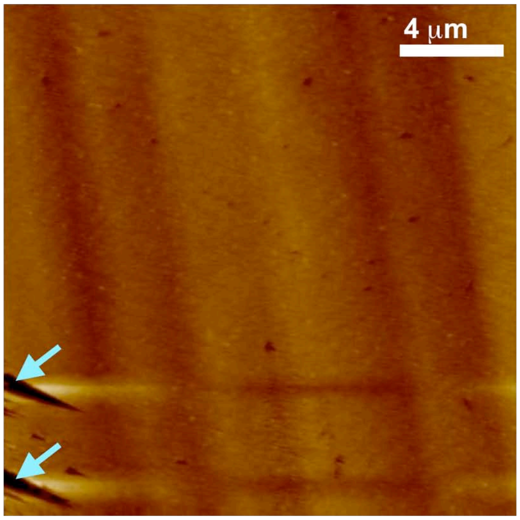

(g)

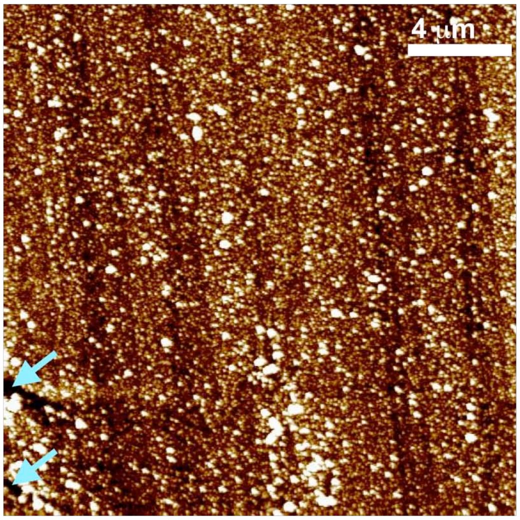

(h)

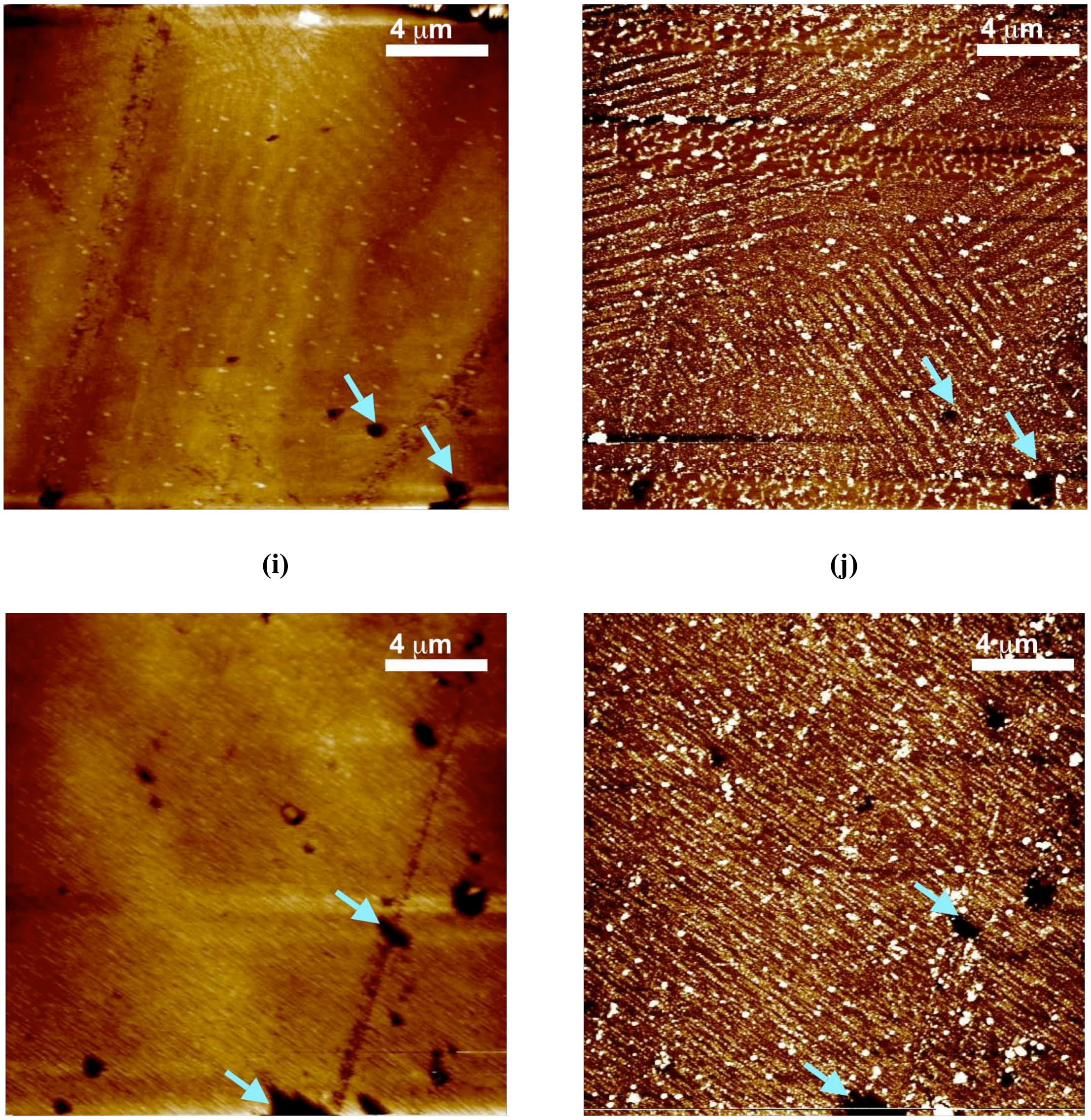

(i)

(j)

(k)

(l)

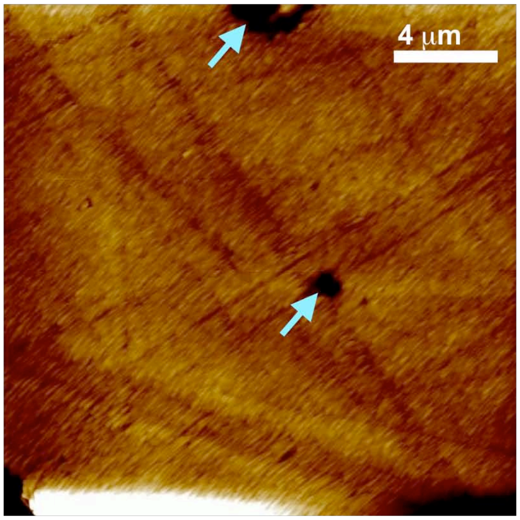

(m)

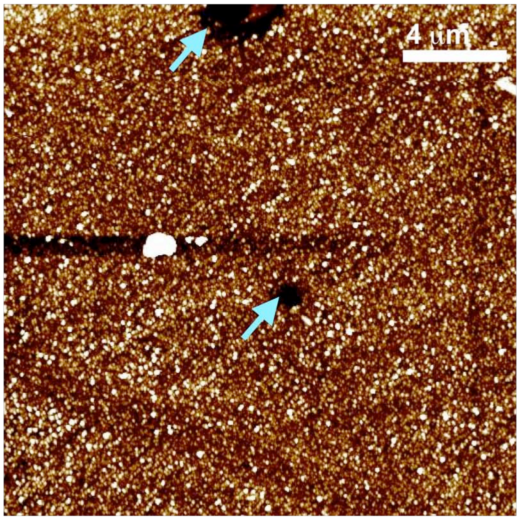

(n)

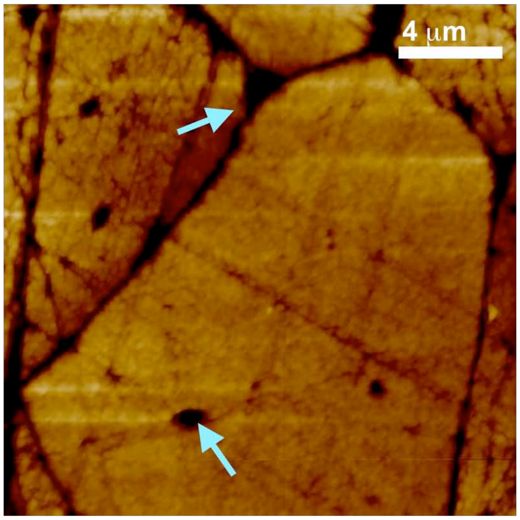

(o)

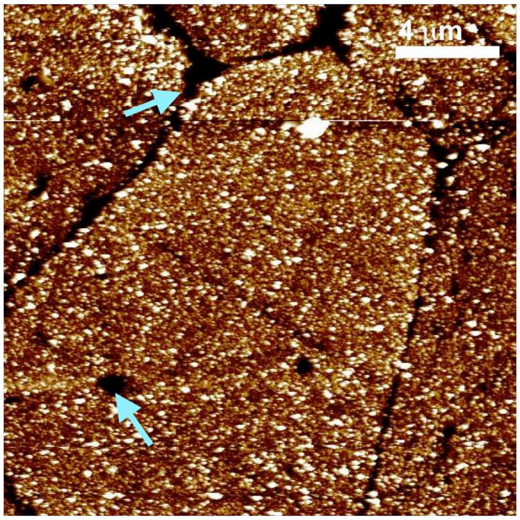

(p)

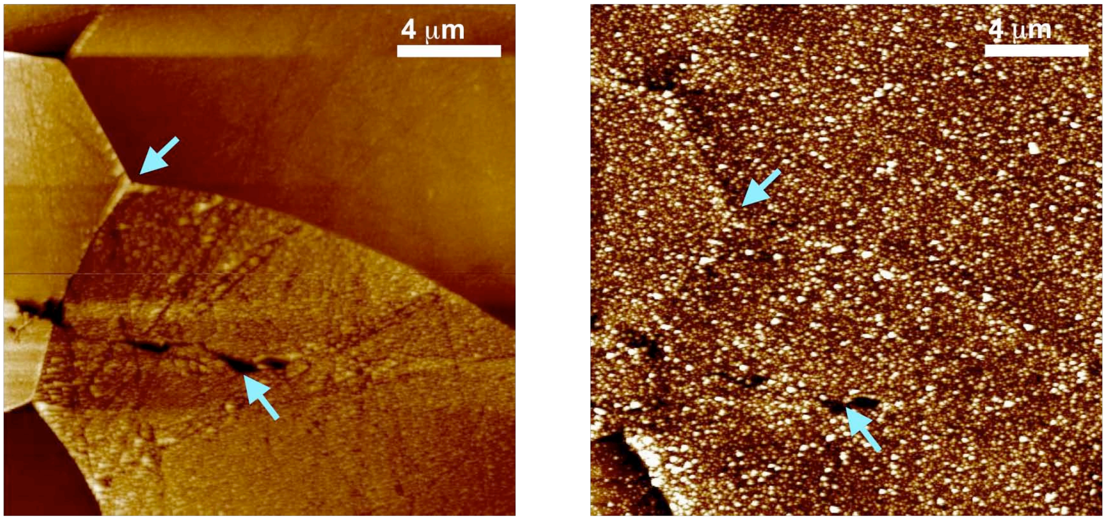

(q) (r)

Figure 6.26 – Topographical AFM images of the surface of $Sr_xBa_{1-x}TiO_3$ before and after reaction are pictured for $BaTiO_3$ **(a & b)**, $Sr_{0.1}Ba_{0.9}TiO_3$ **(c & d)**, $Sr_{0.2}Ba_{0.8}TiO_3$ **(e & f)**, $Sr_{0.26}Ba_{0.74}TiO_3$ **(g & h)**, $Sr_{0.27}Ba_{0.73}TiO_3$ **(i & j and k & l)**, $Sr_{0.28}Ba_{0.72}TiO_3$ **(m & n)**, $Sr_{0.4}Ba_{0.6}TiO_3$ **(o & p)** and $SrTiO_3$ **(q & r)**. The black-to-white contrast for the images is – **(a)** 60 nm, **(b)** 60 nm, **(c)** 45 nm, **(d)** 75 nm, **(e)** 40 nm, **(f)** 60 nm, **(g)** 120 nm, **(h)** 95 nm, **(i)** 40 nm, **(j)** 60 nm, **(k)** 40 nm, **(l)** 70 nm, **(m)** 50 nm, **(n)** 90 nm, **(o)** 75 nm, **(p)** 110 nm, **(q)** 100 nm and **(r)** 110 nm. The blue arrows in the images draw attention to the same features on the before and after images of each set.

In **Fig. 6.27** two sets of before and after reaction images along with the surface potential images are shown for $Sr_{0.26}Ba_{0.73}TiO_3$. **Fig. 6.27 (a & d)** show the surfaces before reaction, images **(b & e)** show the surface potential images recorded simultaneously with the corresponding before reaction ones and images **(c & f)** show the surfaces after reaction. For these images in **Fig. 6.27** the reaction time was 4 seconds. The reaction time is lower than that used for the reactivity comparison study (6 seconds) because at 6 seconds the surface of $Sr_{0.26}Ba_{0.73}TiO_3$ is too saturated with silver to clearly see if there is spatially selective reactivity. In **Fig. 6.27 (c)**, the blue boxes mark the region where Ag was accidentally wiped off during handling the sample. The green arrows on the images show some positively charged domains in **Fig. 6.27 (b & e)** and the corresponding areas in **Fig. 6.27 (c & f)**. It can be seen from the surface potential images that the ferroelectric domains exist in $Sr_{0.26}Ba_{0.73}TiO_3$. However, Ag reaction is not as spatially selective as it is in the case of $BaTiO_3$ and $Sr_{0.1}Ba_{0.9}TiO_3$. There is Ag everywhere on the surface with slightly more on the domains. This shows that the high reactivity of this sample is not due to ferroelectric domains alone. The high reactivity can be attributed to high dielectric constant for this composition. This is explained in detail in the following section.

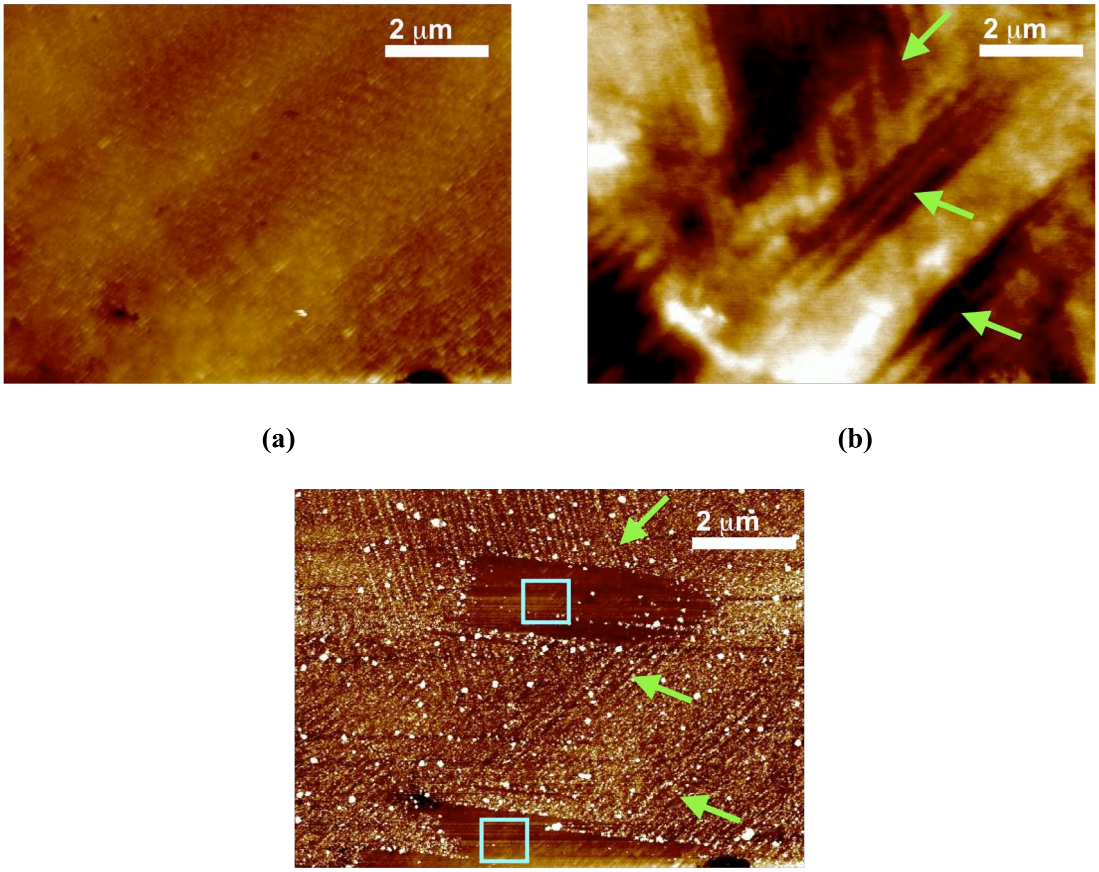

(a) **(b)**

(c)

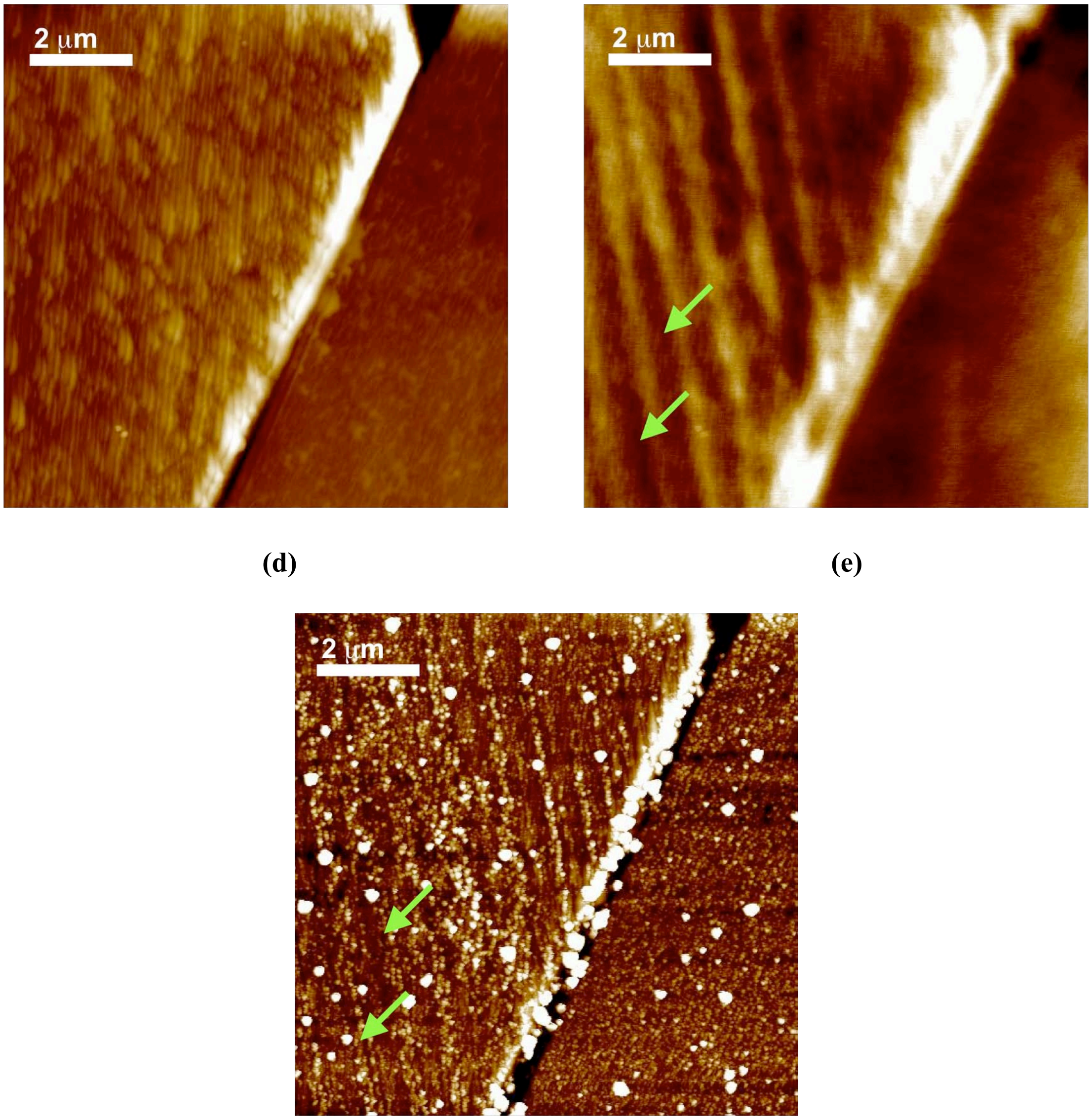

(d) (e)

(e)

Figure 6.27 – Topographical AFM images of the surface of $Sr_{0.26}Ba_{0.74}TiO_3$ before reaction **(a & d)** and after reaction **(c & f)** are pictured. Surface potential images **(b & e)** of the surface are taken simultaneously with **(a & d)**. The black-to-white contrast for the images in **(a to f)** is 70 nm, 90 mV, 70 nm, 80 nm, 90 mV and 80 nm. The green arrows in the images draw attention to the location of the same domains on the surface potential and after images of each set. The blue boxes in **(c)** mark the regions on the surface where silver was wiped off during the handing of the sample.

6.5 Discussion.

As mentioned in **Section 4.2.1**, methylene blue was used to study the photochemical reactivity of the samples because it changes color on changing its oxidation state. This change of color is taken as the measure of the sample's photochemical reactivity. The redox potential for a 10 μM solution of methylene blue is +0.011 eV on NHE scale at pH 7 [13]. It is very close to H_2/H^+ redox potential (=0 eV on NHE scale) and lies within the band gap of the $Sr_xBa_{1-x}TiO_3$ compositions as seen in **Fig. 3.5**.

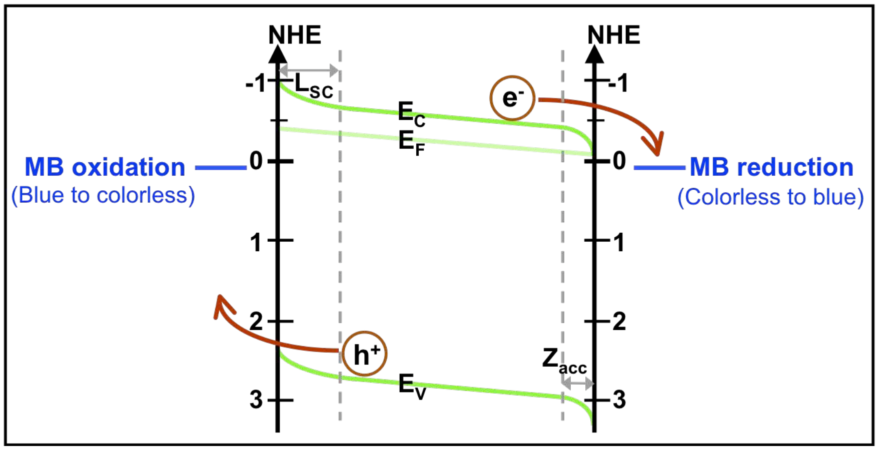

Figure 6.28 – Schematic showing the interaction of methylene blue dye on the sample surfaces with upward and downward band bending. The space charge layer width L_{SC} and Z_{acc} in $BaTiO_3$ is ~ 162 nm and 23 nm (calculated later in this section).

When the sample is immersed in solution, dye adsorbs on the surface of the sample. During illumination, the colorless oxidized form of the dye takes an electron from the positively charged surface and changes its color to blue as shown in **Fig. 3.5 and 3.6**. However, the reaction opposite to the one shown in **Fig. 3.5** takes place on the negatively charged domains with upward band bending and the blue reduced form of the dye from the solution gives an electron and becomes colorless (**Fig. 6.28**). The net result is that the illuminated surface of the sample turns darker due to more and more blue reaction product sticking to it and the solution turns lighter in color due to the blue ions turning colorless by the same amount. This change in color is greater for more reactive samples than for the less reactive ones. In other words, this change in color at the surface and in the solution is a measure of photochemical reactivity.

For the Atomic Force Microscopy study, the amount of Ag on the surface after the reaction with a 0.115 M $AgNO_3$ aqueous solution is taken as a measure of photochemical reactivity. The amount of Ag reduced by different $Sr_xBa_{1-x}TiO_3$ compositions is measured to determine their relative reactivities.

From the data obtained for the comparison of photochemical reactivity (**Fig. 6.9, 6.10, 6.22 & 6.25)**, it was seen that as the amount of Sr increases in $BaTiO_3$, the reactivity first decreases, then increases and peaks near the ferroelectric to non-ferroelectric transition. After the local maximum, the reactivity increases again and, at x = 1 for $Sr_xBa_{1-x}TiO_3$, the reactivity of $SrTiO_3$ is similar to $BaTiO_3$. This shows that polarization is not the only parameter that is affecting the reactivity. Had P_S been the only factor, the reactivity would have followed the same trend as the change in P_S with composition (**Fig. 6.29**) [14].

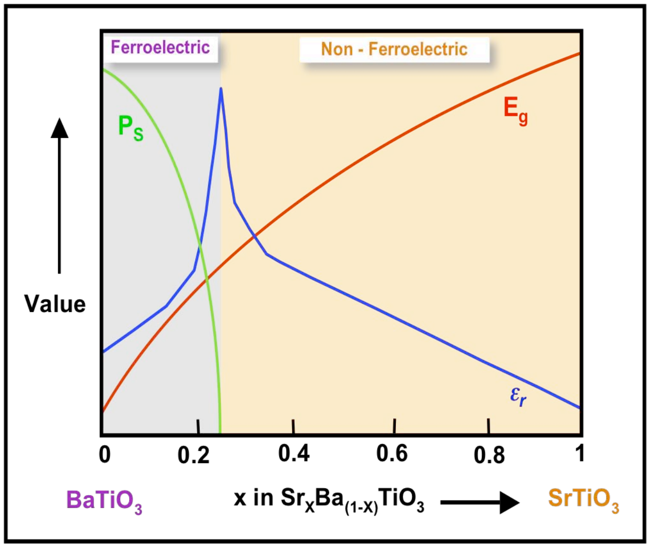

Figure 6.29 – Schematic of the changes in polarization, dielectric constant and band gap with the change in Sr content of $Sr_xBa_{1-x}TiO_3$ samples.

Fig. 6.29 shows the trend of some parameters that influence the reactivity of $Sr_xBa_{1-x}TiO_3$ compositions. The polarization (P_S) plot with composition was estimated by simulation at 0 K by Tinte *et al.* [14]. The trend of change in P_S is assumed to be similar at room temperature, which is relevant to the current resuts. The original plot of P_S vs. composition by Tinte *et al.* [14] is modified to represent the ferroelectric phase change at room temperature and the plot is also extrapolated till the P_S value equal to 0 to mark the transition from ferroelectric to non-ferroelectric phase.

The change in dielectric constant with an increase in Sr in $Sr_xBa_{1-x}TiO_3$ powders prepared by the sol-gel method was measured by Ding *et al*. [15]. The main result of the Ding *et al.* [15] work is that the reactivity peaks at the transition from the ferroelectric to non-ferroelectric phase. This is also known from earlier work [16] and is the basis for the curve in **Fig. 6.29**. However, it should also be noted that Ding *et al.* [15] found the transition in the range of x = 0.1 to 0.2. They also report an abnormally large value for the dielectric constant of $SrTiO_3$ that conflicts with other sources (dielectric constant value = 300 [17, 18]). The source of these differences is not clear, but might be due to the temperature (not reported) at which they made the measurements or the sample preparation method.

The trend in the change of band gap of thin films of $Sr_xBa_{1-x}TiO_3$ was reported by Thielsch *et al*. [19] and Samantaray *et al* [20]. They calculated the band gap using Tauc and Menth law as described in **Eqn. 6.2**.

$$\alpha.E \approx A.(E - E_{gap})^m \qquad \text{---(6.2)}$$

where A is a constant, and m = 0.5, 2, 1.5 or 3 for allowed direct, allowed indirect, forbidden direct and forbidden indirect electronic transitions, respectively [21, 22]. They observed that the value of *m* was 0.5 for all compositions indicating that the absorption process was due to direct allowed electronic transition between the highest occupied state of the valence band and the lowest unoccupied state of the conduction band. The value of α was determined from reflection spectra of each $Sr_xBa_{1-x}TiO_3$ composition using reflection extrema envelope method [23, 24]. They observed that the band gaps for the films were higher than the reported values for the bulk samples. Since bulk samples are used in this research, it is assumed that the trend of change in the band gap will be the same as for the films, though the endpoints will match the band gaps of the pure bulk phases (**Fig. 6.29**). The numerical values of the parameters shown in **Fig. 6.29** are shown in **Table 6.1** below.

Table 6.1 – Values of band gap, polarization and dielectric constant for $Sr_xBa_{1-x}TiO_3$ samples. $Sr_{0.26}Ba_{0.74}TiO_3$ is the composition at the transition from ferroelectric to non-ferroelectric phase.

Property **Composition**	**Band gap (E_{gap}) eV**	**Polarization (P_S) µC/cm^2**	**Dielectric Constant (ε_r) dimentionless**
$BaTiO_3$	3 [14]	26 [15]	2000 [7]
$Sr_{0.26}Ba_{0.74}TiO_3$	3.05*	~ 0 *	11000 [7]
$SrTiO_3$	3.2 [14]	0	300 [17, 18]

**** Interpolated from the data available in literature.***

The other factors that strongly affect the availability of photon generated charge carriers for useful work are the absorption coefficient and the efficiency of non-radiative electron transitions (discussed earlier in **Sections 2.4.5.1 & 2.4.5.2** respectively). The absorption coefficient will be discussed first. To review, the absorption coefficient (α) is a property of a material and gives the intensity of radiation of a certain wavelength after traveling 1 cm into the sample. It is one of the key factors that determine the quantum efficiency [25, 26]. If the absorption coefficient of a material is zero, no light is absorbed. Therefore, no charge carriers are photogenerated and this is not a suitable condition for photochemical reactivity. On the other hand, if the absorption coefficient of a material is extremely large, all the radiation is absorbed and the charge carriers are generated in a shallow region near the surface because the penetration depth is extremely small. In this situation, though the higher density of charge carriers will increase the recombination rate, the photochemical reaction is still favored because the electrons and holes are generated close to the surface in the space charge region where they can be separated and have a relatively short distance to travel to the surface. The values of α [27, 28] (also mentioned in **Table 3.1**) and the calculated penetration depths for $BaTiO_3$ and $SrTiO_3$ at wavelengths corresponding to their respective band gaps are as shown in **Table 6.2**. It can be seen that the α value for $SrTiO_3$ is slightly lower than that of $BaTiO_3$ and therefore the penetration depth is longer for the former.

To maximize the charge carrier separation, it is important that the charge carriers are photogenerated in the space charge region of the material. The electrons and holes created outside of space charge region are more likely recombine. In other words, light absorbed deeper in the bulk of the material is wasted. Consider the case where the penetration depth is much larger than the space charge layer widths in materials with band gaps close to each other. For the same amount of absorbed radiation ($> E_g$), a higher absorption coefficient promotes photochemical reactions because more charge carriers are generated closer to the surface. There is also a possibility of expanding the space charge region (for example, by changing the pH of the solution), provided the particle size of the material is greater than twice the space charge layer width, and increasing the spatial separation of the charge carriers to further enhance the reactivity.

Table 6.2 – Absorption coefficient and calculated penetration depth of incident radiation in $BaTiO_3$ and $SrTiO_3$.

Property / **Composition**	**Absorption Coefficient (α) cm^{-1}**	**Penetration Depth ($1/\alpha$) μm**
$BaTiO_3$	40-50 [27]	200 – 250
$SrTiO_3$	10-20 [28]	500 – 1000

Another factor that increases the recombination rate of photogenerated charge carriers is the efficiency of non-radiative transitions (explained earlier in **Section 2.4.5.2**). To review, alloy scattering in solid solutions decreases the mean free path of charge carriers in a material and increase the recombination rate [29]. The presence of impurity states within the band gap of a material (due to doping and presence of defects) can also act as recombination centers by trapping electrons and holes and thereby annihilating the pair [25]. Photoluminescence studies provide information about impurity states. In photoluminescence spectra of materials excited by monochromatic radiation, higher intensity of luminescence or emitted radiation from a material suggests lower efficiency of non-radiative transitions or fewer impurities in the material [26]. H. Kato *et al.* [30] conducted photoluminescence study on $Sr_2(Ta_{1-X}Nb_X)_2O_7$ solid solutions. They observed that despite having a wider band gap (0.63 eV larger than $Sr_2Nb_2O_7$) $Sr_2Ta_2O_7$ had the highest luminescence intensity when irradiated by monochromatic radiation of 260 nm wavelength at 77 K. This suggested that $Sr_2Ta_2O_7$ had the lowest efficiency of non-radiative transition. The luminescence intensity decreased significantly with small additions of Nb (x= 0.1). However as the Nb content was increased the luminescence intensity increased and became almost equal to that for $Sr_2Nb_2O_7$ at x = 0.5 sample. They also compared photochemical reactivities of different compositions by recording and comparing the rate of H_2 production using these materials activated with NiO as catalysts and found that $Sr_2Ta_2O_7$ was more reactive than $Sr_2(Ta_{1-X}Nb_X)_2O_7$ with x = 0.1 composition and proposed that there is a direct correlation between the efficiency of non-radiative transition and reactivity. The authors have stated that if non-radiative transitions are dominant in a material, it decreases the number of charge carriers available for reactions and, therefore, decreases the photochemical reactivity.

The presence of impurities / defects creates absorption bands in a material and these are reflected in the absorption coefficient vs. wavelength plots. Tian *et al.* [31] analyzed $Sr_xBa_{1-x}TiO_3$ thin films of ~230 nm thickness and x = 0.1, 0.2 and 0.3. They observed that as the Sr content increases in the films, the absorption coefficient in the absorption band near the band edge decreases. This suggests that the impurities or defects increase in the films as Sr increases. In other words, Sr addition to $BaTiO_3$ creates scattering centers that act as recombination sites causing the efficiency of non-radiative transition to increase. This trend can be assumed to be true in the case of bulk $Sr_xBa_{1-x}TiO_3$ as addition of Sr to $BaTiO_3$ in small amount can create scattering centers in $BaTiO_3$ and vice versa for Ba addition to $SrTiO_3$. However for this it is assumed that intrinsic defect concentration like that of oxygen vacancies and the ordering of the structure are similar for all the $Sr_xBa_{1-x}TiO_3$ compositions prepared in this research. The variation in oxygen vacancy concentration and the ordering of the crystal structure is known to influence the photoluminescence behavior of $BaTiO_3$ and $SrTiO_3$ for obvious reasons and can therefore affect the efficiency of non – radiative electron transitions [32-36].

Noting all the above mentioned facts about the parameters affecting the reactivities of the $Sr_xBa_{1-x}TiO_3$ samples, the results obtained in this research are analyzed as follows. There are two main observations in this research – the reactivity decreases on addition of Sr and Ba in $BaTiO_3$ and $SrTiO_3$ respectively, and there is a local maximum in reactivity at the composition at ferroelectric to non – ferroelectric transition. The factors that most consistently explain these observations are alloy scattering and dielectric constant. Alloy scattering due to the addition of Sr and Ba in $BaTiO_3$ and $SrTiO_3$ respectively, decreases the mean free path of the charge carriers and therefore increase the recombination of electrons and holes. This has an adverse effect on photochemical reactivity. A large dielectric constant creates a wider space charge region. Because the absorption depth is always greater than the width of the space charge region, more charge carriers separated and the reactivity increases. Therefore, the high reactivity at the transition composition corresponds to a high value of dielectric constant (**Fig. 6.29**) at room temperature. Other factors such as band gap, polarization and absorption coefficient are of less significance.

As explained in **Section 2.4.2**, Debye length and space charge layer widths are related to the dielectric constant as described by **Eqns. 2.1, 2.2, 2.3 & 2.4** [37, 38]. Even without knowing the exact numbers for the parameters required to estimate these lengths, it can be seen that as the dielectric constant increases, Debye length and space charge layer widths increase. However, it will be interesting to estimate the Debye length and space charge layer widths of the materials used in this research. The method to estimate these is explained as follows. The values of different parameters used to calculate L_D, L_{SC}

and Z_{acc} for different samples and the results are shown in **Table 6.3**. Since both L_D and L_{SC} (for non – ferroelectric materials) are directly proportional to the square root of ε_r (**Eqns. 2.3 and 2.1**), the Debye length and the space charge layer width will be large for large values of ε_r. The change in L_D with the change in ε_r is shown in **Fig. 6.30**. The value of N_D is assumed to be that of bulk $BaTiO_3$ that was reported to be 10^{19} cm^{-3} (6.4×10^{-4} ppm by mole) by Remeika and Nishioka *et al* [39, 40]. In **Fig. 6.30** the plots are drawn with three different values of N_D to see the effect on L_D. The value of Debye length for the $Sr_xBa_{1-x}TiO_3$ transition composition (Dielectric constant 11000 [15]) is approximately five times the Debye length of $SrTiO_3$ (Dielectric constant 300 [17, 18]) and approximately twice the Debye length of $BaTiO_3$ (Dielectric constant 2000 [15]) for any value of N_D. When $BaTiO_3$ is doped with 0.5 mole % Y_2O_3, L_D and L_{SC} change only due to the change in N_D (**Section 6.4.1.3(c)**). The value of N_D for the doped sample is calculated to be 8.8×10^{19} cm^{-3} (5×10^{-3} ppm by mole) assuming complete ionization of donor states at room temperature. To calculate the value of L_D for doped and undoped $BaTiO_3$, **Eqn. 2.3** is used. The value of L_D for undoped and doped $BaTiO_3$ is 17 nm and 6 nm respectively.

Now considering the depletion space charge layer width, L_{SC}, **Eqn. 2.4** is used to calculate the L_{SC} for both doped and undoped $BaTiO_3$ (because $BaTiO_3$ is ferroelectric) and **Eqn. 2.1** is used to calculate the L_{SC} for all the compositions with $P_S = 0$ including the composition at the transition (because $P_S \approx 0$ at the transition) and $SrTiO_3$. To calculate the accumulation space charge layer width (Z_{acc}), **Eqn. 2.2** is used for all the compositions ($BaTiO_3$, doped $BaTiO_3$, $Sr_xBa_{1-x}TiO_3$ composition at the transition and $SrTiO_3$). For doped and undoped $BaTiO_3$ the value of $P_S = 26$ $\mu C/cm^2$ [41] is used to calculate L_{SC}. As can be seen in **Fig. 3.5**, the maximum band bending (ϕ_{SC}) possible for the reaction of the samples with the dye to take place is equal to the difference between the conduction band edge and the redox potential of the dye (for oxidation reaction only or for positively charged surfaces). For band bending greater than this difference the oxidation reaction will not take place. Therefore the value of V_S used to calculate Z_{acc} is taken to be 0.25 eV for the $Sr_xBa_{1-x}TiO_3$ composition with x = 0.26 and 0.4 eV for $SrTiO_3$ (from **Fig. 3.5** and **Table 6.1**).

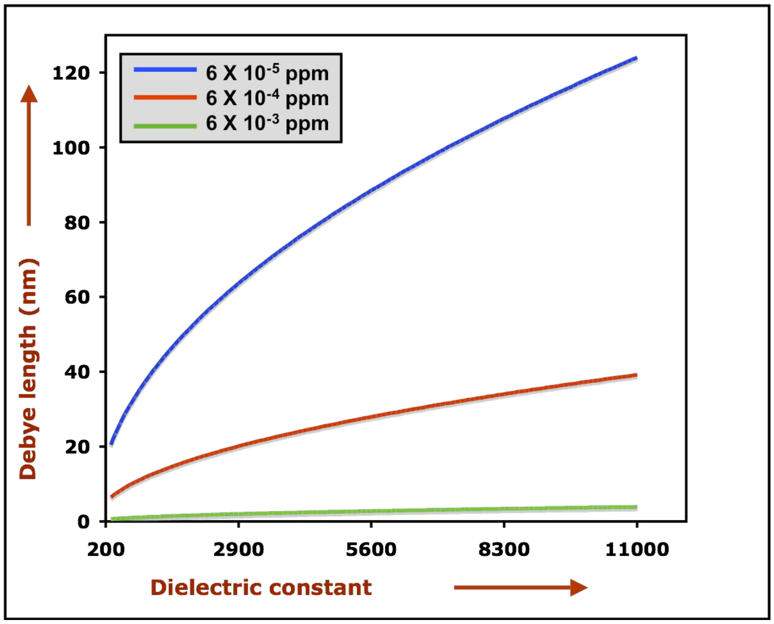

Figure 6.30 – Schematic of the change in Debye length by changing the dielectric constant for different values of N_D (ppm by mole) in $Sr_xBa_{1-x}TiO_3$ samples.

On the negatively charged surfaces, the maximum band bending possible that allows the reduction reaction to occur is more that 2 eV (from **Fig. 3.5**). This amount of band bending is unlikely to exist without the application of external bias. Therefore, the position of the conduction band edge of non – ferroelectric compositions has to be estimated using **Eqns. 2.5 and 2.8**. The point of zero charge for $SrTiO_3$ is taken to be 8.6

pH [42] (**Table 3.1**) and is assumed to be the same for $Sr_xBa_{1-x}TiO_3$ composition at transition. The difference in the conduction band edge at the pH of the dye solution (~ 6.3 pH, **Section 6.4.1.4(i)**) and at flat band condition is taken to be the amount of band bending (ϕ_{SC}). This calculated value of ϕ_{SC} is 0.14 eV. The effect of surface states on band bending is ignored in this calculation. Since $Sr_xBa_{1-x}TiO_3$ solid solutions are n – type semiconductors, there is a strong likelihood of trapping of electrons in the surface states thereby adding to the negative charge at the surface. In this case, the inclusion of the effect of surface states should only increase the amount of upward band bending at the surface and increase the value of ϕ_{SC}. However, it is not possible to estimate the effect of surface states and therefore, for this discussion the minimum band banding at the negative surfaces (due to the difference between pzc and actual pH) is used to calculate depletion space charge layer widths (L_{SC}).

The values of dielectric constant and donor density, ε_r and N_D respectively, are taken as 300 [17, 18] and 10^{19} cm^{-3} [22] for $SrTiO_3$, 11000 [15] and 10^{19} cm^{-3} for $Sr_xBa_{1-x}TiO_3$ composition at $x = 0.26$ (assuming that the value of N_D for $Sr_xBa_{1-x}TiO_3$ compounds does not vary from that of the pure materials $BaTiO_3$ and $SrTiO_3$) and 2000 and 8.8×10^{19} cm^{-3} for doped $BaTiO_3$. Thus the values of L_{SC} for $BaTiO_3$, doped $BaTiO_3$, $Sr_{0.26}Ba_{0.74}TiO_3$, and $SrTiO_3$ are found to be 162 nm, 19 nm, 130 nm and 22 nm. The calculated values of Z_{acc} for $BaTiO_3$, doped $BaTiO_3$, $Sr_xBa_{1-x}TiO_3$ composition at the transition and $SrTiO_3$ are 23 nm, 8 nm, 56 nm and 10 nm respectively. To review, longer Debye lengths and space charge layer widths indicate that more charge carriers are separated in a greater volume of the material. Hence the possibility of charge carrier recombination is reduced.

Table 6.3 – Values of calculated Debye lengths (L_D) and space charge layer widths (L_{SC} and Z_{acc}) and the parameters used for the calculation (polarization (P_S), band bending (ϕ_{SC} or V_S) and dielectric constant (ε_r)).

Property **Composition**	**P_S ($\mu C/cm^2$)**	**ϕ_{SC} (eV)❖**	**V_S (eV)#**	**ε_r (no units)**	**L_D (nm)**	**L_{SC} (nm)**	**Z_{acc} (nm)**
$BaTiO_3$	2 [41]	–	0.2	2000 [15]	17	162	23
Y_2O_3 doped $BaTiO_3$	26*	–	0.2*	2000*	6	19	8
$Sr_{0.26}Ba_{0.74}TiO_3$	–	0.14	0.25	11000 [15]	39	130	56
$SrTiO_3$	–	0.14	0.4	300 [17, 18]	7	22	10

❖ ***Assumed to be due to the pH of the solution only.***
 # Assumed from the positions of the band edges and redox potential of the dye.
**** Assumed to be the same as $BaTiO_3$ based on literature.***

If it is true that a wider space charge region promotes increased reactivity, then the reactivity should decrease if the space charge region is made smaller. This idea was tested by the experiment that compared the reactivities of undoped and donor doped $BaTiO_3$. The lower reactivity of the doped sample supports the idea that reactivity is related to the space charge layer width. However, it must also be added that the addition of dopants also adds impurity states in the band gap of $BaTiO_3$ that increase the efficiency of non – radiative electron transitions. This effect will also cause a decrease in reactivity and may contribute to the decreased reactivity of the doped sample.

The $Sr_xBa_{1-x}TiO_3$ composition at ferroelectric to non – ferroelectric transition has the highest dielectric constant and therefore has longer space charge region. The polarization at this composition is approximately zero and it has been shown from the AFM study that the photochemical reactions do not occur in a spatially selective way (**Fig. 6.27**). Hence, the contribution of polarization to high reactivity at the transition is ruled out. Also, as the value of x decreases in $Sr_xBa_{1-x}TiO_3$ compounds away from the transition, the dielectric constant decreases but the polarization increases. However, the reactivity still decreases and this further shows that polarization is not the dominant factor affecting the reactivity in this composition region. Similarly, as the Sr content increases in $Sr_xBa_{1-x}TiO_3$ compounds away from the transition, the dielectric constant decreases and so does the reactivity. The additions of alloying elements (Sr in $BaTiO_3$ and Ba in $SrTiO_3$) create scattering centers in the structure of the material and decrease the mean charge carrier lifetimes. This increases the rate of charge carrier recombination and therefore lowers the reactivity. The effect of this alloy scattering on reactivity is evident in $Sr_xBa_{1-x}TiO_3$ solid solutions as x increases from zero and decreases from 1.

Along with dielectric constant and alloy scattering, there are other factors that can affect the photochemical reactivity such as polarization and conduction band edge position with respect to redox potential of the reacting species. The possibility of dipolar fields enhancing the reactivity still exist, however, this effect will be limited to pure $BaTiO_3$ and $Sr_xBa_{1-x}TiO_3$ with extremely small Sr content until the effect of alloy scattering does not overcome the effect of dipolar fields. The relative position of conduction band edge to the redox potential of the reactants indicates the thermodynamic favorability of the photochemical reaction. Since the conduction band edge of $SrTiO_3$ is higher than the other compositions, the potential difference between the electron in the conduction band and the redox potentials of the reacting species (methylene blue dye and silver nitrate in this research) is greater and if this were the only factor, it suggests that $SrTiO_3$ would be more reactive than the other compositions. The position of the conduction band edge and the polarization can potentially enhance the reactivity, but only in nearly pure compositions and are not the prime factors affecting the photochemical behavior of $Sr_xBa_{1-x}TiO_3$.

In the case of reduction of silver, the presence of silver on the surface of the samples after initial nucleation acts as a metal – semiconductor junction. Since the work function of silver (~ 4.6 eV with respect to vacuum level [43]) is lower than the conduction band edge of $Sr_xBa_{1-x}TiO_3$ (~ 3.6 – 3.7 eV with respect to vacuum level), the transfer of electrons to the silver deposits is favored. This should therefore make the reduction reaction self – sustainable on the silver nuclei till a certain thickness of silver deposits and should therefore affect the amount of silver present on the surface after a certain period of reaction time. Therefore, one might suppose that the total amount of silver formed on the surface is determined by the number of nuclei that form. If this were true, then samples with spatially uniform reactivity would have more nuclei and more silver. However, the AFM results in this research did not demonstrate this correlation. The samples that uniformly react have more silver nuclei per unit area as compared to the samples that react spatially selectively. If the formation of metal – semiconductor junction was controlling the reactivity, then all the uniformly reacting samples would have had higher reactivities than the samples that reacted spatially selectively. However that is not the case and therefore the influence of the formation of metal – semiconductor junction (for the reduction reaction of silver) on the reactivity trend in $Sr_xBa_{1-x}TiO_3$ is ruled out.

Lastly, the surface areas of the samples play an important role in the rates of reactions. More surface area implies higher reactivity. The surface areas of the $Sr_xBa_{1-x}TiO_3$ samples were not controlled in this research. The SEM images (**Fig. 5.3**) of different $Sr_xBa_{1-x}TiO_3$ samples show that the surfaces are similar. Therefore, the difference in the surface areas of different $Sr_xBa_{1-x}TiO_3$ samples controlling the reactivity is unlikely.

6.6 References.

1. French, R.H., J. Am. Ceram. Soc., 1990. **73**: p. 477.
2. Kalinin, S., R. Shao, and D.A. Bonnell, J. Am. Ceram. Soc., 2005. **88**: p. 1077-1098.
3. Kalinin, S. and D.A. Bonnell, Physical Review B, 2001. **63**: p. 125411.
4. Kim, J.H. and Y.H. Han, Mat. Sc. For., 2007: p. 534-536.
5. Vlack, L.H.V., *Elements of Materials Science and Engineering 6th ed*. 1989: Addison – Wesley Publishing Company.
6. Jeong, J.H., M.G. Park, and Y.H. Han, J. of Electroceram., 2004. **13**: p. 805-809.
7. Xue, L.A., Y. Chen, and J. Brook, Mat. Sc. and Eng. B, 1988. **B**: p. 193.
8. Lin, M.H. and H.Y. Lu, Mater. Sci. Eng., A, 2002. **335**: p. 101.
9. Morrison, S.R., *Electochemistry at Semiconductor and Oxidized Metal Electrodes*. 1980, New York: Plenum Press.
10. Lizama, C., et al., Catalysis. Today, 2002. **76**: p. 235-246.
11. Giocondi, J.L. and G.S. Rohrer, J. Phys. Chem. B, 2001. **105**: p. 8275-8277.
12. Giocondi, J.L. and G.S. Rohrer, Chem. Mater., 2001. **13**: p. 241-242.
13. Rao, P.S. and A. Hayon, The J. of Phys. Chem., 1973. **77**(23): p. 2753-2756.
14. Tinte, S., et al., J. Phys.: Condens. Matter, 2004. **16**: p. 3495–3506.
15. Ding, S., et al., Acta Chimica Sinica, 2006. **64**(12): p. 1243-1247.
16. Nowotny, J. and M. Rekas, Key Eng. Mater., 1992. **45**: p. 66-67.
17. Choudhury, B.K., K.V. Rao, and R.N.P. Choudhury, J. Mater. Sci., 1989. **24**: p. 3469 – 3474.
18. Nowotny, J. and M. Rekas, Key Engineering Materials, 1992. **66-67**: p. 45-144.
19. Thielsch, R., et al., Thin Solid Films, 1997. **301**: p. 203–210.
20. Samantaray, C.B., et al., Indian J. Physics 2001. **75A**(4): p. 347-350.
21. Mott, N.F. and E.A. Davis. Electronic Processes in Non-crystalline Materials, 2nd edn. 1979, Oxford: Clarendon Press.
22. Tauc, J. and A. Menth, J. Non-cryst. Solids, 1972. **569**: p. 8-10.
23. Kushev, D.B., et al., Infrared Phys., 1986. **26**: p. 385.
24. Minkov, D.M., J. Phys. D: Appl. Phys., 1989. **22**: p. 1157.
25. Sze, S.M., *Physics of Semiconductor Devices, 2nd edition*. 2001: John Wiley & Sons Inc.
26. Streetman, B.G. and S. Banerjee, *Solid State Electronic Devices, 5th edition*. 2005: Prentice Hall.
27. Berglund, C.N. and H.J. Braun, Phy. Rev., 1967. **164**(2): p. 790-799.
28. Noland, J.A., Phys. Rev., 1954. **94**(3): p. 724.

29. Omar, M.A., *Elementary Solid State Physics : Principles and Applications*. Addison - Wesley Series in Solid State Sciences. 1975, USA: Addison - Wesley Publishing Company, Inc.
30. Kado, H. and A. Kudo, J. of Photochem. And Photobio. A : Chem., 2001. **145**: p. 129-133.
31. Tian, H.Y., et al., Mat. Sci. and Eng. B,, 2003: p. 246-252.
32. Orhan, E., et al., J. Solid State Chem., 2004. **177**: p. 3879.
33. Chang-Qing, J., et al., Chin. Phys., 2007. **16**: p. 3125.
34. Shanthi, N. and D.D. Sarma, Phys. Rev. B, 1998. **57**: p. 2153.
35. Orhan, E., et al., J. Phys. Chem. B., 2004. **108**: p. 9221.
36. Orhan, E., et al., Phys. Rev. B, 2005. **71**: p. 085113.
37. Albery, W.J. and P.N. Bartlett, J. Electrochem. Soc., 1984. **131**: p. 315.
38. Monch, W., *Electronic Properties of Semiconductor Interfaces*. 2004, New York: Springer-Verlag Berlin Heidelberg.
39. Remeica, J.P., J. Am. Chem. Soc., 1954. **76**: p. 940.
40. Nishioka, A., K. Sekikawa, and M. Owaki, J. Phys. Soc. (Japan), 1956. **11**: p. 180.
41. Burfoot, J.C. and D.V. Nostrand. Ferroelecrics: An Introduction to the Physical Properties. 1967, London: Company Ltd.
42. Reichman, B. and B. Mich. 1985: USA
43. Lide, D.R., *CRC handbook on Chemistry and Physics*. 89th ed. 2008: CRC.

7. Conclusions.

In this research, it was originally hypothesized that the ferroelectric compositions of $Sr_xBa_{1-x}TiO_3$ are more reactive than the non-ferroelectric ones because of better charge separation due to polarization in the ferroelectric samples. The results obtained in this research however do not substantiate this hypothesis. It is observed that along with polarization there are other factors such as the dielectric constant and the efficiency of non – radiative electron transitions (due to alloy scattering) that significantly affect the reactivity of $Sr_xBa_{1-x}TiO_3$. The photochemical reactivities of polycrystalline $Sr_xBa_{1-x}TiO_3$ samples are studied by two methods – comparing the extent of photodegradation of methylene blue dye solution and comparing the amount of silver reduced from aqueous $AgNO_3$ solution by different compositions under similar experimental conditions. While both the probe reaction and the microstructures of the samples in the two experiments were different, the results were qualitatively the same. The two main trends are that as more of the solid solution component is added to either $BaTiO_3$ or $SrTiO_3$, the reactivity decreases and that there is a local maximum in the reactivity at the $Sr_xBa_{1-x}TiO_3$ composition at the ferroelectric to non-ferroelectric transition. The conclusions of this thesis are reviewed in the remainder of this chapter.

7.1 Effect of Ferroelectric Polarization on Photochemical Reactivity.

The presence of dipolar fields in a material causes spatially selective reactivity. It was hypothesized that this spatially selective reactivity should reduce both the recombination of charge carriers and the back reaction of intermediate reaction species and that these two factors should lead to an enhancement of the reactivity. However, the observations do not substantiate this hypothesis for $Sr_xBa_{1-x}TiO_3$. In fact, samples with compositions near the ferroelectric to paraelectric transition, which have very weak polarizations, had reactivities equivalent to the most highly polarized sample ($BaTiO_3$). While it is still possible that dipolar fields have a beneficial effect on reactivity, the results of the experiments in this thesis indicate that it is not the dominant factor in the $Sr_xBa_{1-x}TiO_3$ system.

7.2 Effect of Dielectric Constant.

The most intriguing observation of this thesis is that there is a local maximum in reactivity at the ferroelectric to paraelectric transition. This corresponds to a maximum in the dielectric constant. It was hypothesized that the dielectric constant affects the reactivity through its influence on the width of the space charge region. As the space charge region is enlarged, more carriers are separated, fewer recombine, and more react at the surface. In one experiment where the width of the space charge region was deliberately decreased by increasing the donor density, the reactivity decreased, consistent with the hypothesis.

7.3 Effect of Impurity Scattering.

The reactivity of $Sr_xBa_{1-x}TiO_3$ solid solutions decrease as x increases from 0 or decreases from 1. When all the possible factors are considered, it is concluded that the most likely mechanism for the reduction in reactivity is scattering from the alloying components that reduces the carrier lifetime. Therefore, as more of the solid solution component is added, more charge carriers recombine and the reactivity decreases.

7.4 Mechanism of Methylene Blue dye – $Sr_xBa_{1-x}TiO_3$ Interaction.

During reactions with the dye solution, the $Sr_xBa_{1-x}TiO_3$ samples become increasingly blue. The AFM experiments showed that the reaction of methylene blue dye on the $Sr_xBa_{1-x}TiO_3$ samples occurs by a mechanism that is similar to the reaction with silver nitrate solution. The methylene blue dye and silver reduce on the surfaces of positively charged domains and the reduced reaction products remain at the reduction reaction site.

7.5 Relationship between Reactivity and Domain Structure on $Sr_xBa_{1-x}TiO_3$ Samples.

The comparison of the surfaces of $Sr_xBa_{1-x}TiO_3$ samples imaged by AFM after reaction (with silver nitrate) showed that the mode of reaction gradually changes from spatially selective reactivity for $BaTiO_3$ to spatially uniform reactivity for $SrTiO_3$. For $x \leq 0.1$, silver is strongly localized on certain domains while other parts of the surface are nearly free of silver. In the transition region at $x = 0.26$, silver is found on all surfaces, but the preference for the reaction on certain domains makes it possible to see the domain structure. Evidence for domains disappears completely for all compositions with $x \geq 0.28$ which exhibit spatially uniform reactivities.

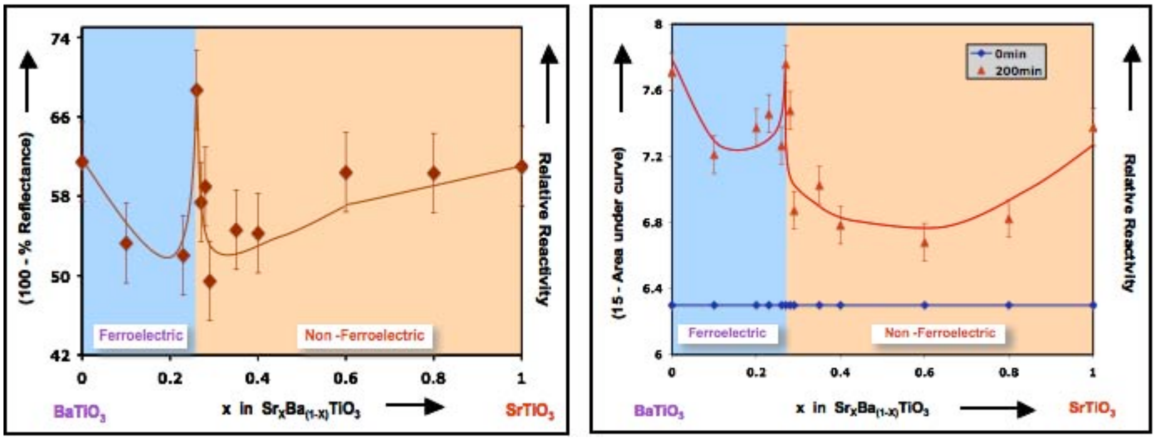

(a) **(b)**

Figure 7.1 - **(a)** **(**100 – **%** Reflectance) v/s x (mole fraction of Sr in $Sr_xBa_{(1-x)}TiO_3$ samples) at 656.8nm wavelength. **(b)** (15-Area under the curve near the peak) v/s x (mole fraction of Sr in $Sr_xBa_{(1-x)}TiO_3$ samples) zero minute and 200 min exposure time for experiments done in 5×10^{-6} M methylene blue dye solution. The lines in these plots are drawn as guides to visualize the trends in the data.

To summarize, optical spectroscopy and atomic force microscopy were used to compare the photochemical reactivities of $Sr_xBa_{1-x}TiO_3$ solid solutions. The results show that the reactivity decreases as x increases from 0 or decreases from 1, but that there is an enhancement in reactivity at the transition from ferroelectric to non-ferroelectric phase (**Fig. 7.1**). The dominant factors affecting the photochemical reactivities of $Sr_xBa_{1-x}TiO_3$ samples are the dielectric constant and the effect of alloy scattering. However a better understanding of some factors is still needed to entirely comprehend the photochemical reactivity behavior of $Sr_xBa_{1-x}TiO_3$. These are mentioned in the **Chapter 8** along with some experiments to take this research further.

8. Future Work.

8.1 Band Edge Positions at the Surface.

To get accurate values of band bending in $Sr_xBa_{1-x}TiO_3$, it is important to know exactly where the conduction and valence band edges lie on the surface for these samples. This information will help in understanding how the band banding occurs on differently charged surfaces. This can be done by recording Mott – Schottky plots or capacitance vs. applied voltage for single crystals (of different orientations for each composition) of these materials. By careful analysis of Mott – Schottky plots values of flat band potential and the surface charge densities can be obtained for different compositions at different crystal orientations. These can then be used to estimate the amount of band bending (ϕ_{SC}) on the surface. Since the positions of conduction band and valence band edges are known from the literature, the band positions at the surface can be obtained [1].

8.2 Defect Concentration.

The other factor that is of importance is to estimate the defect concentration in these materials. Oxygen vacancy concentration is reported to have effect on the photoluminescence behavior in the literature [2-6] and therefore it needs to be estimated for the $Sr_xBa_{1-x}TiO_3$ as synthesized in this research.

8.3 Photocatalysis of Water.

The long term goal of this research is to find a particulate catalyst for efficient photolysis of water to produce hydrogen gas. Hence the next step in this research is to carry out the photocatalysis of water using $Sr_xBa_{1-x}TiO_3$ powder catalysts (with NiO activation if required). The comparison of the photochemical reactivity of $Sr_xBa_{1-x}TiO_3$ catalysts of different compositions and particle sizes can be done by using the amount of hydrogen produced with the passage of time as a measure of the reactivity. The amount of hydrogen produced can be determined by Shimadzu GC-14A gas chromatograph with a thermal conductivity detector. Similar experiments have been reported in the literature with different catalysts [7-11]. The surface area measurements will also be important for comparison of reactivity of samples of different sizes because high surface area to volume ratio is favorable for reactivity. Surface area can be determined by BET measurements [12, 13].

8.4 References.

1. Morrison, S.R., *Electochemistry at Semiconductor and Oxidized Metal Electrodes*. 1980, New York: Plenum Press.
2. Orhan, E., et al., Phys. Rev. B, 2005. **71**: p. 085113.
3. Orhan, E., et al., J. Phys. Chem. B., 2004. **108**: p. 9221.
4. Orhan, E., et al., J. Solid State Chem., 2004. **177**: p. 3879.
5. Chang-Qing, J., et al., Chin. Phys., 2007. **16**: p. 3125.
6. Shanthi, N. and D.D. Sarma, Phys. Rev. B, 1998. **57**: p. 2153.
7. Inoue, Y., et al., J. Chem. Soc. Commun., 1992.
8. Domen, K., et al., J. Chem. Soc., Chem. Commun., 1986: p. 356-357.
9. Wemple, S.H. and M. DiDomenico, Phys. Rev. B, 1971. **3**: p. 1338.
10. Hwang, D.W., et al., J. of Catalysis, 2000. **193**: p. 40-48.
11. Kim, H.G., et al., Chem. Commun., 1999: p. 1077-1078.
12. Brunauer, S., P.H. Emmett, and E. Teller, J. Amer. Chem. Soc., 1938. **60**: p. 309-319.
13. Leconte, Y., et al., Glass Physics and Chemistry, 2005. **31**(4): p. 510–518.